CHARLES UNIVERSITY IN PRAGUE

Faculty of Science

Department of Physical and Macromolecular Chemistry

Program: Physical chemistry

NANOPARTICLES FORMED BY COMPLEXES OF COPOLYMERS WITH LOW-MOLAR-MASS COMPOUNDS

Jana Hajduová

PhD Thesis

Supervisor: doc. RNDr. Miroslav Štěpánek, Ph.D.

Prague 2016

Title: Nanoparticles formed by complexes of copolymers with low-molar-mass compounds

Annotation: This thesis is focused on mixed systems of various copolymers (double hydrophilic block and gradient polyelectrolytes, hydrophobic graft copolymers) and low-molar-mass compounds (sodium dodecyl sulfate as a representative of a ionic surfactant or superparamagnetic iron oxides in the form of nanocrystals). The electrostatic and hydrophobic interactions in the studied systems in aqueous solutions leading to aggregation behavior and to the formation of co-assembled nanoparticles were investigated by combination of scattering and microscopy techniques, including light, X-ray and neutron scattering, electron microscopy and atomic force microscopy.

Key words: copolymers, self-assembly, aggregation, surfactant, magnetic nanoparticles

Název: Nanočástice tvořené komplexy kopolymerů s nízkomolekulárními látkami

Anotace: Tato práce se soustředí na směsné systémy tvořené různými typy kopolymerů (dvojitě hydrofilní blokové a gradientové polyelektrolyty, hydrofobní roubované kopolymery) a nízkomolekulárními látkami (dodecylsulfát sodný jako typický iontový surfakant, superparamagnetické oxidy železa ve formě nanokrystalů). Elektrostatické a hydrofobní interakce ve studovaných systémech vedoucí k agregačnímu chování a k tvorbě samoorganizovaných nanočástic byly studovány kombinací rozptylových a mikroskopických technik, zahrnující rozptyl světla, X-paprsků a neutronů, elektronovou mikroskopii a mikroskopii atomárních sil.

Klíčová slova: kopolymery, samoorganizace, agregace, surfaktant, magnetické nanočástice

I declare that I have elaborated the thesis on my own. If already published results are used, they are included in the list of references. I agree with lending the thesis to anyone who may be interested. It is not substantially the same as any work that has been or is being submitted to any other University for any degree, diploma or any other qualification.

Prague, 8.8.2016

The support of Ministry of Education, Youth and Sports of the Czech Republic (long-term Research Project MSM0021620857, Grant LK21302), the Czech Science Foundation (Grants 13-02938S, P106-12-0143, 14-11516S) and the Technology Agency of the Czech Republic (Grant TE01020118) is gratefully acknowledged.

I would like to thank to my supervisor doc. RNDr. Miroslav Štěpánek, Ph.D. for vocational guidance, assistance, inspiring discussions, comments, suggestions and patience in creating this diploma thesis.

Special thanks belong to my family, my fiancé and friends for their support.

Contents

Abbreviations

AFM	atomic force microscopy
cac	critical aggregation concentration
Cel-*g*-PS	cellulose-*graft*-polystyrene
cmc	critical micelle concentration
d_f	fractal dimension
DHBC	double hydrophilic block copolymer
DLCA	diffusion-limited cluster-cluster aggregation
DTAB	dodecyl trimethyl ammonium bromide
HPPhMeOx	poly[(2-methyl-2-oxazoline)-*grad*-(2-phenyl-2-oxazoline)-*mod*-(ethylene imine)]
ITC	isothermal titration calorimetry
MNP	magnetic nanoparticle
MRI	magnetic resonance imaging
NPHOS	poly[3,5-bis(dimethylaminomethyl)-4-hydroxystyrene]
PAA	poly(acrylic acid)
PDEA	poly[2-(diethylamino)ethyl methacrylate]
PEO	poly(ethylene oxide)
PE-S	polyelectrolyte-surfactant complex
PMAA	poly(methyl acrylic acid)
PMEMA	poly[2-(N-morpholino)ethyl methacrylate]
PNIPAM	poly(N-isopropylacrylamide)
PVP	poly(vinylpyrro1idone)
PS	polystyrene
RLCA	reaction-limited cluster-cluster aggregation
QNPHOS	poly[3,5-bis-(trimethylammoniummethyl)-4-hydroxystyrene iodide]
SANS	small angle neutron scattering
SAXS	small angle X-ray scattering
SDS	sodium dodecyl sulfate
SLS	static light scattering
SPION	superparamagnetic iron oxide nanoparticle
TEM	transmission electron microscopy
ζ	zeta potential
Z	charge-molar ratio

1 AIM OF THE STUDY

Complexes of copolymers with low-molar-mass compounds exhibit interesting co-assembly behaviour and nanostructures they form find a number of advanced applications in biotechnology, medicine and industry.

This thesis represents a summary of results of my experimental work done during four years of my PhD. studies. My attention was focused on the study of co-assembled nanostructures formed by various types of copolymers with ionic surfactants and superparamagnetic iron oxide nanoparticles.

The studies of the complexes were aimed at the invention of reproducible preparation protocol and detailed characterization of formed nanostructures on the wide length and time scales.

2 THEORETICAL PART

2.1 BLOCK COPOLYMERS

Block copolymers are a class of polymers which are formed by covalently connected at least two different types of polymer segments or blocks containing homogeneous repeating units. The most interesting property of block copolymers is the micro-phase segregation behaviour that may occur between the blocks. Self-assembly of block copolymers due to segregation of mutually incompatible blocks has been a subject of numerous studies both for its general importance in physical chemistry of polymers and its impact on potential applications [1-3]. The segregation of polymer chains can be explained by considering the contributions to the free energy of mixing. Since a polymer is made of covalently connected repeating units the entropy for mixing two dissimilar polymers is much less than the mixing entropy of small molecules. For example, in the bulk state, a larger contribution to the mixing free energy of dissimilar polymer chains comes from the enthalpy, which is usually positive, unless the chains have specific interactions such as ion pairing or H-bonding. Under such conditions, the dissimilar polymer chains tend to become segregated from each other. For block copolymers in the bulk state, micro-phase separation is driven by thermodynamic incompatibility, while the macro-phase separation is prevented by the covalent bonds holding the different blocks together.

Block copolymers can self-assemble into versatile nanostructures of various morphologies, either in the solid state, or in block selective solvents. Generally, the morphology of block copolymers in the bulk state is governed by the number of repeating units, the volume fraction of the different blocks, and the Flory-Huggins parameter, χ, which describes the enthalpy of contacting polymer chains [4]. Block copolymer solutions in block selective solvents exhibit complex phase behaviour including the micellar regime at low concentrations as well as lyotropic liquid crystalline phases in concentrated solutions [5]. A selective solvent for a block copolymer is defined as a solvent which dissolves at least one block and which

causes the precipitation of the other blocks. It used to be also considered as a good solvent for one block and poor solvent for another one. If we put a linear AB diblock copolymer into a block selective solvent, which is a good solvent for block A and a poor solvent for the block B, in order to decrease the total free energy of the system, the A blocks tend to stretch into the solvent and the B blocks tend to segregate against the solvent in order to minimize the energetically unfavored interaction with the solvent. The B blocks therefore form a core phase while the A blocks form a corona or shell, resulting in the formation of spherical polymer aggregates. In aqueous solution, attachment of a water soluble polymer to an insoluble polymer leads to the formation of micelles of resulting amphiphilic block copolymer. Two extremes of micellar structures can be distinguished for diblock copolymers, depending on the relative length of the blocks. If the soluble block is larger than the insoluble one, the micelles formed consist of a small core and a very large corona, and are thus called 'star-micelles'. By contrast, micelles having a large insoluble segment with a short soluble corona are referred to as 'crew-cut micelles' [6]. (Figure 1)

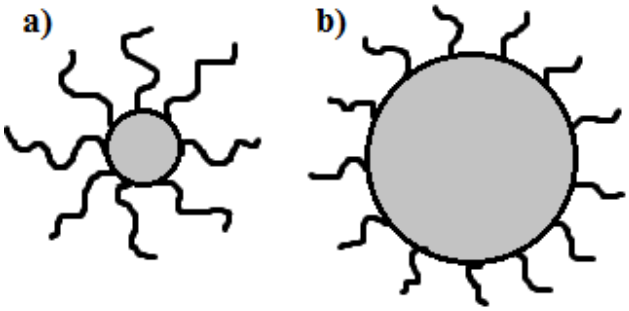

Figure 1: Schematic representation of two extreme morphologies of micelles depending on the relative block lengths: (a) star micelle, (b) crew-cut micelle.

It is well known that micellization occurs in dilute solutions of block copolymers in a selective solvent at a fixed temperature above a concentration called the critical micelle concentration, cmc, which is also called the critical association concentration for polymeric micelles. Block copolymers in a selective solvent form micelles via a closed association process, characterized by a certain cmc, below which only molecularly dissolved copolymer is present in solution, usually as unimers. Above cmc, multimolecular micelles are in equilibrium with the unimers.

The morphology of block copolymers in the solution depends on the volume fraction

of the different blocks. The morphological transition of diblock copolymer self-assemblies in aqueous dispersions associated with the variation in the volume fraction of a block was first reported by Eisenberg and coworkers [7]. By increasing the volume fraction of polystyrene (PS) in a polystyrene-*b*-poly(acrylic acid), PS-*b*-PAA, diblock copolymer, the morphology of the aggregates changed progressively from spheres to cylinders, to bilayers (both vesicles and lamellae), and eventually to compound micelles consisting of an assembly of inverted micelles surrounded by a hydrophilic surface. For a block copolymer of a given composition, solvent interaction parameters that drive self-assembly properties can be tuned by changing solvent composition. An example of the effect of solvent composition on the morphology of diblock copolymer self-assembly was reported by Zhang and coworkers [8]. By changing the volume ratio between water and acetone, the self-assembly of polystyrene-*b*-poly(acrylic acid-co-methyl acrylate), PS-*b*-P(AA-co-MA), undergoes a morphology transition from core-shell spheres, to porous spheres, and finally to core-shell cauliflower-like aggregates. Other parameters that can affect the morphology of block copolymers include pH and ionic strength, especially in the case of block polyelectrolytes. The pH values infuence de-protonisation and thus the charge density of weak polyelectrolytes and the ionic strength affects polymer aggregation by screening the effect of electrostatic repulsion [9].

Block copolymer self-assemblies could be prepared following two different protocols. One of them consists in dissolving the block copolymer in a solvent which is good for both blocks and subsequently a block selective solvent is added under vigorous stirring until micellization occurs. The second technique consists in direct dispersing the block copolymer in a block selective solvent. During the preparation of the block copolymer self-assemblies, the mobility of the polymer chains might be frozen at a certain solvent composition, resulting in products that are not thermodynamically stable. When changing parameters affecting the behavior of an associating block copolymer system, polymer chain mobility may become highly restricted in many cases, which prevents the system from achieving equilibrium. This allows for isolation of nonequilibrium, kinetically trapped self-assemblies which are stable on quite long timescales. The stability of kinetically trapped self-assemblies in principle allows for the preparation of various nanoparticle morphologies from a single copolymer sample using different preparation protocols [10].

Self-assembled block copolymers are used in a variety of applications including drug delivery and controlled drug release [11,12], nanopatterning and lithography [13,14] and in a preparation process of many tailor-made materials. Nano-engineering of new block copolymers can allow for the preparation of polymeric micelles with integrated smart, stimuli-responsive and targetable functions. Block copolymers could be also used as stabilizers for the preparation of various colloidal particles, for example based on nano-sized inorganic crystals [15-19]. The latter application is based on the preferential adsorption of one of the blocks onto the surface of the crystal, while the other block interacts with the solvent. Similarly, block copolymers can stabilize droplets in either water-in-oil or oil-in-water emulsions [20-22].

2.1.1 BLOCK POLYELECTROLYTES

Polyelectrolyte block copolymers combine structural features of polyelectrolytes, block copolymers, and surfactants. They possess quite unusual and unique properties which make them a challenging subject for researchers. In dilute aqueous solutions, polyelectrolyte block copolymers self-assemble into micelles consisting of a hydrophobic core and a polyelectrolyte shell. Micelle formation and micellar structure depends on various parameters like temperature, salt concentration, pH, and solvent quality, which are of relevance in many technological and biological processes. Important instrinsic parameters of the copolymer that control the size of micelles are the degree of polymerization of the polymer blocks and the Flory-Huggins interaction parameter, χ. Spherical micelles are not the only association structure that is formed by polyelectrolyte block copolymers. With increasing hydrophobic block length there is a tendency to form block copolymer vesicles, polymersomes, which are structurally very similar to bilyer lipid vesicles [23-25]. Most of block polyelectrolytes have the surprisingly low solubility when directly dissolved in water. It became a common practice to use organic co-solvents for the dissolution of the polymers, followed by dialysis to obtain stable micelles in pure aqueous solutions. “Frozen” micelles remain a major problem when investigating micellar properties since they do not correspond to the state of thermodynamic equilibrium. On the other hand, their structure is frozen, so their micellar state can be kept constant when varying external parameters, ionic strength or temperature [26].

2.1.2 DOUBLE HYDROPHILIC BLOCK COPOLYMERS (DHBC)

Double hydrophilic block copolymers (DHBC)s are a class of polymers, which have attracted attention of many researchers thanks to their tunable solubility in aqueous media [27-39]. DHBCs, in general, are fully soluble under certain conditions, but they can be turned to amphiphilic BCs by change of pH, ionic strength or temperature, which triggers their association and formation of well-defined structures, for example core-shell micelles in aqueous solutions, surface layers, etc. Thanks to that, DHBCs have been widely used in various applications including drug delivery systems, surface coatings and nanoreactors. The most frequently studied DHBCs include (meth)acrylic acid- and N-isopropylacrylamide based diblock copolymers, that have been often reported as pH- (PMAA, PAA) and thermoresponsive (PNIPAM) [35,36]. It was found that poly(ethylene glycol)-block-poly(N-isopropylacrylamide) (PEG-*b*-PNIPAM) [36] and poly(N-isopropylacryl-amide)-block-poly(acrylic acid) (PNIPAM-*b*-PAA) [37] diblock copolymers form PNIPAM-core micelles at high temperatures, above 32 °C, at neutral pH and in alkaline solutions. Poly(ethylene glycol)-block-poly(methacrylic acid) (PEG-*b*-PMAA), form PMAA-core micelles at low pH values due to desolvation of nonionized carboxylic acid groups of PMAA [D38]. Numerous examples of novel water-soluble diblock copolymers with weak basic blocks of tertiary amine methacrylates and their selectively quaternized derivatives have also been reported [28,29,39]. Butun and coworkers [28] studied so-called „schizophrenic“ block copolymers in which individual blocks can be tuned independently to become either hydrophilic or hydrophobic by changing the solution pH, temperature or ionic strength. The chains of the latter type of copolymers can self-assemble in dilute aqueous solution in the absence of any organic co-solvent to form two distinct micelle structures. In the first reported example [29], the ‘schizophrenic’ diblock copolymer was based on two tertiary amine methacrylates, namely 2-(diethylamino)ethyl methacrylates (DEA) and 2-(N-morpholino)ethyl methacrylate (MEMA). It was demonstrated that PDEA-*b*-PMEMA diblock copolymer disolves molecularly in dilute aqueous solution at pH 6 and 20 °C. Under these conditions, the neutral PMEMA block is hydrophilic and nonionic, whereas the PDEA block is

protonated and soluble as a cationic polyelectrolyte. At pH 8.5, the PDEA block is deprotonated and becomes hydrophobic, leading to PDEA-core micelles. On the other hand, if a suitable electrolyte is added to the original solution at pH 6, the PMEMA block can be selectively salted out to produce PMEMA-core micelles.

2.2 POLYMER – SURFACTANT COMPLEXES

It is customary to classify polymer-surfactant interactions according to charge of polymer or surfactant, and according to concentration region. Most studies concerned with the determination of surfactant binding to polymers are carried out at low polymer concetration, with surfactant concentrations determined by the binding region. On the other hand phase equilibria and phase diagrams are normally studied at higher concentrations.

At an early stage of the research in the field of polymer-surfactant interaction in general, it was recognized that in the polymer-surfactant complex the properties of both the surfactant micelles and the polymer are mutually modified. The most important aspect with respect to industrial applications was the fact that the solubilization power as well as the viscosity of an aqueous solution of polymer-bound surfactant micelles are higher than those of the separate surfactant and polymer solutions [40,41]. In 1957, Saito published the first extensive study on polymer-surfactant complexation [41]. He observed an increase in viscosity of an aqueous poly(vinylpyrro1idone) (PVP) solution upon addition of sodium dodecyl sulfate, SDS, and an increase in solubilizing power of SDS solution upon addition of PVP. Though it was suggested that the aggregation of sufactant molecules in the presence of the polymer resembled normal micellization, Saito proposed that, at a low surfactant-to-polymer ratio, the surfactant molecules bind individually to the polymer. The major concept emerged in the following decade was the picture of individual molecules along the polymer, with some kind of micellization occurring above the critical micelle concentration, cmc, of the surfactant in pure water. Many details of polymer-micelle interaction were revealed in next period, including the finding that complexation takes place even below the normal cmc. In 1977, Cabane established the polymer-micelle model as it is now quite generally accepted [42]. He studied the interaction of large, non-ionic macromolecules (PEO)

with small anionic surfactant micelles (SDS) using neutron scattering and NMR. In dilute solutions of PEO and SDS, only isolated macromolecules adsorbed on the surfaces of spherical micelles of surfactant were found. Figure 2a gives a schematic representation of the model Cabane studied the PEO/SDS system using ^{3}C, ^{1}H, and ^{23}Na NMR [43]. Depending on the amount of SDS in the solution, each macromolecule bound to one or more micelles of SDS. The distances between neighbouring micelles within one aggregate are determined by a competition between intermicellar forces. When the second virial coefficient for the intermicellar interactions is zero, the distribution of micelles within one aggregate closely follows the Gaussian distribution of the free polymer [44]. Figure 2b shows a tentative picture of such an aggregate. For linear polymers, a general model which has become accepted as a typical structure of polymer-surfactant complex is often referred to as the „necklace“ or „beads on a string“ model, in which one or more small micelles of surfactant reside within the random coil of the polymer.

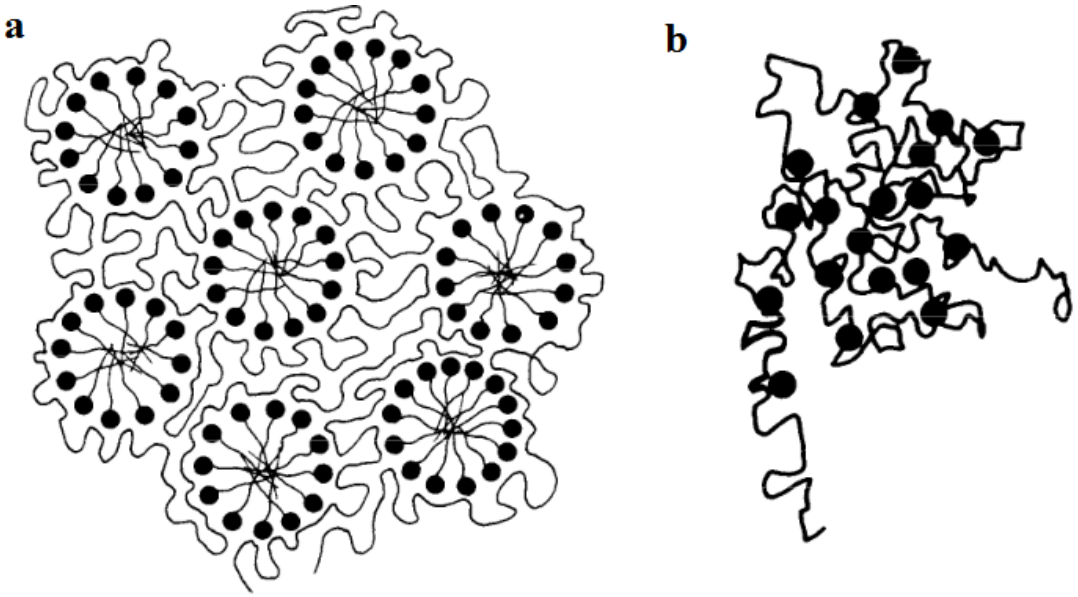

Figure 2: Schematic representation of the topology of polymer-micelle complexes in aqueous solutions [43].

Polymer-surfactant interactions used to be now described by two critical values of concentration. The critical aggregation concentration (cac, sometimes referred to as C1) at which binding of the surfactant to the polymer is starting and the second

critical concetration (C2), when the polymer is saturated with surfactant micelles. In the polymer-surfactant system, the critical micellization concentration of the free surfactant (cmc or Cm) could also be observed, but this value is generally higher than cac or coincident with C2. For example, for polyelectrolyte-surfactant systems of opposite charges, binding of the surfactant may occur at concentrations two or three orders of magnitude below the cmc.

The determination of the cac can be made by various methods as conductometry [45], calorimetry, surface tension measurements and potentiometry [46]. The most direct method for the determination of the cac, potentiometry, makes use of surfactant selective electrodes, which measure the concentration of free surfactant (not bound to polymer) in the solution, C_f. If we define C_p as concentration of the polymer and C_s as analytical concentration of the surfactant, the degree of binding β, number of surfactant molecules bound per polymer charged group is given by $\beta = C_b/C_p$, where C_b represents the concentration of the bound surfactant, $C_b = C_s - C_f$. The $\beta(C_f)$ function is called the binding isotherm, and has a sigmoidal shape. The binding of the surfactant could be described by cooperativity, u, which is characterised as a ratio between the probability of surfactant binding to a monomer unit adjacent to a monomer unit with the bound surfactant molecules, and the probability of binding to a monomer unit surrounded by monomer units without the bound surfactant molecules. The cac is usually defined as the concentration at which the response of the electrode deviates from that of the pure surfactant solution. This determination is accurate when association is very cooperative, that is, at large u. When u is of the order of unity, the cac is less well defined. In these cases, determinations by different methods may differ [47].

In general, the cac decreases with increasing surfactant chain length (as the cmc) and the cooperativity increases. Addition of salt increases both the cac and the cooperativity. Increasing polyelectrolyte concentration produces the same effect, because it leads to self-screening of electrostatic interactions. At high salt concentrations (above about 0.1 M), association no longer occurs. The cac decreases and the cooperativity increases also with increasing charge density of the polyelectrolyte [46,48,49].

2.2.1 POLYELECTROLYTE – IONIC SURFACTANT COMPLEXES

Polyelectrolyte-surfactant (PE-S) systems are involved in a wide range of applications, including personal and domestic care products, pharmaceutical formulations, and medical and biotechnological uses. The richness of their properties made them commonly used in everyday household products and cosmetics, such as shampoos and laundry detergents. Because of the fact that the benefical use of PE-S complexes depends on understanding and controlling the intermolecular interactions between them, they have been studied extensively for many years and several reviews were already published [47,50,51], in order to summarize a general understanding of the interactions between polyelectrolytes and surfactants in solution.

The strong electrostatic attraction between oppositely charged polyelectrolytes and surfactants is clearly observable and occurs at a concentration several orders of magnitude below the critical micelle concentration of surfactant in pure water. This concentration is called critical aggregation concentration, cac, and is defined as concentration at which point binding of the surfactant to the polymer first occurs. Above cac, the strong interactions between surfactants and oppositely charged polyelectrolytes lead to partial collapse of the polymer chains and to the formation of multichain complexes. These complexes are dense and monodisperse if the polymer is moderately rigid and non-branched, if the surfactant chain length is small and if the polymer-surfactant ratio is small. Otherwise, the complexes are large, soft, dilute and polydisperse [47].

Phase separation is frequently is observed in polyelectrolyte-surfactant systems, either associative or segregative. In the former case, mixed polyelectrolyte-surfactant aggregates are formed, while with segregating systems, separate polyelectrolyte structures and surfactant micelles are present. The behaviour observed depends upon the balance between the various attractive and repulsive forces present. Polymers in the solution and also surfactants in the form of self-assemblies with large aggregation numbers are both characterized by low translational entropy. In the absence of an attractive polymer-surfactant interaction, mixed solutions are expected to have the tendency to segregative phase separation. This is typical for mixed solutions of

a nonionic polymer with a nonionic surfactant. Nevertheless, PE-S mixtures are typical examples of systems displaying an associative phase separation. It is generally accepted that a major driving force for the strong association between charged polymers and oppositely charged micelles comes from the entropy gain of releasing the counterions associated with them and their transfer into the bulk solution [52]. Another driving force is hydrophobic interaction, which plays an important role in case of amphiphilic polymers, for example for hydrophobically modified water soluble polymers [51]. In addition, it is likely that hydrogen bonding may also play a role, particularly in complexing with nonionic surfactants [53].

The associative phase separation occuring for systems of oppositely charged polymer and surfactant leads to one dilute and one concentrated phase. The concentrated phase can be solid or liquid depending on the system, but typically it has a liquid crystalline nature. Lamellar, hexagonal and also cubic structure have been identified [54]. Associative phase separation can also be the basis for formation of homogenous particles, core-shell particles or polymer gels by physical cross-linking. By addition of small drops of a concentrated solution of a polyelectrolyte into a surfactant solution, gel particles in a size range of 100 nm to mm can be formed [51].

Many factors can influence the phase behaviour of polyelectrolyte-surfactant mixtures such as molecular weight, degree of branching, charge density, backbone rigidity and concentration of the polymer, as well as polar head, chain length and concentration of the surfactant. The role of added salt is also important since electrostatic interactions are partially screened when salt is present. It was found that the complexation depends not only on salt concentration, but also on the nature of salt ions, valency and type (for instance, the rank in the Hofmeister series) [47]. Some theoretical and experimental studies have been reported on the effect of chain rigidity on polyelectrolyte-surfactant interactions. Wallin and Linse studied complexation between charged surfactant micelles and oppositely charged polyelectrolytes by using Monte Carlo simulation [55]. They tried to calculate the ratio between cmc and cac, the concentration at which surfactant starts micellization alone and in the presence of polyelectrolyte. As a result, they presented that the cac could be between 4 and 60 times lower than cmc depending on the rigidity of polyelectrolyte. For rigid polyelectrolyte, the difference is not so high as for flexible polyelectrolyte. The cac increase with the chain rigidity. This result confirmed that

flexibility of the polyelectrolyte affects the structure of the formed complexes.

Most attention in the field of PE-S complexes has been paid to polyelectrolyte homopolymers [56-58]. It was found that their behaviour is determined mainly by the charge-molar ratio of the surfactant to the polyelectrolyte, *Z*. Nonstoichiometric PE-S complexes with excess free polyelectrolyte units ($Z<1$) or excess surfactant molecules ($Z>1$) are generally water-soluble. Stoichiometric complexes with zero net charge ($Z=1$) precipitate from aqueous solutions and can be dissolved only in organic solvents. At $Z<1$, the size of the polyelectrolyte coils decreases as compared to surfactant-free polyelectrolyte solution as a result of decreased net charge density and reduced electrostatic repulsion. Studies of interactions between weak polyelectrolytes and surfactants showed that polycarboxylic acids, such as PAA, PMAA and their derivatives, have surprisingly strong affinity to cationic surfactants. Nanostructures formed on the basis of these interactions could be considered as stimuli-responsive materials, because their stability and properties depend on the pH of the solution. By varying the degree of protonisation, it is possible to modify the charge density, hydrophobicity and backbone flexibility of the weak polyelectrolyte chains. However, since the pH values of the polyacid solutions change with the addition of surfactant, carrying out quantitative analysis of the influence of pH on the binding interactions is quite difficult. To solve this problem, it is necessary to study interactions in buffer solutions, where the pH values remain constant over the entire course of binding. It was reported by several researchers that hydrogen bonds are involved in the complexation of poly(carboxylic acids) with oppositely charged surfactants [57,59,60]. Hydrogen bonding plays an important role at low pH, where the poly(carboxylic acids) are weakly ionized. With increasing pH and increasing degree of deprotonization of the polyacid, the contribution of hydrogen bonding to the binding is superimposed on the electrostatically controlled polymer-surfactant interaction [59]. The role of hydrogen bonding in the formation of weak polyelectrolyte-surfactant complexes were confirmed by performing isothermal titration calorimetry (ITC) studies at various different temperatures for PAA-DTAB system. In the binding region at low degree of protonization, a significant exothermic peak in the ITC profile was found, the position and height of which were essentially independent of the temperature, which corresponds to the interchain complexation via hydrogen bonding. It was suggested by the authors of this study that the reason

for interchain H-bonding may be the change in the polarity of the polymer upon the binding of ionic micelles on the polymer backbone. Without the addition of surfactant, the unionized PAA chains are apolar and they tend to form a compactly coiled structure to minimize their contact with water molecules due to hydrophobic effect. The binding of DTAB micelles onto PAA chains with their cationic headgroups enhances the polarity as well as reduces the hydrophobicity of the PAA backbone, which expands the polymer chain. Thus, a more H-bonding-friendly environment in aqueous medium is established, and the interchain complex is formed [57]. The significance of hydrogen bonding in the mixtures of weak polyelectrolyte and nonionic surfactants was also published [60,61].

Nanoparticles formed by polyelectrolyte-surfactant complexes could be used as versatile nanocarriers of various substances. Due to the hydrophobic interior, the slightly charged or uncharged (neutralized) PE-S nanoparticles could act as nanocontainers for some hydrophobic drugs in aqueous media. To achieve this ability, it is necessary to prevent the nanoparticles from aggregation. An important feature of interactions between polymers and oppositely charged surfactants is that in certain charge ratio or concentration range PE-S complexes precipitate from dilute solutions. As surfactant binds to the polymer, neutral insoluble complexes come out of the solution. In some cases redissolution of these complexes is possible upon addition of higher amount of the surfactant. This will occur if the polymer has a partly hydrophobic character and can bind the surfactant micelles in amounts exceeding the charge stoichiometry [62]. Spontaneous overcharging in polyelectrolyte-surfactant complexes, involving adsorption of flexible chains on oppositely charged cores, is a phenomenon which has been observed both experimentally [63] and by simulation techniques [64,65]. It is an entropic effect associated with release of the counterions of the highly charged polyelectrolyte chains. The electrostatic energy of the macro-ions which favours electroneutrality competes with the counterion entropy upon overcharging. Close to the local isoelectric point, characterized by low effective charge density of the complex, the free energy of the complex is low and further adsorption is favoured by the gain in entropy upon counterion release. The effect of this competition results in the net charge of the complex with the same sign as that of the flexible chain. This spontaneous under- or over- charging should be observed with flexible (and semi-

flexible) polyelectrolyte-colloid complexes, including biological assemblies. The most intriguing biological examples involve complexes of DNA with various proteins, which control gene replication and regulation.

The redissolution of water-insoluble polyion−surfactant ion complexes by excess of the surfactant has been investigated systematically in both experimental and theoretical phase equilibrium studies. The efficient redissolution found for certain copolyion systems was explained by the formation of soluble polyion−surfactant ion complexes carrying an excess of surfactant ions through an additional hydrophobic attraction. This redissolution is, however, not possible for entirely hydrophilic polymers [66].

Addition of nonionic amphiphilic block copolymers can prevent PE-S complexes from aggregation. A Pluronic-type triblock copolymer (PEO-PPO-PEO) was used by Pojjak and Meszaros to prevent the aggregation of branched poly(ethylenimine) (PEI) – sodium dodecyl sulfate (SDS) complexes. The full suppression of precipitation was reached due to the formation of sterically stabilized dispersions of uncharged PEI-SDS nanoparticles with an hydrophobic core and hydrophilic corona [67]. The first phase diagram of a polyelectrolyte-surfactant system was published in 1990 by Thalberg and co-workers and opened a route to better understanding of polyelectrolyte-surfactant interactions [68].

2.2.2 POLYELECTROLYTES AND NONIONIC SURFACTANTS

Interactions between polyelectrolytes and nonionic surfactants are generally weak [40]. However, if the polyelectrolyte has hydrophobic domains, it is suggested that there may be attractive interactions with the nonionic surfactants leading to association. In the case of nonionic surfactant we have to take into consideration both noncooperative and cooperative binding of surfactant to polymer. It was found that in some specific cases the critical association concentration (cac) seems to be higher than cmc of free surfactant. This fact could be ascribed to the hydrophobic microdomains of the polymer coil in water (for example PMAA), probably in its interior. It is considered that some surfactants are bound first to these hydrophobic microdomains noncooperatively and after that, at specific critical concentration cac*, an abrupt transition to cooperative binding occurs. When the cmc of free surfactant is

low and the amount of the surfactant bound into the hydrophobic microdomains is relatively large, it could raise the cac* value higher than cmc. In comparison with PAA, cac* for the PMAA + nonionic surfactant system consists of the amount of noncooperative binding and the cac of the cooperative binding in equilibrium. Therefore, this cac* has a different meaning from that for PAA and should be called the apparent cac. The amount of the surfactant bound by hydrophobic microdomains and also the value of the cac* is dependent on the PMAA concentration. The measurements of cac* at various PMAA concentrations and extrapolation of the cac* value to that for the zero PMAA concentration allows for finding the realistic value of the cac, corresponding to cooperative binding. This value was found to be lower than the respective cmc [61].

2.2.3 BLOCK POLYELECTROLYTES – SURFACTANT COMPLEXES

For practical applications of PE-S complexes, it is desirable to prevent their aggregation and the formation of precipitates. It is well known, that aggregation could be fully supressed for mixtures of ionic surfactants with appropriate block polyelectrolytes, called double-hydrophilic block copolymers, consisting of a polyelectrolyte block and a neutral hydrophilic block. Mixing of such block polyelectrolytes with oppositely charged surfactants in aqueous solutions leads to the formation of self-assembled nanoparticles. The pioneering works on this field of investigation were done by Kabanov and co-workers [69-71], who have demonstrated the preparation of water-soluble stoichiometric nanocomplexes of various block copolymers with oppositely charged surfactants. Depending on the properties of both ionic and nonionic block, as well as on the type of surfactant, these complexes can exhibit different self-assembly behaviour and create various types of supramolecular structures, such as core-shell micelles [69,70] or vesicle-like aggregates [71,72]. In the former case, micelles are formed by the hydrophobic core and hydrophilic corona. The insoluble core of the nanoparticles is a disordered microphase formed by densely packed surfactant micelles connected by the polyelectrolyte blocks, which overcompensate the charge of the micelles. The core is surrounded by nonionic blocks of the copolymer forming shell of the nanoparticles. Vesicle-like aggregates are composed of a nonionic corona and a surfactant-

neutralized polyanion shell. Both the length of the neutral block and the number of nonionic groups that can lyophilize the electroneutral PE-S complex have important influence on the solubility of these nanostructures.

Studies of PE-S of block polyelectrolytes have received considerable attention in the last decades [73-76]. It was found that the overall size of the nanoparticles depends on the molar mass of the whole block copolymer, but the core radius is driven only by the polymerization degree of the polyelectrolyte block and does not depend on the length of the shell-forming neutral block [75]. It has also been reported that the size and structure of PE-S core/shell nanoparticles formed by block polyelectrolytes depend on the sample history, which suggests a nonequilibrium nature of these systems [76]. The structure of nanoparticles depends also on the conformational rigidity and charge density of the polyelectrolyte block. A higher density of charges and the presence of the bulky units in the chain can cause the limited mobility of the polyelectrolyte block which can prevent it from the transition into the core-shell structure [77].

2.3 SUPERPARAMAGNETIC IRON OXIDE NANOPARTICLES (SPION)S

Materials whose physical properties can be varied by application of external magnetic fields belong to a specific class of smart stimuli-responsive materials. The broad family of magnetic field-controllable materials includes ferrofluids (magnetic fluids), magnetic polymers, magnetic inorganic materials and magnetically modified biological structures. In many cases magnetically responsive materials consist of small magnetic particles, usually in the nanometer to micrometer range, dispersed in a polymer, biopolymer or inorganic matrix. In recent years, considerable attention has been paid to iron oxide magnetic nanoparticles (most often formed by magnetite and maghemite), due to their magnetic properties, such as high susceptibility and superparamagnetism, non-toxicity and biocompatibility. These properties allow for using iron oxide nanoparticles in various biomedical applications and biotechnologies [78], for example in separation processes, drug delivery, cancer treatment and magnetic resonance imaging (MRI).

Magnetic nanoparticles (MNP) can be selectively removed from the complex

samples using external magnetic field. This process is very important for bioapplications due to the fact that absolute majority of biological materials have diamagnetic properties which enable efficient selective separation of magnetic materials. According to magnetic properties of iron oxide nanoparticles, it is possible to separate the target biomolecules using the external magnetic field (permanent magnet, electromagnet) instead of time-consuming centrifugation or precipitation. To fulfill the criteria as a separation tool, the clustering of MNPs is an important issue. Moeser et al. reported that the individual polymer-coated MNPs with magnetic core diameters of 7.5 nm could not be permanently trapped in a magnetic separator. However, clusters of these MNPs of size greater than 50 nm could be permanently trapped and used effectively in the separation process [79]. Several ways to prepare MNP clusters have been employed with the preparation protocols containing more than one step. The preparation of stabilized individual MNP is first required, which are used in a second step for the formation of clusters [80]. In some procedure the individual MNP could be stabilized in organic solvent by hydrophobic compound, such as oleic acid, and subsequently, after solvent exchange, the clustering process is carried out in aqueous media, with [81] or without an addition of surfactant [82].

Magnetic particles can be targeted to the desired place and kept there using an external magnetic field, which could be used for magnetic targeting and drug delivery. They could be used also for the cancer treatment, called magnetic fluid hyperthermia [83]. These method is based on the generation of the heat during exposure magnetic particles to high frequency alternating magnetic field. Magnetic iron oxide nanoparticles generate a negative T2 contrast during magnetic resonance imaging (MRI), so they are used as efficient contrast agents. Magnetic nano- and microparticles can be used for magnetic modification of diamagnetic biological materials, such as cells, organic polymers and inorganic materials, and for magnetic labelling of biologically active compounds, for example antibodies or enzymes [84].

Different chemical routes for the synthesis of superparamagnetic iron oxide nanoparticles and their use for the preparation of magnetically responsive materials have been reviewed [85]. Many chemical procedures have been used to synthesize magnetic nanoparticles, such as classical co-precipitation, sol-gel syntheses, hydrothermal synthesis, electrochemical methods, hydrolysis and thermolysis of precursors and mechanochemical processes.

Chemical co-precipitation of iron salts seems to be one of the most promising pathways to obtain magnetic particles because of its simplicity, relatively low cost and high productivity [86,87]. Iron oxides, either in the form of magnetite (Fe_3O_4) or maghemite (γ-Fe_2O_3), are usually prepared by aging stoichiometric mixture of ferrous and ferric salts in aqueous alkaline solution. The chemical reaction of Fe_3O_4 formation is usually written as follows:

$$Fe^{2+} + 2\ Fe^{3+} + 8\ OH^- = Fe_3O_4 + 4\ H_2O$$

However, magnetite is not very stable and is sensitive to oxidation which results in the formation of more stable maghemite. It was reported that co-precipitation in carefully controlled conditions such as particular concentration of iron salts, pH value of the solution, reaction temperature or stirring rate can lead to iron oxide particles of desired size and shape.

A simple and facile microwave method to prepare relatively monodisperse magnetic Fe_3O_4 and Fe_3O_4/Ag NPs was published [88,89]. It is known that microwave irradiation does not only heat the reaction mixture but in many cases also enhances the reactivity. A wide variety of chemical reactions accelerated by microwave irradiation on reactants have been observed [90]. In comparison with conventional heating method, reactions under microwave irradiation have the significant advantages of higher reaction rates and product yields in a shorter period of time. The formation of magnetic Fe_3O_4 NPs using microwave method requires only a few seconds or minutes. This is much faster than other reported methods such as thermal decomposition, micelle synthesis and hydrothermal synthesis since they all need several hours or days for reactions [91]. Different from other, not only microwave-assisted methods, that employed both Fe^{2+} and Fe^{3+} ions as precursors, these works [89,90] used Fe^{2+} only. Thanks to that, the synthetic condition was much simpler and the quality of the prepared MNPs was not affected by the initial stoichiometric ratio of Fe^{2+}/Fe^{3+}.

To obtain biocompatible magnetically responsive materials, it is usually necessary to stabilize the prepared iron oxide nanoparticles by appropriate modification of their surface or by their incorporation into appropriate biocompatible matrix. As these nanomaterials have large surface-to-volume ratio, stabilization against aggregation

is very challenging. Several compounds with carboxylic [92], phosphate [93] and sulfate [94] groups are known to bind to the surface of magnetic particles and stabilize them. Citric acid can be used to stabilize water-based magnetic fluids by coordinating via one carboxylic group. Other carboxylic groups exposed to the solution can be responsible for making the surface negatively charged and hydrophilic. Other ferrofluids can be stabilized by ionic interactions, using for example perchloric acid or tetramethylammonium hydroxide [95].

2.3.1 COMPLEXES OF SPIONS WITH BLOCK COPOLYMERS

Block copolymers can be used as stabilizers for magnetic nanoparticles. Several publications describing preparation, coating and co-assembly of SPIONs with amphiphilic [96-100] and double hydrophilic block copolymers have been published [16,17,80,101,102]. Co-assemblies of SPIONs with amphiphilic block copolymers may have various sizes and structures depending on the molecular weight of the polymer blocks, relative volume ratio between hydrophilic and hydrophobic parts, charge ratio between nanoparticles and polyelectrolyte blocks and also on solvent composition. Based on the fact that charged SPIONs interact with the polyelectrolytes, incorporation of the SPIONs into the polyelectrolyte block copolymers affects the self-assembly behaviour of the copolymers by modifying the relative volume ratio between the hydrophobic block and the hydrophilic block. Controlling the solvent-nanoparticle and polymer-nanoparticle interactions, Hickey and coworkers prepared co-assemblies of SPIONs and PAA-*b*-PS with several different morphologies, including homogeneous magneto-micelles, magneto-core shell structures and magneto-polymersomes (Figure 3) [97,99,100].

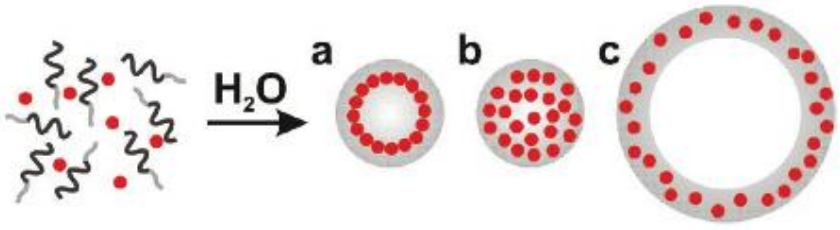

Figure 3: Various magneto-structures made of SPIONs with PAA-*b*-PS [97].

Double hydrophilic block copolymer, PEO-*b*-PAA, was used to prepare aqueous solution of magnetic nanoparticles by one-pot synthesis method, where the copolymer controlled the particle growth and played as a stabilizer and also as a clustering agent. It was found that depending on the iron-to-polymer ratio, the nanoparticles can grow in the form of colonies of small iron oxide particles of about 10 nm or bigger homogeneous and regular spherical clusters of these small particles with the size larger than 100 nm. The clustering phenomenon was related to the van der Waals attraction. An insufficient polymer coverage induced an instability in the system as the polymer coatings do not sufficiently screened this attraction. The bridging of particles was possible due to ability of one polymer chain to adsorb simultaneously onto more iron oxide particles to form clusters rather than to cover a single individual iron oxide particle [80].

DHBC can be used for additional stabilizing SPIONs in aqueous dispersions also by mixing electrostatically stabilized coated SPIONs with an oppositely charged DHBC. Electrostatic co-assembly of both components leads to the formation of mixed nanoparticles with protective shell formed by the neutral blocks of the DHBC and core formed by the complex of SPIONs with polyelectrolyte blocks (Figure 4) [101]. The structure of formed nanoparticles is similar to PE-S complexes, but a noticeable difference is in their polydispersities. The dispersity of nanocomplexes formed by magnetic nanoparticles is much larger than in the case of complexes with surfactants, which probably originates from the broader distribution of the sizes of mineral nanocrystals.

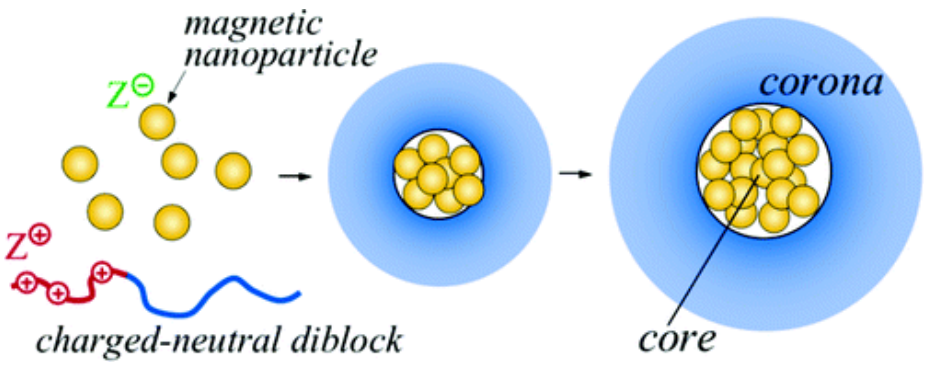

Figure 4: Core-shell nanostructures formed by DHBC with SPIONs [101].

2.4 AGGREGATION OF COLLOIDAL PARTICLES

Aggregation of colloidal particles has been of fundamental interest to many academic and industrial researchers for many years. Because of the fractal structure of the colloidal aggregates, the advent of fractal mathematics has resulted in a great progress in this field of study [103,104]. There are two different regimes of colloidal particles aggregation, diffusion-limited cluster-cluster aggregation (DLCA) and reaction-limited cluster-cluster aggregation (RLCA). The former describes cluster formation of Brownian particles following random walks with a high probability of intercepting an arm of the cluster as the particle moves from an exterior point to a point deep inside a growing cluster or aggregate. Therefore, the growing arms screen the interior of the cluster from the incoming particles. As a consequence, a particle is more likely to stick near the outside of the cluster than to penetrate near the centre, resulting in a very open structure. Because a large number of diffusing clusters exist at any given time, they can grow by sticking to each other as well as from single particle addition [105].

It is also possible for the aggregation rate to be limited by the probability that particles will stick upon contact. If the collision efficiency is very small, the clusters will need to collide many times before they stick and this allows the diffusing clusters to penetrate further into each other before sticking. This type of aggregation is commonly referred to as reaction-limited cluster-cluster aggregation. In the case of slow or reaction-limited cluster aggregation, the average cluster size grows exponentially with time, and the obtained clusters are more compact [106].

Both types of colloidal aggregates could be considered as fractal objects. The term *fractal* was used by Mandelbrot to describe the structure of many random materials which possess a special kind of complexity and can be characterized by a noninteger, fractal, dimensionality [107]. A fractal object is an object that is considered to be self-similar, meaning that the structure of the object is invariant to a change of scale. The fractal dimension corresponds to the degree of irregularity or the space-filling capacity of an object. Some materials, such as polymers, are known to be mass fractals, where the mass, M, is proportional to some fractional power, d_f, of the radius, R. Other materials, such as powdered coal, are surface fractals and have

a surface area that is proportional to some fractional power, d_s,of the radius, R.

$m(R) \propto R^{d_f}$

$A(R) \propto R^{d_s}$

Here d_f and d_s are called the mass and the surface fractal dimension, respectively, and are not limited to integer values, unlike ordinary mass-size relationships. The mass fractal dimension can be used also to characterize changes in mass density of the fractal object, $\rho(R)$, observed within a sphere of radius R centred at some point in the object:

$\rho(R) \propto R^{d_f-3}$, where $1 \leq d_f \geq 3$ for an object in 3-dimensional space. Compact objects have a d_f of 3, while open configurations of particles are characterized by smaller fractal dimensions [108]. Many materials in nature have fractal character, so the fractal growth phenomena are closely related to many processes of practical importance, for example to air and water pollution control. Fractal morphology was demonstrated for a range of particle aggregates including those of silica, gold, latex, clay, polymer and coal, among others.

In understanding the structure of the fractal aggregates a major role was played by a simulations and much of the knowledge about fractal growth was driven from computer modelling [104,109]. It was found that the aggregates formed by diffusion-limited cluster cluster aggregation have fractal dimension about d_f = 1.75 [105]. The low fractal dimensions of this DLCA model reflect the loose, open appearance of the aggregates formed. On the other hand, more compact aggregates formed by reaction-limited cluster aggregation have d_f values around 2.1 [106].

The first experiments that explicitly investigated the fractal nature of particle aggregates were based on the image analysis techniques of electron micrographes (TEM) of metallic oxide smoke particles made by Forrest and Witten [103]. The difficulty in these experiments was that the three-dimensional clusters were simply projected onto the two-dimensional TEM substrates. Schaefer and coworkers avoided the inherent limitations of the sample preparation required by microscopy methods by using light and X-ray scattering to measure the fractal dimension of colloidal silica aggregates [110]. Since their introduction, a wide variety of colloidal systems have been studied using scattering techniques, including for example polystyrene latex [108], gold [111] or hematite [112].

2.5 FUNDAMENTALS OF CHARACTERIZATION METHODS

This section reviews the fundamentals of methods for characterization of the studied polymers as well as the complexes that were built from these polymers with law-molar-mass compounds. The molecular weight, size and the shape of the complexes were analysed mainly by scattering techniques, particularly by static light scattering, dynamic light scattering, electrophoretic light scattering and small angle light, X-ray and neutron scattering. Because light scattering is associated with variations in dielectric properties, or refractive index, X-rays are scattered by electrons and neutrons are scattered by nuclei, each type of radiation has its own advantages as a probe of soft matter. The morphologies of the nanostructures, as well as their compositions, were studied by electron microscopy and atomic force microscopy.

2.5.1 Light scattering (LS)

A number of materials exist in the solution in the form of nanostructures with the size ranging from 1 to 1000 nm, which can be determined by dynamic light scattering. These materials include proteins, polymers, surfactants, emulsions and vesicles, as well as materials more traditionally considered as particles, such as clays, silica, pigments and inks. The phenomenon of light scattering has first been described theoretically by Lord Rayleigh in the 19th century [113]. Rayleigh discovered that the sky looks blue due to the fact that the short wavelengths of the visible spectrum of the sun light are scattered much stronger by the gas molecules in the atmosphere than the long wavelengths. Nowadays, light scattering is an effective non-destructive method used in physical chemistry of macromolecules and colloidal systems, providing information about macromolecules in solution, which are difficult to reach by other methods. Light scattering has become a very important analytical tool to determine molar mass, size and shape of nanoparticles [114]. Light scattering techniques are divided into static methods, which investigate the structure of the scatterers by measuring time-averaged angular dependences of the intensity of the scattered radiation, and dynamic methods which consist in following the dynamics of the scatterers by monitoring time fluctuations of the scattered light intensity.

2.5.1.1. Static Light scattering (SLS)

Light scattering is caused by oscillations of the induced dipole moment during the interaction of electromagnetic radiation (laser beam) with matter. During a static light scattering measurement, the dependence of the scattered light intensity on the so-called scattering angle, θ, between the direction of the primary beam and the direction of observation is recorded. In the regularly arranged systems, such as mono crystals, only radiation scattered in the same direction as the primary beam has non-zero intensity (scattering angle $\theta = 0°$). The radiation in other directions is suppressed by destructive interference. In liquids, which are disordered by thermal, density and (in the case of solutions) concentration fluctuations due to thermal motions of molecules, the light is scattered also in directions of non-zero angles. Particles small enough in comparison with the wavelength of scattered light ($d < \lambda/20$), scatter equally to all directions. For larger particles ($d > \lambda/20$), there are differences in the phase of the scattered light from various parts in the macromolecule, which lead to destructive or constructive interference in certain directions and to the angular dependence of the intensity of scattered light.

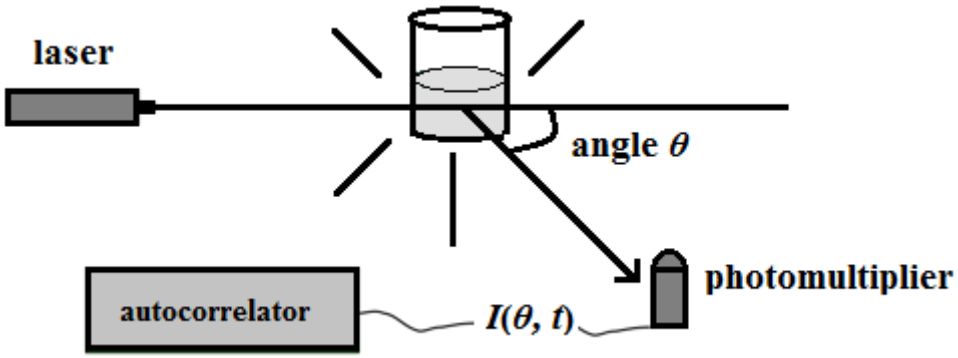

Figure 5: Schematic representation of traditional light scattering measurement.

The SLS measurement provides the so-called Rayleigh ratio, *R*:

$$R(q) = \frac{I(q)}{I_0} r^2 \quad (1)$$

where $I(q)$ is the time averaged intensity of scattered light per unit of volume as a function of the scattering vector, q. I_0 is the intensity of primary beam, r is the distance of the observer (detector) from the place of scattering, α_p is the polarizability of the molecules, and N_A is the Avogadro constant, representing the number of atoms, molecules, or ions in one mole of a substance. The scattering vector, q, is defined as:

$$q = \frac{4\pi n_0}{\lambda} \sin\frac{\theta}{2}, \quad (2)$$

where n_0 represents the refractive index of the solvent, λ is the wavelength of the incident radiation in vacuum and θ is the scattering angle at which we measure the intensity of scattering. The scattering from a solution is observed due to fluctuations of the polarizability, α_p, which could be caused by density or concentration fluctuations. In dilute solutions of polymers, the density fluctuations of the pure solvent contribute negligibly and could be subtracted from the measured signal. In fact the scattering intensity depends only on the scattering power of the dissolved particles and on the concentration fluctuations. It was shown by Debye [115] for a liquid two-component system that the polarizability is dependent on the refractive index increment of the sample with respect to the solvent, d*n*/d*c*, and on the osmotic pressure of the solution, Π, by equation:

$$\langle \Delta\alpha_p^2 \rangle \propto n_0^2 RTc \left(\frac{\mathrm{d}n}{\mathrm{d}c}\right)^2 \left(\frac{\partial c}{\partial \Pi}\right)_T. \quad (3)$$

R is the gas constant, T is the absolute temperature and c is the concentration. According to this equation, the Equation (1) could be written in a form:

$$\frac{Kc}{R(q)} = \frac{1}{RT}\left(\frac{\partial \Pi}{\partial c}\right)_T, \quad (4)$$

where K is an optical constant depending on refractive index, wavelength and polarization of the light:

$$K = \frac{4\pi^2 n_0^2}{\lambda^4 N_A}\left(\frac{\mathrm{d}n}{\mathrm{d}c}\right)^2. \quad (5)$$

According to van´t Hoff :

$$\frac{\partial \Pi}{\partial c} = \frac{k_B T}{M_w} \tag{6}$$

for ideal solution and

$$\frac{\partial \Pi}{\partial c} = k_B T \left(\frac{1}{M_w} + 2A_2 c + \cdots \right) \tag{7}$$

for real solutions, where k_B is Boltzmann constant, M_w is weight-averaged molar mass of dissolved particles and A_2 is a second osmotic virial coefficient, which gives an information about the interactions of particles in the solution and so about the excluded volume of one particle for another. For real solutions of small scattering particles with a diameter smaller then $\lambda/20$ it is finally obtained so-called Debye plot:

$$\frac{Kc}{R(q,c)} = \frac{1}{M_w} + 2A_2 c. \tag{8}$$

The intensity of scattered light is proportional to the product of the weight-average molar mass of the particles and their concentration in the measured solution. Measuring the scattering intensity at several angles brings an opportunity to calculate the root mean square radius, also called the radius of gyration, R_g. On the other hand, by measuring the scattering intensity for several various concentrations, the value of A_2, can be calculated. Because of the fact that the scattering intensity from larger particles is depending on the scattering angle, θ, an angular scattering function called particle form factor, $P(q)$, was defined as a power series:

$$P(q) = 1 - \frac{1}{3} q^2 \langle R_g^2 \rangle + \cdots = \sim \frac{1}{1 + \frac{1}{3} q^2 \langle R_g^2 \rangle} \tag{9}$$

where $\langle R_g^2 \rangle$ is the z-averaged square of the radius of gyration. This is a series expansion in q^2 where higher order terms are not shown explicitly. It can be shown that the absolute scattering intensity depends on $P(q)$ as:

$$\frac{Kc}{R(q,c)} = \frac{1}{M_w P(q)} + 2A_2 c + \cdots. \tag{10}$$

This is a series expansion in c. For comparatively dilute solutions, higher order terms in c can be neglected, however.

Inserting $P(q)$ from eq. (8) we get the very important Zimm-equation:

$$\frac{Kc}{R(q,c)} = \frac{1+\frac{1}{3}q^2\langle R_g^2\rangle}{M\left(1-\frac{1}{9}q^4\langle R_g^2\rangle^2\right)} + 2A_2c \approx \frac{1}{M}\left(1+\frac{1}{3}q^2\langle R_g^2\rangle\right) + 2A_2c. \quad (11)$$

This equation provides the basis for analyzing the scattered intensity from comparatively small particles, that is, for $q^2\langle R_g^2\rangle \ll 1$, in which case eq.(9) holds with sufficient accuracy. (For light scattering, this size regime is corresponding to: 10 nm < radius < 50 nm). Eq. (11) allow for evaluating the molar mass, the radius of gyration, R_g, or the second virial coefficient A_2, the latter providing a quantitative measure for particle-solvent interactions. For polydisperse samples the Zimm analysis yields the following averages:

Mass-average of the molecular mass M_w $$M_w = \frac{\sum N_i M_i^2}{\sum N_i M_i} \quad (12)$$

and z-average of the squared radius of gyration $$\langle R_g^2\rangle = \frac{\sum N_i M_i^2 \langle R_g^2\rangle}{\sum N_i M_i^2}. \quad (13)$$

The SLS data can be evaluated in several different ways (Zimm, Berry or Guinier plot) depending on the size of the scattering particles. If the size of the nanoparticles is larger than 50 nm, the plot of $P^{-1}(q)$ vs. q^2 is nonlinear even in the low q region and scattering data cannot be fitted according to the Zimm equation. In such cases, the Berry method based on plotting $(Kc/R)^{1/2}$ vs. q^2 or the Guinier method based on plotting $\ln(Kc/R)$ vs. q^2 can provide a linear dependence which allows for a reliable determination of the gyration radius.

Most data obtained by SLS measurements in this work were treated by the Guinier method neglecting the particle-solvent interactions by means of the equation:

$$\ln\frac{I(q)}{I(0)} = 1 - \frac{1}{3}R_g^2 q^2. \quad (14)$$

2.5.1.2 Dynamic light scattering (DLS)

Particles in solution show thermally incited diffusion, the so-called Brownian motion, as a result of random thermal density fluctuations of the solvent molecules.

These fluctuations push the scattering particles along and therefore cause a time-dependence of the intensity of scattered light per unit of volume. The particles in a liquid move about randomly and their speed of movement is connected with their size. It is known that small particles in a liquid media move or diffuse more quickly in comparison to the larger ones. Characteristically for the Brownian motion, also called a "random walk", the mean squared displacement of the scattering particles, $\langle \Delta R(t)^2 \rangle$, depends linearly on the time of motion *t*:

$$\langle \Delta R(t)^2 \rangle = 6Dt, \tag{15}$$

with *D* the self-diffusion coefficient of the particle.

Dynamic light scattering (DLS), also known as photon correlation spectroscopy (PCS), allows us to study the movement of scattering objects by measuring the temporal fluctuations of the intensity of scattered light. During the measurement, the number of photons entering the detector is recorded and analyzed by a digital correlator. This technique is sometimes called also quasi-elastic light scattering (QELS), because diffusive motion of the particles gives rise to the Doppler effects, broadening of the wavelength distribution of scattered light with respect to the incident light. The outcome of the measurement is normalized intensity autocorrelation function, $g^{(2)}(\tau)$, which is defined as:

$$\mathrm{g}^2(\tau) = \frac{\int_0^\infty I(t)I(t+\tau)\mathrm{d}t}{\int_0^\infty I^2(t)\mathrm{d}t}. \tag{16}$$

The measured intensity correlation function is related to the electric field autocorrelation function, $g^{(1)}(\tau)$, by the Siegert relation [116]:

$$\mathrm{g}^{(2)}(\tau) = 1 + \beta\left|\mathrm{g}^{(1)}(\tau)\right|^2, \tag{17}$$

where β is the coherence factor accounting for the deviation from the ideal correlation. Applying an inverse Laplace transformation on the equation (17), often using a constrained regularization technique (CONTIN), yields the distribution of relaxation times, $A(\tau)$:

$$\mathrm{g}^{(1)}(t) = \int_0^\infty A(\tau)\exp\left(-\frac{t}{\tau}\right)\mathrm{d}\tau\ . \tag{18}$$

For a monodisperse spherical particle, the function, $g^{(1)}(\tau)$, is single-exponential:

$$\mathrm{g}^{(1)}(t) = \exp(-\Gamma t), \tag{19}$$

where Γ is a relaxation rate proportional to the diffusion coefficient, *D*, of the particle. One possibility how to analyze experimentally obtained data is to apply the cumulant fit. The autocorrelation function providing monomodal relaxation time distributions by CONTIN method can be fitted to the cumulant expansion:

$$\ln^{(1)}(t,q) = -\Gamma_1(q)t + \frac{\Gamma_2(q)}{2}t^2 + \cdots + \frac{(-1)^n\Gamma_n(q)}{n!}t^n = \sum_{k=1}^{n}\frac{(-1)^k}{k!}\Gamma_k(q)t^k, \quad (20)$$

where $\Gamma_1(q)$ and $\Gamma_2(q)$, respectively, are the first and the second moment of the distribution function of relaxation rates. The diffusion coefficient of the particles, *D*, can be evaluated by extrapolation of $\Gamma_1(q)/q^2$ using the equation [117]:

$$\frac{\Gamma_1(q)}{q^2} = D(1 + CR_g^2q^2)(1 + k_Dc + \cdots), \quad (21)$$

where *C* is the structural parameter reflecting the shape, polydispersity and internal dynamics of the scattering particles and $k_D = M_wA_2 - k_f - v$ is the hydrodynamic virial coefficient. Here k_f is the friction coefficient and *v* is the molar volume of the scattering particles. From the value of diffusion coefficient extrapolated to the zero angle and zero concentration we can calculate the hydrodynamic radius, R_H, according to the Stokes – Einstein equation [118]:

$$R_H = \frac{k_BT}{6\pi\eta D}, \quad (22)$$

where k_B is the Boltzmann constant, *T* is the temperature and η is the viscosity of the solvent. The $A(\tau)$ distribution can be recalculated to the distributions of apparent hydrodynamic radii, R_H^{app}, using the relationship:

$$R_H^{app} = \frac{k_BTq^2}{6\pi\eta_0}\tau. \quad (23)$$

2.5.2 Small Angle X-ray and Neutron Scattering

Aside from the different mechanisms by which the radiation is scattered, a major difference between light and X-rays and neutrons, is in their wavelengths. X-rays are electromagnetic waves with wavelengths ~0.1 nm, which are scattered by the electrons of atoms. Neutrons have the similar wavelengths as X-rays, but are scattered by the atoms nuclei. The efficiency by which X-rays are scattered depends

on the amount of electrons per illuminated material volume. The average scattered intensity by the sample is just the sum of the average intensity scattered by the individual electrons. The scattering by a single electron is described by a quantity called scattering length, $b_0^X = 2.8x10^{-15}$m. The X-ray scattering length b_j^X of an atom or molecule containing z electrons is then $b_j^X = zb_0^X$. In order to establish contrast in SAXS, studied particles must have different electron density than the surrounding matrix material. The scattering of one particle, can be explained as the interference from every electron inside the particle. Summing up all the wave amplitudes at the detector position and making the square of this sum results in an interference pattern oscillating in a fashion that is responsive to the shape of the particle and is characterized by so-called form factor, $P(q)$. If the sample is dilute (the distances between the particles are large in comparison to the wavelength), then the form factors of all illuminated particles can be summed up. When particle systems are densely packed, the distances relative to each other come into the same order of magnitude as the distance inside the particles and the interference pattern will therefore contain contributions from neighbouring particles as well. This additional interference pattern is called the structure factor, $S(q)$.

The spatial correlations, or structure, in a concentrated system are usually described in terms of the "radial distribution function", $g(R)$, related to the probability of finding the centre of any particle at a distance R from the centre of a given particle. Figure SAXS shows sketches of a typical radial distribution function for a concentrated suspension of strongly interacting colloidal particles and the corresponding structure factor. Since two particles cannot occupy the same space, $g(R)$ is zero for centre-to-centre interparticle separations smaller than the particle diameter. The main peak in $g(R)$ describes the nearest-neighbour shell of particles around any given particle. At large interparticle separations the $g(R)$ function approaches 1 implying that spatial correlations are usually short-ranged. The peak in $S(q)$ can be considered, approximately, to be a "Bragg reflection" from planes of particles separated by distances equal to the mean nearest-neighbour separation.

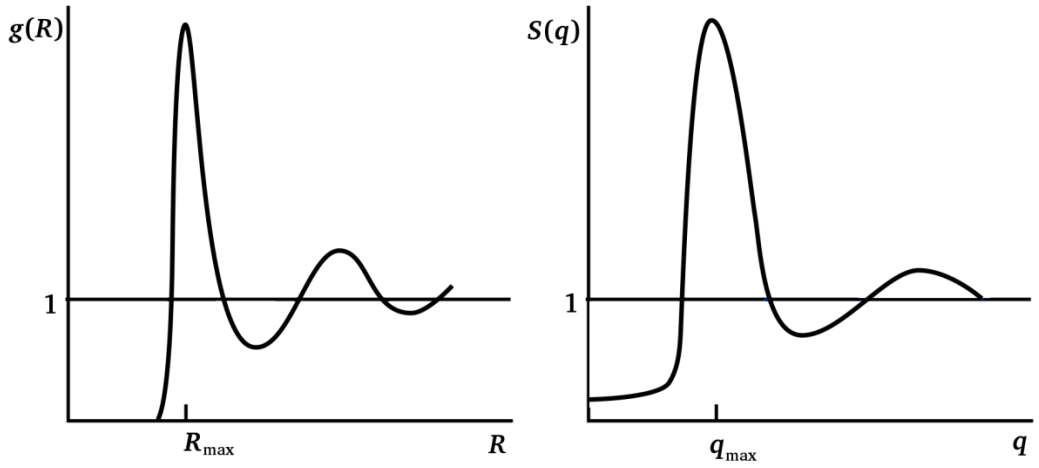

Figure 6: Radial distribution function $g(R)$ and structure factor $S(q)$ for a suspension of strongly interacting colloidal particles [119].

The positions of R_{max} and q_{max} of the main peaks in $g(R)$ and $S(q)$ are related by an approximate "Bragg condition" $q_{max}R_{max} \approx 2\pi$. For this reason it is often said that a scattering experiment, operating at scattering vector, q, measure structure on a spatial scale $2\pi/q$. The peaks in the structure factor become more pronounced, when the particle positions become increasingly ordered. When the domain sizes of ordered particles increase, the system is said to crystallize. The structure factor of a crystalline substance, lattice factor, is a set of narrow and intensive peaks at well-defined angles indicative for the crystal symmetry.

While the X-ray scattering lengths of atoms and thus the intensities of scattering are simply proportional to the atomic number, neutron scattering lengths vary irregularly with the type of the nucleus and can be negative as well as positive, corresponding to a phase shift in the scattering. Furthermore, different isotopes of the same atom can have very different scattering lengths, for example hydrogen nucleus (-3.74×10^{-15} m) and deuterium (6.67×10^{-15} m). Partial deuteration of the components of a sample leads to marked changes in its neutron scattering properties, frequently without seriously affecting its chemical and physical properties. It is possible by this means to highlight different parts of a particle and obtain detailed structural information [119].

In order to achieve required information about the structure from the experimentally obtained scattering data, nonlinear fitting of the scattering curves to various models as well as standard plots are used as the main tools. Standard plots consist in assessing linear behaviours, when plotting functions of the intensity as functions of q, in order to extract characteristic slopes and intercepts. Among the most frequently used plots, belongs the Guinier and the Porod plot.

The Guinier plot involves ln $I(q)$ vs q^2 in order to obtain the radius of gyration, R_g, as a slope of the equation based on the Guinier approximation:

$$\ln I(q) = \ln I(0) - q^2 R_g^2/3. \quad (24)$$

The q-range over which the Guinier approximation is valid, so-called Guinier regime, is limited by the condition $qR_g<1$. Therefore the Guinier regime is much larger for particles with small R_g than for larger ones. Higher q values on the scattering curve contain details regarding to molecular shape.

The Porod region corresponds to a probed range smaller than the scattering objects so that the scattering radiation is probing the local structure. For globular particles of uniform density, the intensity of the scattering falls off by Porod's law:

$$I(q) \propto q^{-4}. \quad (25)$$

Porod's law, like the Guinier approximation, holds only in a portion of the scattering curve. For arbitrary polymers, this region of scattering is typically termed the 'power-law regime', where the dependence of the scattering intensity can be expressed as:

$$I(q) \propto q^{-d}. \quad (26)$$

The Porod plot involving ln $I(q)$ vs ln q, yields information about the so-called fractal dimension, d, of the scattering objects. A Porod slope $d = 1$ is obtained for scattering from rigid rods, while a slope $d = 4$ represents a smooth surface for the scattering particle. Slopes between $d = 3$ and $d = 4$ characterize rough interfaces of surface fractal dimension, D. The scattering from such a rough interface drops as $1/q^{6-D}$. In the case of polymer coils, the Porod slope is related to the excluded volume parameter v as its inverse $d = 1/v$. A slope $d = 2$ is a signature of Gaussian chains in

a dilute environment, a slope $d = 5/3$ is for fully swollen coils and a slope $d = 3$ is for collapsed polymer coils. A slope between $d = 2$ and $d = 3$ is for "mass fractals" such as branched systems, gels or networks.

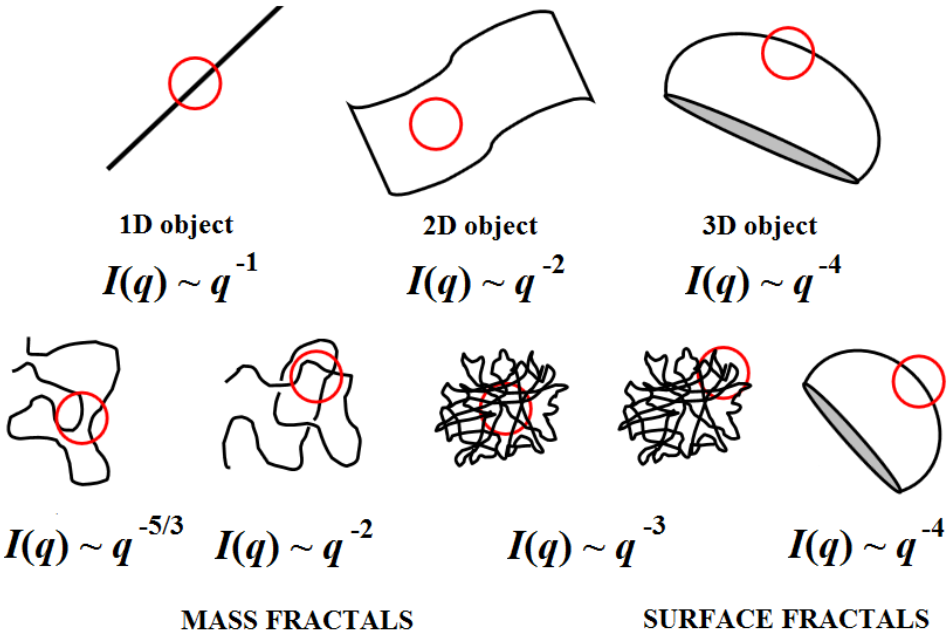

Figure 7: Power-law regime behaviour for objects of different shapes [120].

2.5.3 Electrophoretic light scattering and Zeta potential

Electrophoretic light scattering is the method commonly used to determine the velocity of the particles suspended in a fluid medium under an applied electric field. When a charged particle is suspended into liquid, ions of an opposite charge will be attracted to the surface of the suspended particle. A negatively charged sample attracts positive ions and conversely a positive charged sample attracts negative ions from the liquid. In the fact, the charge on the surface of each particle is counterbalanced by charges of opposite sign (counterions) in the surrounding solution and an electrical double layer exists around each particle. As a result, the solution is neutral as whole and also on a scale somewhat larger than the particles themselves. The liquid layer surrounding the particle consists of two parts. An inner region, called the Stern layer, contains ions situated close to the surface of the

particle and strongly bound to them. Ions that are further away from the surface are less firmly attached and form outer diffusive region, also called a diffuse layer. An electrostatic potential exists between the particle surface and the dispersing liquid which varies according to the distance from the particle surface. The potential near the particle surface is changing very quickly (and linearly) from its value at the surface through the first layer of counterions and then more or less exponentially through the diffuse layer. Within the diffusive layer, there is a notional boundary inside which the ions and particles form a stable entity. When a particle moves in a solution, for example as a result of an applied electric field, ions within the boundary move with it, but any ions beyond the boundary do not travel with the particle, because the electric field pulls the particle in one direction and counterions in the opposite direction. This boundary separating the bound charge from the diffusive charge around the particle is called the surface of hydrodynamic shear or slipping plane. The electrostatic potential on that surface is called the zeta potential and it is the potential which is obtained from electrophoretic measurements of the velocity of the particles under applied electric field. The zeta potential is a very important characteristic giving an indication of the potential stability of the particles within colloidal systems, because it reflects realistically how the particle is seen by other approaching particles, which determines the behavior of the system. If the repulsion between approaching particles is large enough they will bounce away from one another and that will keep the particles in a state of dispersion. If the repulsive force is not strong enough, the particles will come together and may stick into an aggregate. Particularly the zeta potential of the sample will determine whether the particles within a liquid will tend to flocculate (stick together) or not. If the zeta potential of the particles reaches a high negative or positive value then they will tend to repulse each other due to Coulombic interaction and no tendency of flocculation will appear in solution. However, if the particles have low values of zeta potential then there is no force preventing the particles against sticking together and flocculating. A generally accepted limit between stable and unstable suspensions is taken at either +30mV or –30mV. Particles with zeta potential more positive than +30mV or more negative than –30mV are normally considered stable.

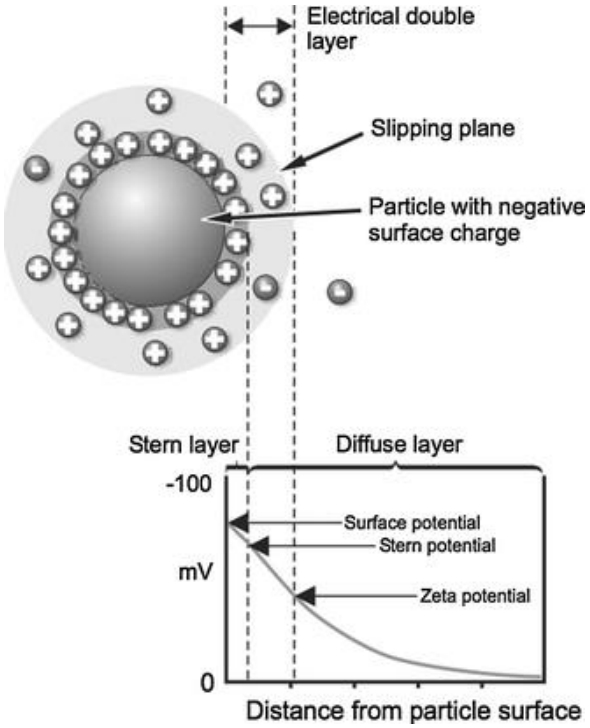

Figure 8: Schematic representation of the double layer that surrounds a particle in aqueous medium. The potential that exists at the slipping plane is known as the ζ-potential. (Taken from Malvern 2007).

The zeta potential of the particle depends strongly on the pH of the solution. Its value on its own without a quoted pH is a virtually meaningless number. If we have some particles with negative zeta potential in solution, adding some alkali to the suspension causes that the particles will tend to acquire a more negative charge. By adding an acid to the solution the zeta potential will increase and a point where the negative charge will be neutralized could be reached. Further addition of acid can cause a capturing of positive charge. The point where the zeta potential passes through zero value is called the isoelectric point and is a very important characteristic in practical terms. Normally it represents the pH conditions, where the colloidal system is the least stable. The knowledge of zeta potential is useful in many industries, for example, in waste water treatment. The flocculation state of waste water is altered by changes in pH or the addition of the chemical flocculants, such as charged polymers, multivalent ions or other highly charged salts.

The measurement of zeta potential is fundamental in the development and maintenance of optimized water treatment protocols [121].

Zeta potential is measured using a combination of two measurement techniques, electrophoresis and laser Doppler velocimetry, sometimes called laser Doppler electrophoresis. Electrophoresis in general is a motion of a charged particle relative to the liquid it is suspended in under the influence of an applied electric field. This method measures the velocity of the particle in an electric field, commonly referred to as its electrophoretic mobility. When an electric field is applied across the solution, charged particles suspended in the solution are attracted towards the electrode of opposite charge. In the same time, viscous forces act on the moving particles in the opposite direction. When equilibrium is reached between these two opposing forces, the particles move with constant velocity, which is dependent on the strength of electric field or voltage gradient, the dielectric constant and viscosity of the medium and the zeta potential of the particle. Based on experimentally obtained data of electrophoretic mobility, the zeta potential of the particles could be calculated by application of the Henry equation:

$$U_{\mathrm{E}} = \frac{2\varepsilon z f(Ka)}{3\eta}, \tag{27}$$

where ζ is zeta potential, UE is electrophoretic mobility, ε is dielectric constant, η is viscosity and *f*(Ka) is Henry´s function. Two limit cases are generally used as a approximations for the *f*(Ka) determination. Electrophoretic determinations of zeta potential are most commonly made in aqueous media and moderate electrolyte concentration. *f*(Ka) in this case is 1.5, and is referred to as the Smoluchowski approximation. The *f*(Ka) value is generally taken 1.0 for zeta potential measurements of small particles in low dielectric constant media. This is referred to as the Hückel approximation, used commonly for non-aqueous measurements. Therefore calculation of zeta potential from the mobility is straightforward for both aqueous and non-aqueous systems [122,123].

The technique used to measure electrophoretic mobility is Laser Doppler Velocimetry (LDV). LDV is a well established technique for the study of fluid flow in a wide variety of situations, from the supersonic flows around turbine blades in jet engines to the velocity of sap rising in a plant stem (ref). For a LDV measurement,

a monochromatic laser beam with a known frequency of light is sent toward the target and the scattered radiation is collected. The scattered light is mixed with the reference beam. This produces a fluctuating intensity signal where the rate of fluctuation is proportional to the speed of the targeted object´s. A digital signal processor is used to extract the characteristic frequencies in the scattered light. The difference between the incident and scattered light frequencies is called the Doppler shift. According to the Doppler effects, the change in frequencies of the scattered radiation is a function of the targeted object's relative velocity [124].

2.5.4 Electron Microscopy

Electron microscopy (EM) is one of the key tools for studying morphology of colloidal nanoparticles. The main advantage of EM stems from the possibility of direct imaging of the size and shape of individual particles. There are two main types of electron microscope – the transmission and the scanning electron microscope. The transmission electron microscope is used to view thin specimens through which electrons can pass generating a projection image. Conventional scanning electron microscopy depends on the emission of secondary electrons and other particles from the surface of a specimen. The interaction of the primary electron beam with the atoms near the surface causes the emission of low energy secondary electrons, high energy back scatter electrons, X-rays and even visible light, which can be collected with a variety of detectors, and their relative number translated to brightness at equivalent points.

Transmission electron microscopy (TEM) is a microscopy technique, similar to a normal light microscopy, in which instead of light, a beam of electrons is transmitted through an ultra-thin film of a sample. A micrograph is formed based on the spatial variations in transmission of the electron beam, due to the interaction of the transmitted electrons with the sample. The contrast comes from the differences in the electron density of the sample. As the maximum resolution that can be obtained with a microscope is limited by the wavelength of the photons that are used to probe the sample, TEM is capable of imaging at a significantly higher resolution then the light microscope due to the small wavelength of electrons (0.02 – 0.05 nm).

The electrons in transmission electron microscope are generated by a either a thermoemission (hot cathode) or autoemission (field emission gun) source, accelerated by application of a high voltage and focused and scanned over the sample by electromagnetic lenses. The whole setup is placed in a high vacuum to avoid collisions of electrons with air molecules. The resulting image is magnified and focused onto an imaging device, such as a fluorescent screen, on a layer of photographic film, or detected by a digital sensor. The imaging of the sample can be performed in several different ways. It is possible to use the bright, the most common, or dark field mode. The contrast of the image in bright mode comes from the absorption and occlusion of the electrons in the sample. Locations with high electron density or larger thickness are displayed on image as a dark stains. In the dark field mode, the scattered electrons are detected so regions with high electron density are brighter than regions with low electron density, which appear as dark spots on the image. In the case of polymer solutions, samples are usually prepared by coating directly onto a carbon-coated TEM grid. This preparation has some disadvantages, because the polymer samples are not in their native environment and it could have some influence on the shape of the polymer chains. In case of soft matter aggregates, which are swollen or filled with solvent, changes of the structure due to deposition on the solid surface and drying can occur. Drying of samples may introduce artifacts like destruction, deformation or aggregation of the imaged particles. There are two types of EM techniques that allow for avoiding the above-mentioned obstacle and imaging solution self-assemblies in situ, cryogenic TEM (cryo-TEM) and environmental SEM (ESEM).

A very powerful method for the investigation of polymer structures in solution is the cryo-TEM, where a thin film of the liquid sample is instantly cooled down by a rapid immersion into liquid ethane. Plunge-freezing into cryogenic liquids is intended to “trap” structures formed and presented in solution, by vitrifying the sample and avoiding crystallization in the solvent. Temperature needs to be controlled during all steps of preparation and measurement to avoid melting and refreezing of the sample.

ESEM microscopy, also known as variable pressure SEM (VP-SEM) microscopy, consists in splitting a SEM microscope into several differentially pumped, aperture-limited sections so that the final chamber with the cooling stage enables wet samples

to be observed. The first commercially available ESEM microscopes contained secondary electrons (SE) and backscattered electrons (BSE) detectors and were successfully applied in numerous studies visualizing bulk wet specimens, including synthetic polymers. Later ESEM microscopes were equipped also with special detectors for transmitted electrons, which made it possible to perform scanning transmission electron microscopy (STEM) in environmental conditions (wet-STEM). Main advantage of wet-STEM imaging consists in the fact that it allows for imaging of nano-sized polymeric particles in the presence of the solvent [125, 126].

2.5.5 Atomic force microscopy

The atomic force microscopy (AFM) is one of the techniques for imaging, measuring and manipulating with the matter at the nanoscale. It is a type of scanning probe microscopy based on scanning of the sample surface by a sharp tip attached at the end of a flexible cantilever to obtain surface topography image thanks to monitoring the tip – surface forces. Forces between the tip and the surface are very weak and it is not possible to measure them directly, so the up and down movement of the cantilever is detected thanks to the mirrored backside which reflects the laser beam into position-sensitive photodetector. When the tip is brought into proximity of a sample surface, forces between the tip and the sample lead to a deflection of the cantilever according to Hooke's law:

$$F = -k_s z, \tag{27}$$

where k_s is the spring constant of the cantilever and z is the vertical cantilever deflection. In general, two types of forces, attractive and repulsive, act at the tip under ambient condition. Depending on the situation, forces that are measured in AFM include mechanical contact force, van der Waals forces, capillary forces, chemical bonding, electrostatic forces, magnetic forces etc. The AFM can be operated in a number of modes, depending on the application. Possible imaging modes are divided into static, also called contact, modes and a variety of dynamic, non-contact or "tapping", modes where the cantilever is oscillated at a given frequency.

In contact mode, the tip is "dragged" across the surface of the sample and the contours of the surface are measured either using the deflection of the cantilever at a constant position. To minimize the applied force, probes with a low spring constant are typically used. Contact mode is almost always done at a depth where the overall force is repulsive, that is, in firm contact with the solid surface. The contact mode works well for hard surfaces, but there is a risk of possible damage of the soft materials, such as polymeric samples, upon the penetration and lateral movement of the tip.

In non-contact AFM, the tip of the cantilever does not contact the sample surface. The tip oscillating with a constant amplitude is scanning the sample in the distance of about 10 nm above the surface. The cantilever is bent towards the sample due to attractive forces. The van der Waals forces, which are strongest from 1 nm to 10 nm above the surface, or any other long-range force that extends above the surface acts to decrease the resonance frequency of the cantilever. This decrease in resonant frequency combined with the feedback loop system maintains a constant oscillation amplitude or frequency by adjusting the average tip-to-sample distance. Measuring the tip-to-sample distance at each point allows the scanning software to construct a topographic image of the sample surface. Non-contact mode does not cause any destruction of the sample or tip, thus this is why it is preferred in measuring soft materials. A disadvantage of this method is that, if there is any adsorbed fluid lying on the surface of a rigid sample, the image from non-contact mode may look quite different from the real surface. An AFM operating in contact mode will penetrate the liquid layer to image the underlying surface, whereas in non-contact mode an AFM will oscillate above the adsorbed fluid layer to image both the liquid and surface.

Tapping mode is most convenient for the study of polymeric materials and other soft matters. It minimizes the direct contact of the cantilever with the surface, by only lightly tapping of the oscillating tip on the surface of the sample during scanning. The tip rapidly moves in and out of the sample surface so that it stays in contact only for a short part of the oscillation period. The frequency and amplitude of the driving signal are kept constant, leading to constant amplitude of the cantilever oscillation as long as there is no drift or interaction with the surface. The interaction of forces acting on the cantilever when the tip comes close to the surface, Van der Waals

forces, dipole-dipole interactions, electrostatic forces, etc. cause decreasing of the amplitude of oscillation. This amplitude is used as the parameter that goes into the electronic equipment that controls the height of the cantilever above the sample. It adjusts the height to maintain a set cantilever oscillation amplitude as the cantilever is scanned over the sample. The oscillation of an AFM tip is defined by the equation:

$$A = A_0 \sin(\omega_0 t + \phi_0), \tag{28}$$

where A_0, ω_0 and ϕ_0 represent the amplitude, frequency and phase angle of free oscillation, respectively. During the scanning process, the equation of the oscillation changes over time:

$$A = A_t \sin(\omega_t t + \phi_t), \tag{29}$$

where A_t, ω_t and ϕ_t are the amplitude, frequency and phase angle of the oscillation at each point in time, respectively. A set-point ratio, r_{sp}, is chosen. The feedback system will maintain the position of the piezo so that the actual oscillation amplitude will be maintained at A_{sp}, as defined by:

$$r_{sp} = \frac{A_{sp}}{A_0}. \tag{30}$$

The actual oscillation amplitude, A_{sp}, is determined by considering the change of the height of the piezo. The topography of the surface is then determined based on this height change, what leads to the height image of the sample. During the oscillation, the frequency and phase angle also change. When operating in tapping mode, the phase of the cantilever's oscillation with respect to the driving signal can be recorded as well. This signal contains information about the energy dissipated by the cantilever in each oscillation cycle. Samples that contain regions of varying stiffness or with different adhesion properties can give a contrast that is not visible in the topographic image.

3 EXPERIMENTAL PART

3.1 STUDIED COPOLYMERS

This thesis is focused on studies of block copolymer complexes with low-molar-mass compounds. The structures of the studied polymers are shown in Figure 9.

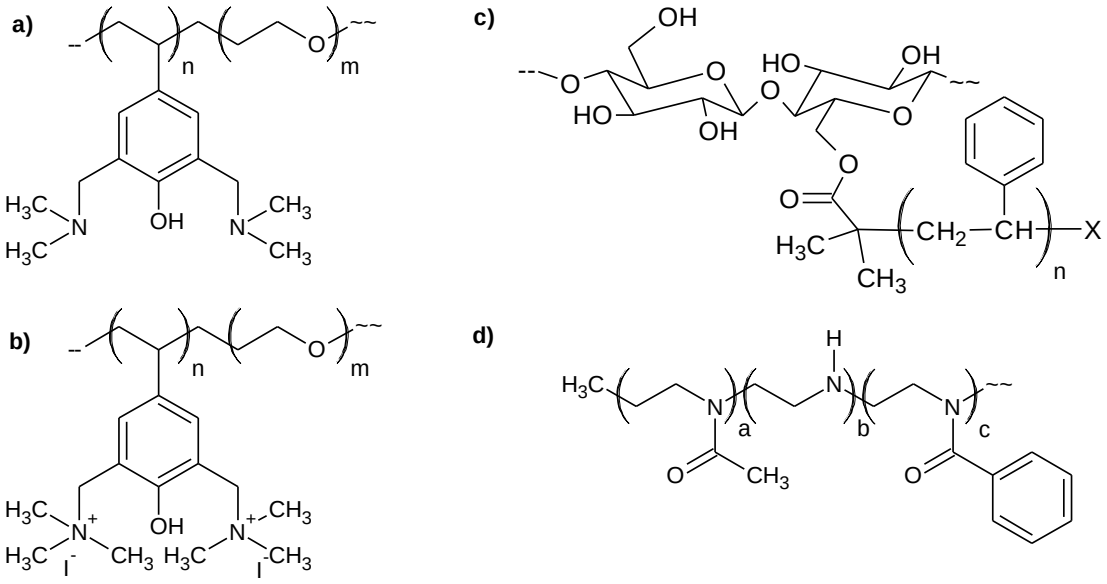

Figure 9: Structures of studied copolymers: a) poly[3,5-bis(dimethylaminomethyl)-4-hydroxystyrene]-*block*-poly(ethylene oxide), (NPHOS-*b*-PEO); b) poly [3,5-bis-(trimethylammoniummethyl)-4-hydroxystyrene iodide]-*block*-poly(ethylene oxide), (QNPHOS-*b*-PEO); c) cellulose-*graft*-polystyrene, Cel-*g*-PS; d) poly[(2-methyl-2-oxazoline)-*grad*-(2-phenyl-2-oxazoline)-*mod*-(ethylene imine)], (HPPhMeOx).

3.1.1 Double hydrophilic block copolymers

Two publications included in this thesis were focused on the study of double hydrophilic block copolymers, DHBCs. The first one deals with the interaction of poly[3,5-bis(dimethylaminomethyl)-4-hydroxystyrene]-*block*-poly(ethylene oxide) (NPHOS-PEO) with oppositely charged surfactant sodium dodecyl sulfate, SDS [127], while the second one was aimed at the interaction between poly[3,5-bis-(trimethylammoniummethyl)-4-hydroxystyrene iodide]-*block*-poly(ethylene oxide) (QNPHOS-PEO) and superparamagnetic iron oxide nanoparticles (SPIONs) [128].

Two different types of DHBCs, consisting of poly(ethylene oxide) (PEO) as the neutral water soluble block and a second polyelectrolyte block based on derivatives of poly(hydroxystyrene) (PHOS), were synthesized in the group of Dr. Stergios Pispas at NHRI, Athens, by the postpolymerization reaction of precursor amphiphilic block copolymers (Figure 9). The synthesis of intermediate PHOS-PEO block copolymer was performed in acetone, by acidic hydrolysis of the precursor poly(tert-butoxystyrene)-*block*-poly(ethylene oxide) (PtBOS-PEO), which was synthesized by sequential anionic polymerization of tert-butoxystyrene and ethylene oxide in vacuum conditions. In order to obtain the required structure of DHBCs, the PHOS block was transformed afterwards by aminomethylation to the NPHOS block, and finally treated with methyl iodide to accomplish the postpolymerization reaction leading to the QNPHOS block. The details on the synthesis and characterization of prepared DHBCs could be found in ref. [129]. The NPHOS block of the NPHOS-PEO copolymer could be considered as a highly charged annealed cationic polyelectrolyte in acidic solution, where NPHOS becomes positively charged due to the protonation of dimethylamino groups and thus the whole copolymer chain is directly soluble in aqueous medium. On the other hand, QNPHOS-PEO was found to be directly soluble in aqueous solutions in the whole range of pH, thanks to quaternized amino groups of the QNPHOS block, which can be considered as a quenched cationic polyelectrolyte with two cationic groups in nearly every monomeric unit.

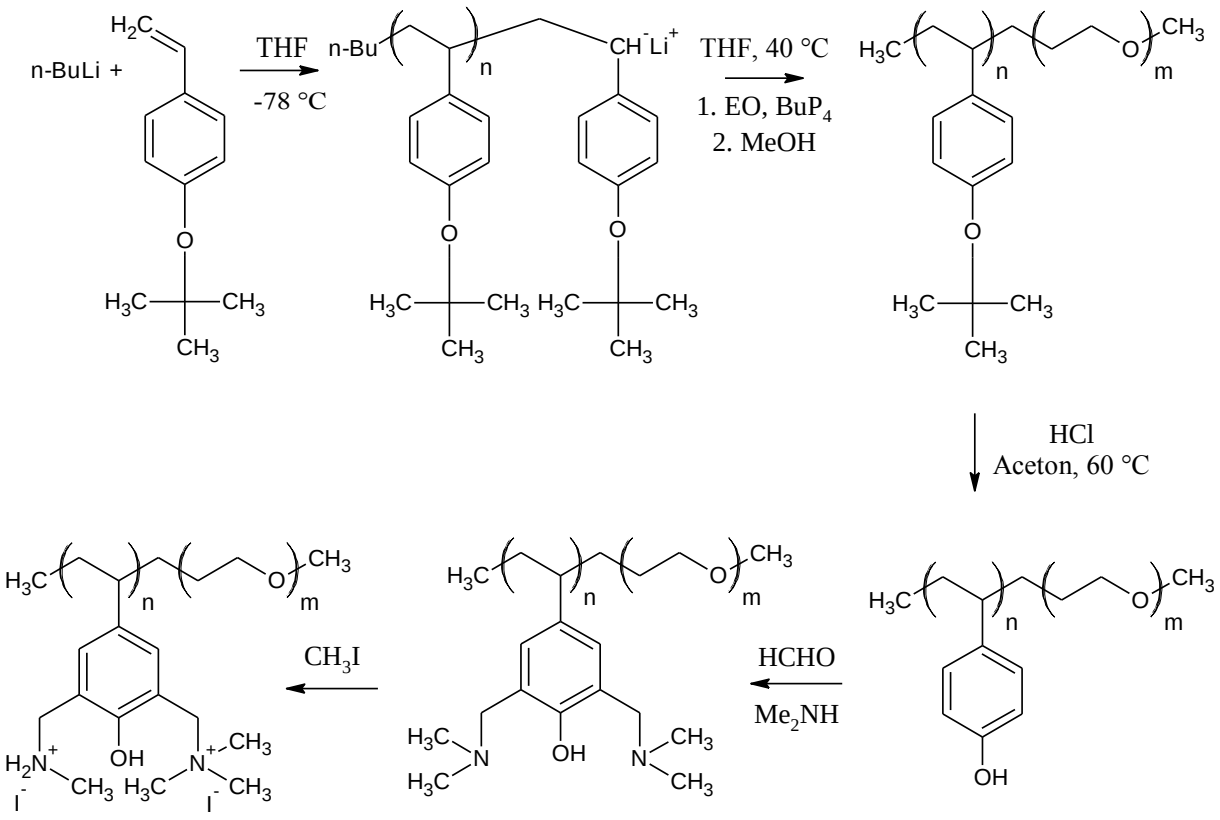

Figure 10: Synthetic scheme for the preparation of NPHOS-PEO and QNPHOS-PEO [129].

3.1.2 Cellulose-based graft copolymers

Cellulose-graft-polystyrene copolymers were prepared by the „grafting-from“ technique by ATRP using the macroiniciator with predetermined number of initiation sites prepared by acylation of microcrystalline cellulose by 2-bromisobutyryl bromide under homogeneous reaction conditions in the N,N-dimethylacetamide/LiCl solvent system (Figure 11). Details on the synthesis and characterization of the samples could be found in ref. [30]. Two samples with the same lengths of the cellulose backbone and polystyrene grafts, differing in the grafting density were used for the study in the publication [130].

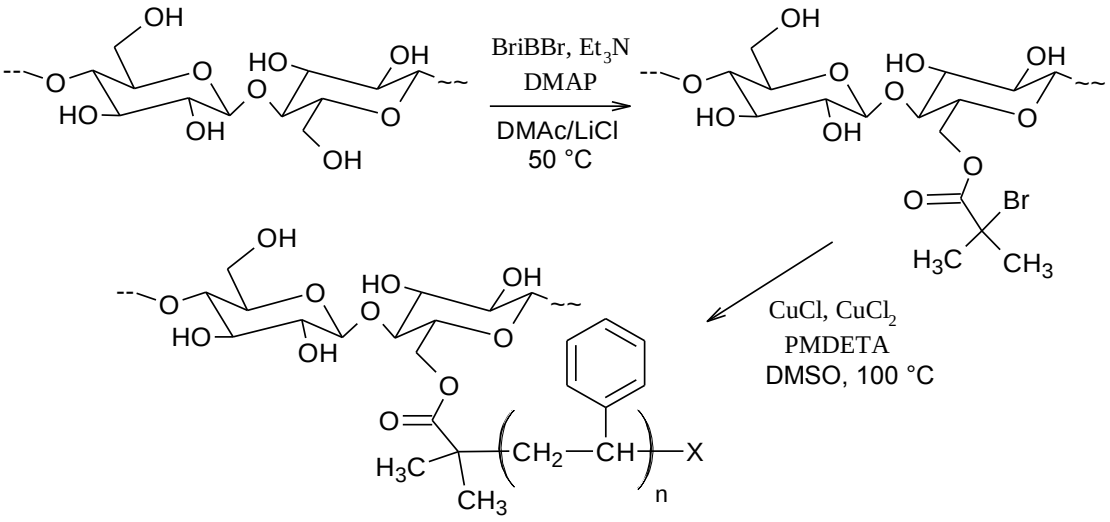

Figure 11: Synthetic scheme for the preparation of Cel-g-PS.

3.1.3 Gradient polyoxazoline-based copolymer

The publication [131] is focused on the study of biocompatible amphiphilic cationic gradient polyelectrolyte poly[(2-methyl-2-oxazoline)-*grad*-(2-phenyl-2-oxazoline)-*mod*-(ethylene imine)] (HPPhMeOx) and the interaction of HPPhMeOx with the anionic surfactant sodium dodecyl sulfate, SDS, in aqueous solutions. HPPhMeOx was prepared by controlled partial hydrolysis of the precursor gradient copolymer poly[(2-methyl-2-oxazoline)-*grad*-(2-phenyl-2-oxazoline)] (PPhMeOx) synthesized by living cationic ring opening polymerization polymerization of 2-oxazolines [33,34] (Figure 12). It was found that the hydrolysis of the PPhMeOx copolymer exhibit a high level of selectivity, resulting in more than 90% hydrolysis of the available methyl side chains while preserving the integrity of 90% of the PhOx segments [34].

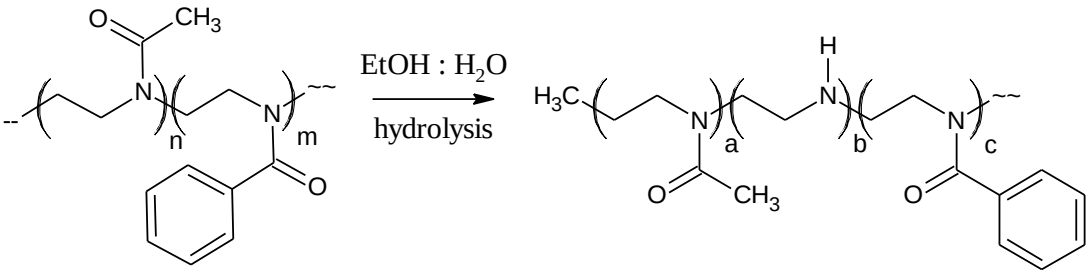

Figure 12: Synthesis of HPPhMeOx from PPhMeOx copolymer.

4 OVERVIEW OF RESULTS

During my PhD studies between the years 2012-2016, four publications dealing with the interactions between copolymers and low-molar-mass compounds were published [127,128,130,131].

4.1 Polyelectrolyte−Surfactant Complexes of Poly[3,5-bis(dimethyl-aminomethyl)-4-hydroxystyrene]-block-poly(ethylene oxide) and Sodium Dodecyl Sulfate: Anomalous Self-Assembly Behavior

The first article, published in 2013 in Langmuir, was aimed on the study of the polyelectrolyte-surfactant complexes of NPHOS-PEO and SDS. The anomalous self-assembly behaviour between double hydrophilic block copolymer and oppositely charged surfactant was discovered by several scattering and microscopic techniques. The study of interactions of this annealed weak polybase was carried out in acidic aqueous solution, 0.1 M HCl, in order to ensure the full ionization of the polyelectrolyte groups. The obtained results showed that the NPHOS-PEO/SDS system behaves differently from other systems of DHBP with oppositely charged surfactant, which often leads to the formation of core-shell nanoparticles with the core of the PE-S complex and the shell formed of the neutral hydrophilic block. It was found that studied system forms water-insoluble complex for compositions close to the zero net charge of the complex, while the excess copolymer or excess surfactant in the system lead to the formation of water-soluble complexes, with the size almost independent of the charge ratio, Z. Based on the light scattering measurements it was confirmed that large spherical aggregates and their clusters are present in the solutions with the concentration of the surfactant below and above the precipitation region. The scattering data indicated that large particles represent only a minority population among the scatterers, and it was assumed that they are formed by secondary aggregation of smaller PE-S particles. Wet-STEM micrographs

confirmed the presence of the clusters of spherical nanoparticles with the broad size distribution. Based on the zeta potential measurements it was found that the aggregates in the solution are stabilized mostly electrostatically. The aggregates formed in the Z range from 0.6 to 1.5, in which the zeta potential was law, precipitated from the solution, while aggregates above the precipitation region overcharged significantly. The fact that the zeta potential of the aggregates formed below the precipitation region were not sufficiently high for the pure electrostatic stabilization, suggested that hydrophilic PEO blocks must play some role in keeping the particles soluble in the solution, but it is not sufficient for aggregates with the charge close to zero. It was suggested that inability of copolymer to undergo core-shell transition could be caused by conformational rigidity and high charge density of NPHOS chains. Although the NPHOS-PEO/SDS system does not form core-shell particles, it was proved by SAXS measurements that the aggregates contain domains of closely packed surfactant micelles with two types of local arrangement corresponding to the micelles bound to NPHOS blocks and PEO blocks separately.

4.2 Structure of polymeric nanoparticles in surfactant-stabilized aqueous dispersions of high-molar-mass hydrophobic graft copolymers

The second article published in 2014 in the journal Colloids and Surfaces A: Physicochemical and Engineering Aspects was aimed on the study of polymeric nanoparticles of high-molar-mass hydrophobic graft copolymers in organic solvent and in water after stabilization by anionic surfactant.

Aqueous dispersions of two types of cellulose-graft-polystyrene (Cel-*g*-PS) copolymers, varying in the grafting density, were prepared by nanoprecipitation from the water-miscible organic solvent, 1,4-dioxane, using SDS as a stabilizer. Prior to the preparation of nanoprecipitated particles, both copolymers were studied at several concentrations by SLS and DLS in order to determine their molar mass, size and interaction parameters. It was found that the molar masses of both samples were higher than those calculated from the grafting density and molar masses of the grafts and backbones, what can be explained by a partial intermolecular recombination of growing polystyrene chains, resulting in covalent bonding between different

copolymer molecules. Afterwards, the nanoprecipitation of the copolymer into the aqueous solution of the surfactant was performed and the dependence of the size of the nanoprecipitated particles on the initial concentration of copolymer in organic solvent and the concentration of the surfactant in aqueous media was investigated. Results of scattering measurements (SLS, SAXS) and TEM showed that the used preparation protocol led to the formation of polydisperse, highly irregularly shaped and structurally heterogeneous aggregates of individual collapsed macromolecules containing entrapped surfactant micelles. It was shown that the size of the aggregates formed by nanoprecipitation could be tuned by the initial polymer concentration in the organic solvent. On the other hand, there was found only a weak dependence of the size of nanoparticles on the surfactant concentration in aqueous media. The slight increase in the hydrodynamic radius with the increase of SDS concentration was observed, most likely thanks to the screening of electrostatic repulsion with increasing the concentration of ionic surfactant and thus increasing of the ionic strength of the solution. Similarly to the case of NPHOS-PEO/SDS system, aggregates of the Cel-*g*-PS/SDS are electrostatically stabilized by SDS molecules, which keep them negatively charged. SAXS measurements in the high-*q* region indicate that the particles contain densely packed SDS micelles, which do not escape from the interior of the kinetically frozen particles even during the dialyses against pure water.

4.3 Aggregation of superparamagnetic iron oxide nanoparticles in dilute aqueous dispersions: Effect of coating by double-hydrophilic block polyelectrolyte

The study published in 2015 in the journal Colloids and Surfaces A: Physicochemical and Engineering Aspects was aimed on the investigation of aggregation behaviour of the oleate-stabilized magnetic nanoparticles and their coating with double hydrophilic block copolymer, QNPHOS-PEO, in order to form additional layer protecting them against aggregation in diluted aqueous solutions. Aggregation of SPION in dilute aqueous dispersions and their protection via coating by DHBC was studied by dynamic light scattering, small-angle light scattering and

microscopic techniques including atomic force microscopy and transmission electron microscopy. The binding of the copolymer to the magnetic nanoparticles was observed by the increasing of the zeta potential as well as of apparent hydrodynamic radius. Both values were increasing depending on the ratio between polymer concentration and concentration of oleate coated magnetic nanoparticles. It was proved that stabilization of the nanoparticles is provided by the PEO blocks of the copolymer, because the saturation point of the SPIONs by polymer corresponded to very low value of the zeta potential, only about 5 mV, which is not sufficient for electrostatic stabilization. The formation of smaller aggregates was confirmed also by AFM and TEM micrographs.

Small angle light scattering data revealed that oleate-SPIONs aggregate in dilute aqueous solution into large compact aggregates with the size about 2 microns and mass fractal dimension around 2.4, characteristic for reaction limited cluster-cluster aggregation. DLS measurements showed that the aggregates exhibit internal dynamics with the relaxation mode with $\tau \sim q^{-3}$, typical form systems undergoing structural rearrangements such as gels. Coating of the oleate-SPIONs by QNPHOS-PEO affects their behaviour in dilute solutions and partially protects them against aggregation. In the case of QNPHOS-PEO/oleate-SPIONs formed aggregates have only around 100 nm.

4.4 Self- and co-assembly of amphiphilic gradient polyelectrolyte in aqueous solution: Interaction with oppositely charged ionic surfactant

The last article dealing with the interactions of SDS, as oppositely charged surfactant, with amphiphilic cationic gradient polyelectrolyte was published in 2015 in European Polymer Journal. The goal of this article was to describe the association behaviour of the biocompatible, protein mimicking amphiphilic gradient PE HPPhMeOx with the anionic surfactant, SDS, in acidic aqueous solution, because the interaction of the hydrophobic-hydrophilic gradient polyelectrolyte with oppositely charged surfactant has not been studied before. Dynamic light scattering measurement of the free copolymer aqueous solution indicated that HPPhMeOx

is not molecularly soluble in water and exists in the form of large, weakly scattering aggregates with the hydrodynamic radius of about 500 nm. Based on evaluation of SANS curves, which exhibit the distinct Guinier regime with the gyration radius of 10 nm, it could be assumed that these large aggregates are formed by a network of physically crosslinked hydrophobic domains of PPhOx with the mean radius of 10 nm. Addition of the surfactant to the HPPhMeOx solution causes the disruption of the network, what is evident from the significant decrease of hydrodynamic radius. After an addition of the surfactant to the acidic solution of the HPPhMeOx the formation of the compact aggregates of HPPhMeOx/SDS complexes accompanied by increasing of turbidity appears. Results from the electrophoretic light scattering show that the stability of the formed complexes depends on the charge ratio, Z, defined as the molar ratio of the amount of dodecyl sulfate anions to the amount of ethylene imine units. The aggregates with the Z value around 0.4, having low electrophoretic mobility, because of the low values of the ζ potential, are very unstable and precipitate within a few days after preparation. This observation indicates that the formed aggregates are stabilized mainly electrostatically. The SANS measurements of the HPPhMeOx/SDS dispersions with various Z values, confirm the presence of compact domains below and above the precipitation region. The R_g dependence of these domains passes the maximum at Z = 0.22, which indicates different mechanism of the interaction of SDS with copolymer at low and high concentrations of SDS. Below the critical aggregation concentration (cac), DS single ions are bound preferentially into hydrophobic domains formed by PhOx units and cause considerable growth of their size. After the reaching of cac, ($Z > 0.6$), the hydrophobic domains are disrupted and the majority of the HPPhMeOx chains are bound into the HPPhMeOx/SDS complexes, which contain densely packed surfactant micelles. The proof of the existence of highly ordered structure of SDS micelles is supported by the correlation peak in the high-q region of the SANS curves. The Bragg length corresponding to the peak position, $\lambda = 2\pi/q_{max} = 3.6$ nm, represents the distance between the neighbouring packed SDS micelles.

The ability of HPPhMeOx chains to form both hydrophobic domains and the PE-S complexes indicates the amphiphilic character of the gradient polyelectrolyte chain.

5 SUMMARY

This thesis is based on studies of self-assembly and co-assembly behaviour of several types of copolymers with low-molar-mass compounds that I conducted at the Department of Physical and Macromolecular Chemistry at the Charles University, Prague under the leading of my supervisor, doc. RNDr. Miroslav Štěpánek PhD, between the years 2012 and 2016. My work contributed to publishing four articles, in three of which I am the first author and in the last case the second author.

Three of the four articles dealt with interactions of various types of copolymers with sodium dodecyl sulfate (SDS) as a representative of ionic surfactant and formation of co-assembled nanoparticles. The studies involved copolymers with polycationic blocks which produced electrostatically stabilized complexes with SDS (NPHOS-*b*-PEO, HPPhMeOx) as well as neutral copolymers (cellulose-*graft*-polystyrene) in which the complexation was based solely on hydrophobic interactions. The studies showed that in both cases the co-assembly contained densely packed SDS micelles, even though the electrostatic interaction lead to more ordered packing of SDS micelles in the co-assembly. The study of the NPHOS-*b*-PEO/SDS system demonstrated that the formation of core-shell particles with the well-segregated neutral shell and the core of the polyelectrolyte-surfactant complex is not the only possible scenario for co-assembly of double-hydrophilic diblock polyelectrolytes with oppositely charged surfactants, unlike to what was shown many times earlier in the literature.

The fourth article aimed at interactions of block copolymers with superparamagnetic iron oxide nanoparticles (SPION)s, showing the enhancement of the long term stability of negatively charged SPIONs in dilute aqueous dispersions by coating with QNPHOS-*b*-PEO. The small-angle light scattering study of the SPIONs and QNPHOS-*b*-PEO/SPIONs dispersions revealed changes in the structure of the large aggregates (the lengthscale of μm to tens of μm) of SPIONs in aqueous media induced by the coating.

References

[1] Hamley, I. *Physics of Block Copolymers*; Oxford University Press, Oxford, **1998**.

[2] Riess, G. *Prog. Polym. Sci.* **2003**, *28*, 1107-1170.

[3] Hadjichristidis, N.; Pispas, S.; Floudas, G.A. *Block Copolymers. Synthetic Strategies, Physical Properties and Applications;* J. Wiley, Hoboken, **2003**.

[4] Khandpur, A.K.; Foerster, S.; Bates, F.S.; Hamley, I.; Ryan, A.J.; Bras, W.; Almdal, K.; Mortensen, K. *Macromolecules* **1995**, 28, 8796-8806.

[5] Wanka, G.; Hoffmann, H.; Ulbricht, W. *Macromolecules* **1994**, 27, 4145-4159.

[6] Hernández, J.R.; Chécot, F.; Gnanou, Y.; Lecommandoux, S. *Prog. Polym. Sci.* **2005**, 30, 691–724.

[7] Zhang, L.; Eisenberg, A. *J. Am. Chem. Soc.* **1996**, 118, 3168-3181.

[8] Zhang, W.; Shi, L.; An, Y.; Gao, L.; Wu, K.; Ma, R.; Zhang, B. *Macromol. Chem. Phys.* **2004**, 205, 2017-2025.

[9] Matsuda, T.; Annaka, M. *Langmuir* **2008**, 24, 5707-5713.

[10] Cai, S.; Vijayan, K.; Cheng, K.; Lima, E.M.; Discher, D.D. *Pharm. Res.***2007**, 24, 2099-2109.

[11] Kataoka, K.; Harada, A.; Nagasaki, Y. *Adv Drug Deliv Rev.* **2001**, 47, 113-131.

[12] Ganta, S.; Devalapally, H.; Shahiwala, A.; Amiji, M. *Journal of Controlled Release* **2008**, 126, 187–204.

[13] Park, M.; Harrison, C.; Chaikin, P.M.; Register, R.A.; Adamson, D.H. *Science* **1997**, 276, 1401-1404.

[14] Bolognesi, A.; Botta, C.; Thin, S.Y. *Solid Films* **2005**, 492, 307–312.

[15] Bronstein, L.M.; Sidorov, S.N.; Gourkova, A.Y.; Valetsky, P.M.; Hartmann, J.; Breulmann, M.; Cölfen, H.; Antonietti, M. *Inorganica Chimica Acta* **1998**, 280, 348–354.

[16] Berret, J.F.; Sehgal, A.; Morvan, M.; Sandre, O.; Vacher, A.; Airiau, M. J. *Colloid Interface Sci.* **2006**, 303, 315–318.

[17] Frka-Petesic, B.; Fresnais, J.; Berret, J.F.; Dupuis, V.; Perzynski, R.; Sandre, O. *J. Magn. Magn. Mater.* **2009**, 321, 667–670.

[18] Pichot, C. *Reactive nanocolloids for nanotechnologies and microsystems, Colloidal Nanoparticles in Biotechnology*, Wiley, **2008**, 1–30.

[19] Sanchez-Gaytan, B.L.; Li, S.; Kamps, A.C.; Hickey, R.J.; Clarke, N.; Fryd, M.; Wayland, B.B.; Park, S.J. *The Journal of Physical Chemistry C* **2011**, 115, 7836-7842.

[20] Gustafsson, J.; Ljusberg-Wahren, H.; Almgren, M.; Larsson, K. *Langmuir* **1997**, 13, 6964-6971.

[21] Lemarchand, C.; Couvreur, P.; Vauthier, C.; Costantini, D.; Gref, R. *International Journal of Pharmaceutics* **2003**, 254, 77–82.

[22] Amalvy, J.I.; Unali, G.F.; Li, Y.; Granger-Bevan, S.; Armes, S.P.; Binks, B.P.; Rodrigues, J.A.; Whitby, C.P. *Langmuir* **2004**, 20, 4345-4354.

[23] Lee, J.C.-M.; Bermudez, H.; Discher, B.M.; Sheehan, M.A.; Won, Y.-Y.; Bates, F.S.; Discher, D.E. *Biotechnology and Bioengineering* **2001**, 73, 135-145.

[24] Bermudez, H.; Brannan, A.K.; Hammer, D.A.; Bates, F.S.; Discher, D.E. *Macromolecules* **2002**, 35, 8203-8208.

[25] Bermudez, H.; Hammer, D.A.; Discher, D.E.; *Langmuir* **2004**, 20, 540-543.

[26] Forster, S.; Abetz, V.; Muller, A.H.E. *Adv Polym Sci* **2004**, 166, 173-210.

[27] Colfen, H. *Macromolecular Rapid Communications* **2001**, 22, 219-252.

[28] Bütün, V.; Liu, S.; Weaver, J.V.M.; Bories-Azeau, X.; Cai, Y.; Armes, S.P. *Reactive and Functional Polymers* **2006**, 66, 157–165.
[29] Bütün, V.; Billingham, N.C.; Armes, S.P. *J. Am. Chem. Soc.* **1998**, 120, 11818-11819.
[30] Raus, V.; Stepanek, M.; Uchman, M.; Slouf, M.; Latalova, P.; Cadovam, E.; Netopilík, M.; Krız J.; Dybal, J.; Vlcek, P. *J. Polym. Sci. A Polym. Chem*. **2011**, 49, 4353–4367.
[31] Hoogenboom, R.; Lambermont-Thijs, H.M.L.; Jochems, M.H.J.C.; Hoeppener, S.; Guerlain, C.; Fustin, C.A.; Gohy, J.F.; Schubert, U.S. *Soft Matter* **2009**, 5, 3590–3592.
[32] Glassner, M.; Lava, K.; Rosa, V.R.; Hoogenboom, R. *J. Polym. Sci. A Polym. Chem*. **2014**, 52, 3118–3122.
[33] Vlassi, E.; Pispas, S. *Macromolecular Chemistry and Physics* **2015**, 216, 873-883.
[34] Kuringen, H.P.C.; de la Rosa, V.R.; Fijten, M.W. M.; et al. *Macromol. Rapid Commun.* **2012**, 33, 827-832.
[35] Ge, Z.; Xie, D.; Chen, D.; Jiang, X.; Zhang, Y.; Liu, H.; Liu, S. *Macromolecules* **2007**, 40, 3538-3546.
[36] Zhang, W.; Shi, L.; Wu, K.; An, Y. *Macromolecules* **2005**, 38, 5743-5747.
[37] Li, G.; Song, S.; Guo, L.; Ma, S. *J. Polym. Sci. A Polym. Chem*. **2008**, 46, 5028–5035.
[38] Boudier, A.; Aubert-Pouëssel, A.; Gérardin, C.; Devoisselle, J.-M.; Bégu, S. *International Journal of Pharmaceutics* **2009**, 379, 212–217.
[39] Butun, V.; Armes, S.P.; Billingham, N.C. *Polymer* **2001**, 42, 5993-6008.
[40] Brackman, J.C.; Engberts, J.B.F.N. *Chem. Soc. Rev.* **1993**, 22, 85-92.
[41] Saito, S. *Kolloid Zeitschrift* **1957**, *1*54, 19.
[42] Cabane, B. *The Journal of Physical Chemistry* **1977**, 81, 1639-1645.
[43] Nagarajan, R. *Colloids and Surfaces* **1985**, 13, l-17.
[44] Cabane, B. *Colloids and Surfaces* **1085**, 13, 19-33.
[45] Mészáros, R.; Thompson, L.; Bos, M.; Varga, I.; Gilányi, T. *Langmuir* **2003**, 19, 609-615.
[46] Jain, N.; Trabelsi, S.; Guillot, S.; McLoughlin, D.; Langevin, D.; Letellier, P.; Turmine, M. *Langmuir* **2004**, 20, 8496-8503.
[47] Langevin, D. *Advances in Colloid and Interface Science* **2009**, 147–148, 170–177.
[48] Hansson, P. *Langmuir* **2001**, 17, 4167-4180.
[49] Diamant, H.; Andelman, D. *Macromolecules* **2000**, 33, 8050-8061.
[50] Hansson, P. *Current Opinion in Colloid & Interface Science* **2006**, 11, 351–362.
[51] Lindman, B.; Antunes, F.; Aidarova, S.; Miguel, M.; Nylander, T. *Colloid Journal* **2014**, 76, 585–594.
[52] Hansson, P.; Lindman, B. *Current Opinion in Colloid & Interface Science* **1996**, 1, 604-613.
[53] Burrows, H.D.; Valente, A.J.M.; Costa, T.; Stewart, B.; Tapia, M.J.; Scherf, U. *Journal of Molecular Liquids* **2015**, 210, 82–99.
[54] Percebom, A.M.; Barbosa, L.R.S.; Itri, R.; Loh, W. *Langmuir* **2014**, 30, 11493-11503.
[55] Wallin, T.; Linse, P. *Langmuir* **1996**, 12, 305-314.
[56] Antonietti, M.; Conrad, J.; Thuenemann, A. *Macromolecules* **1994**, 27, 6007-6011.
[57] Wang, C; Tam, K.C. *Journal of Physical Chemistry B* **2004**, 108, 8976-8982.
[58] Claesson, P.M.; Bergström, M.; Dedinaite, A.; Kjellin, M.; Legrand, J.F.; Grillo, I. *Journal of Physical Chemistry B* **2000**, 104, 11689-11694.
[59] Yoshida, K.; Dubin, P.L. *Colloids and Surfaces A* **1999**, 147, 161–167.
[60] Anghel, D.F.; Saito, S.; Băran, A.; Iovescu, A. *Langmuir* **1998**, 14, 5342-5346.
[61] Anghel, D.F.; Saito, S.; Băran, A.; Iovescu, A.; Corniţescu, M. *Colloid. Polym. Sci.* **2007**, 285, 771-779.
[62] Park, S.Y.; Bruinsma, R.F.; Gelbart, W.M. *Europhys Lett* **1999**, 46, 454-460.
[63] Berret, J.F. *Journal of Chemical Physics* **2005**, 123, 164703.
[64] Rumyantsev, A.M.; Santer, S.; Kramarenko, E. *Macromolecules* **2014**, 47, 5388-5399.
[65] Jonsson, M; Linse, P. *Journal of Chemical Physics* **2001**, 115, 3406-3418.
[66] Santos, S.; Gustavsson, C.; Gudmundsson, C.; Linse, P.; Piculell, L. *Langmuir* **2011**, 27, 592-603.

[67] Pojják, K.; Mészáros, R. *Langmuir* **2011**, 27, 14797-14806.
[68] Thalberg, K.; Lindman, B.; Karlstroem, G. *The Journal of Physical Chemistry* **1990**, 94, 4289-4295.
[69] Bronich, T.K.; Kabanov, A.V.; Kabanov, V.A.; Yu, K.; Eisenberg, A. *Macromolecules* **1997**, 30, 3519-3525.
[70] Bronich, T.K.; Cherry, T.; Vinogradov, S.V.; Eisenberg, A.; Kabanov, V.A.; Kabanov, A.V. *Langmuir* **1998**, 14 , 6101-6106.
[71] Kabanov, A.V.; Bronich, T.K.; Kabanov, A.V.; Yu, K.; Eisenberg, A. *J. Am. Chem. Soc.* **1998**, 120, 9941-9942.
[72] Wang, Y.; Han, P.; Xu, H.; Wang, Z.; Zhang, X.; Kabanov, A.V. *Langmuir* **2010**, 26, 709-715.
[73] Berret, J.F.; Herve, P.; Aguerre-Chariol, O.; Oberdisse, J. *J. Phys. Chem. B* **2003**, 107, 8111-8118.
[74] Berret, J.F.; Oberdisse, J. *J. Physica B Cond. Matter* **2004**, 350, 204-206.
[75] Berret, J.F.; Vigolo, B.; Eng, R.; Herev, P.; Grillo, I.; Yang, I. *Macromolecules* **2004**, 37, 4922-4930.
[76] Berret, J.F.; Cristobal, G.; Hervé, P.; Oberdisse, J.; Grillo, I. *The European Physical Journal* **2002**, 9, 301-311.
[77] Štěpánek, M.; Matějíček, P.; Procházka, K.; Filippov, S.K.; Angelov, B.; Šlouf, M.; Mountrichas, G.; Pispas, S. *Langmuir* **2011**, 27, 5275-5281.
[78] Gupta, A.K.; Gupta, M. *Biomaterials* **2005**, 26, 3995–4021.
[79] Moeser, G.D.; Roach, K.A.; Green, W.H.; Hatton, T.A. *AIChE Journa*l **2004**, 50, 2835-2848.
[80] Sondjaja, R.; Hatton, T.A.; Tam, M.K.C. *J. Magn. Magn. Mater.* **2009**, 321, 2393–2397.
[81] Zheng, W.; Gao, F.; Gu, H. *J. Magn. Magn. Mater.* **2005**, 288, 403–410.
[82] Euliss, L.E.; Grancharov, S.G.; O'Brien, S.; Deming, T.J.; Stucky, G.D.; Murray, C.B.; Held, G.A. *Nano Letters* **2003**, 3, 1489-1493.
[83] Jordan, A.; Scholz, R.; Wust, P.; Fähling, H.; Felix, R. *J. Magn. Magn. Mater.* **1999**, 201, 413-419.
[84] Safarik, I.; Safarikova, M. *Chemical Papers*, 63, 497–505.
[85] Laurent, S.; Forge, D.; Port, M.; Roch, A.; Robic, C.; Elst, L.V.; Muller, R.N. *Chemical Reviews* **2008**, 108, 2064-2110.
[86] Jolivet, J.P.; Chaneac, C.; Tronc, E. *Chem. Commun.* **2004**, 5, 481–487.
[87] Wan, S.R.; Huang, J.S.; Yan, H.S.; Liu, K.L. J. *Mater. Chem*. **2006**, 16, 298–303.
[88] Liu, C.H.; Zhou, Z.D.; Yu, X.; Lv, B.Q.,; Mao, J.F.; Xiao, D. *Inorganic Materials* **2008**, 44, 291-295.
[89] Zheng, B.; Zhang, M.; Xiao, D.; Jin, Y.; Choi, M.M.F. *Inorganic Materials* **2010**, 46, 1106-1111.
[90] Haque, K.E. Int. J. *Miner. Process.* **1999**, 57, 1–24.
[91] Ge, S.; Shi, X.Y.; Sun, K.; et al. *J. Phys. Chem. C* **2009**, 113, 13593–13599.
[92] Fathi, M.; Entezami, A.A. *Surf. Interface Anal.* **2014**, 46, 145–151.
[93] Basuki, J.S.; Jacquemin, A.; Esser, L.; Li, Y.; Boyer, C.; Davis, T.P. *Polym. Chem*. **2014**, 5, 2611-2620.
[94] Choia, J.-W.; Lee, H.; Song, Y.; Sohn, D. *J. Colloid Interface Sci.* **2015**, 443, 2015, 8–12.
[95] Berger, P.; Adelman, N.B.; Beckman, K.J.; Campbell, D.J.; Ellis, A.B.; Lisensky, G.C. *Journal of Chemical Education*. **1999**, 76, 943-948.
[96] Lecommandoux, S.; Sandre, O.; Checot, F.; Rodriguez-Hernandez, J.; Perzynski, R. *Adv. Mater.* **2005**, 17, 712-718.
[97] Hickey, R.J.; Haynes, A.S.; Kikkawa, J.M.; Park, S.-J. *J. Am. Chem. Soc.* **2011**, 133, 1517-1525.
[98] Filippousi, M.; Papadimitriou, S.A.; Bikiarib, D.N.; Pavlidou, E.; Angelakeris, M.; Zamboulis, D.; Tian, H.; Tendeloo, G.V. *International Journal of Pharmaceutics* **2013**, 448, 221–230.

[99] Hickey, R.J.; Sanchez-Gaytan, B.L.; Cui, W.; Composto, R.J.; Fryd, M.; Wayland, B.B.; Park, S.J. *Small* **2010**, 6, 48–51.
[100] Kamps, A.C.; Sanchez-Gaytan, B.L.; Hickey, R.J.; Clarke, N.; Fryd, M.; Park, S.J. *Langmuir* **2010**, 26, 14345-14350.
[101] Berret, J.F.; Schonbeck, N.; Gazeau, F.; Kharrat, D.E.; Sandre, O.; Vacher, A.; Airiau, M. *J. Am. Chem. Soc.* **2006**, 128, 1755-1761.
[102] Xu, Y.; Yuan, J.; Fang, B.; Drechsler, M.; Müllner, M.; Bolisetty, S.; Ballauff, M.; Müller, A.H.E. *Adv. Funct. Mater.* **2010**, 20, 4182–4189.
[103] Forrest, S.R.; Witten, T.A. *J Phys A Math Gen* **1979**, 12, L109.
[104] Witten, T.A.; Sander, L.M. *Phys. Rev. Lett.* **1981**, 47, 1400.
[105] Meakin, P. *J. Colloid Interface Sci.* **1984**, 102, 491-504.
[106] Wua, H.; Lattuadab, M.; Morbidellia, M. *Advances in Colloid and Interface Science* **2013**, 195–196, 41–49.
[107] Mandelbrot, B. B. *The Fractal Geometry of Nature*; Freeman: San Francisco, CA, **1982**.
[108] Burns, J.L.; Yan, Y.; Jameson, G.J.; Biggs, S. *Langmuir* **1997**, 13, 6413-6420.
[109] González, A.E. *Phys. Rev. Lett.* **1993**, 71, 2248.
[110] Schaefer, D.W.; Martin, J.E.; Wiltzius, P.; Cannell, D.S. *Phys. Rev. Lett.* **1984**, 52, 2371-2374.
[111] Kima, T.; Leea, C.-H.; Joob, S.-W.; Leea, K. *J. Colloid Interface Sci.* **2008**, 318, 238–243.
[112] Bushell, G.; Amal, R. *J. Colloid Interface Sci.* **2000**, 221, 186-194.
[113] Strutt, J. *Philosophical Magazine* **1871**, 41, 107-120, 274-279.
[114] Wyatt, P.J. *Analytica Chimica Acta* **1993**, 272, 1-40.
[115] Debye, P. *The Journal of Physical and Colloid Chemistry* **1947**, 51, 18-32.
[116] Siegert, A.J.F., *MIT Rad. Lab.* **1943**, 465.
[117] Schärtl, W. *Light Scattering from Polymer Solutions and Nanoparticle Dispersions*; Springer, Berlin, **2007**.
[118] Brown, W. *Light Scattering: Principles and Developement*; Calendron Press, Oxford, **1996**.
[119] Lindner P.; Zemb,T. *Neutrons, X-Rays and Light: Scattering methods applied to soft condensed matter;* Elsevier North-Holland, **2002**.
[120] Hammouda, B. *A Distance Learning Course of Small-Angle Neutron Scatterin,* chapter 22 https://www.ncnr.nist.gov/staff/hammouda/distance_learning/chapter_22.pdf
[121] López-Maldonado, E.A.; Oropeza-Guzmana, M.T.; Jurado-Baizavala, J.L.; Ochoa-Terán, A. *Journal of Hazardous Materials* **2014**, 279, 1-10.
[122] Sarit K.D.; Choi, S.U.; Yu, W.; Pradeep, T. *Nanofluids: Science and Technology, Technology & Engineerin* **2007**, 57.
[123] Swan, J.W.; Furst, E.M. *J. Colloid Interface Sci.* **2012**, 388, 92–94.
[124] Zetasizer nano series user manual, Malvern Instruments Ltd. **2009.**
[125] Bogner,A.; Thollet, G.; Basset, D.; Jouneau, P.-H.; Gauthier, C. *Ultramicroscopy* **2005**, 104, 290–301.
[126] Šlouf, M.; Lapčíková, M.; Štěpánek, M. *European Polymer Journal* **2011**, 47, 1273–1278.
[127] Hajduová, J.; Procházka, K.; Šlouf, M.; Angelov, B.; Mountrichas, G.; Pispas, S.; Štěpánek, M. *Langmuir* **2013**, 29, 5443-5449.
[128] Hajduová, J.; Uchman, M.; Šafařík, I.; Šafaříková, M.; Šlouf, M.; Pispas, S.; Štěpánek, M. *Colloids and Surfaces A: Physicochemical and Engineering Aspects* **2015**, 483, 1-7.
[129] Mountrichas, G.; Pispas, S. *J. Polym. Sci. A Polym. Chem*. **2007**, 45, 5790-5799.
[130] Hajduová, J.; Procházka, K, Raus, V.; Šlouf, M.; Krzyžánek, V.; Garamus, V.M.; Štěpánek, M. *Colloids and Surfaces A: Physicochemical and Engineering Aspects* **2014**, 456, 10-17.
[131] Uchman, M.; Hajduová, J.; Vlassi, E.; Pispas, S.; Appavou, M.S.; Štěpánek, M. *European Polymer Journal* 2015, 73, 212-221.

Appendix

Langmuir

Article

pubs.acs.org/Langmuir

Polyelectrolyte–Surfactant Complexes of Poly[3,5-bis(dimethylaminomethyl)-4-hydroxystyrene]-*block*-poly(ethylene oxide) and Sodium Dodecyl Sulfate: Anomalous Self-Assembly Behavior

Jana Hajduová,[†] Karel Procházka,[†] Miroslav Šlouf,[‡] Borislav Angelov,[‡] Grigoris Mountrichas,[§] Stergios Pispas,[§] and Miroslav Štěpánek*,[†]

[†]Department of Physical and Macromolecular Chemistry, Faculty of Science, Charles University of Prague, Hlavova 2030, 12840 Prague 2, Czech Republic

[‡]Institute of Macromolecular Chemistry, Academy of Sciences of the Czech Republic, Heyrovský Sq. 2, 16206 Prague 6, Czech Republic

[§]Theoretical & Physical Chemistry Institute, National Hellenic Research Foundation, 48 Vassileos Constantinou Avenue, 11635 Athens, Greece

ABSTRACT: Polyelectrolyte–surfactant complexes (PE–S) formed by double hydrophilic cationic polyelectrolyte poly[3,5-bis(dimethylaminomethyl)-4-hydroxystyrene]-*block*-poly(ethylene oxide) (NPHOS-PEO) and anionic surfactant sodium dodecyl sulfate (SDS) in acidic aqueous solutions were studied by light scattering, SAXS, and scanning transmission electron microcopy in the environmental mode (wet-STEM) for various stoichiometric ratios between the numbers of SDS anions and dimethylaminomethyl groups of NPHOS in the complex. The obtained results show that the NPHOS-PEO/SDS system behaves differently from other systems of double hydrophilic block polyelectrolyte and oppositely charged ionic surfactant because it forms water-insoluble PE–S for compositions close to the zero net charge of the complex. This phase separation occurs, instead of the PE–S rearrangement to core–shell particles, which is hindered due to conformational rigidity of the NPHOS blocks. For the surfactant amounts below and above the precipitation region, large spherical aggregates and their clusters are present in the solution. SAXS measurements indicate that although the NPHOS-PEO/SDS system does not form the core–shell particles with the NPHOS/SDS core and the PEO shell as other PE–S of double hydrophilic polyelectrolytes, the aggregates contain domains of closely packed surfactant micelles which bind to both NPHOS polyelectrolyte blocks and PEO blocks.

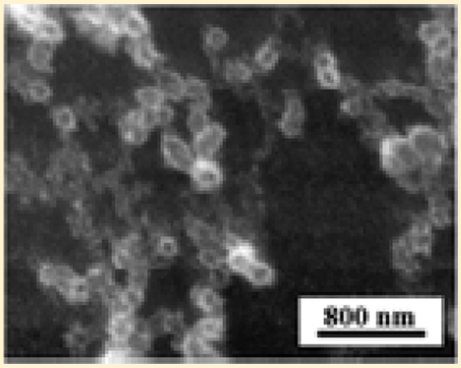

INTRODUCTION

Complexes of polyelectrolytes with oppositely charged surfactants have attracted the attention of many researchers in the past two decades due to general interest in nanostructured self-assembled systems and pharmaceutical and other applications of such materials.[1−3] Polyelectrolyte–surfactant complexes (PE–S) are stabilized by an entropic contribution to the free energy of the system from released counterions of the PE and by electrostatic interactions between the surfactant head groups and the polyelectrolyte side groups and hydrophobic interactions between the hydrophobic backbone of the polyelectrolyte and the alkyl chains of the surfactant. It has been found that the oppositely charged surfactant ions condense on the polyelectrolyte chains and form micelles at concentrations far below the surfactant critical micelle concentration (cmc) in the absence of the polyelectrolyte[4] and that water-insoluble stoichiometric PE–S with zero net charge form various water-insoluble-ordered crystalline-like phases.[5]

The interaction of oppositely charged ionic surfactants with double hydrophilic block polyelectrolytes, DHBP, consisting of a polyelectrolyte block and a neutral hydrophilic block [as poly(methacrylic acid)-*block*-poly(ethylene oxide)[6−8] or poly(acrylic acid)-*block*-poly(acrylamide)[9−11]], leads to the formation of core–shell nanoparticles with the core of the PE–S and the shell of the neutral hydrophilic block. Morphologies similar to those of amphiphilic diblock copolymers, including spherical[6−11] and wormlike[12] micelles or vesicles,[13] have been reported for a number of DHBP-containing PE–S in aqueous solution. SANS measurements reveal that the core of the nanoparticles contains densely packed surfactant micelles.[9,10]

The structural transition of a DHBP-containing PE–S to the core–shell particle, involving the segregation of the PE–S complex from the hydrophilic blocks, occurs when the system

Received: February 13, 2013
Revised: April 16, 2013
Published: April 16, 2013

attains a certain critical ratio, Z, between the amounts of the charges of the surfactant and of the polyelectrolyte units. In some cases, however, the structural transition to the core−shell particles does not occur, and the precipitation of the PE−S is observed instead. In our recent study,[14] we observed the latter behavior for the PE−S formed by poly[3,5-(trimethylammoniummethyl)-4-hydroxystyrene iodide]-*block*-poly(ethylene oxide) (QNPHOS-PEO) and sodium dodecyl sulfate (SDS) in salt-free aqueous solutions. SAXS studies of water-soluble PE−S of QNPHOS-PEO/SDS (Z below 0.6) confirmed that they did not form core−shell particles.

In this article, we extend our studies of the QNPHOS-PEO/SDS to a system containing poly[3,5-bis(dimethylaminomethyl)-4-hydroxystyrene)]-*block*-poly(ethylene oxide) (NPHOS-PEO), which is, in contrast to the strong polyelectrolyte studied earlier, an annealed polyelectrolyte; we also extend our studies to a broader range of Z. The structure of the PE−S aggregates formed by the NPHOS-PEO/SDS system have been investigated by a combination of static, dynamic and electrophoretic light scattering, SAXS, and scanning transmission electron microscopy in the environmental mode (wet-STEM). We show that due to the inability of the NPHOS-PEO/SDS aggregates to undergo the transition to core−shell particles, the stabilization of the NPHOS-PEO/SDS aggregates in aqueous media is secured only by electrostatic interactions so that the PE−S with the low charge close to zero are water-insoluble, while the excess copolymer or excess surfactant in the system lead to the formation of water-soluble complexes. The reported behavior resembles PE−S formed by homopolyelectrolytes rather than PE−S of DHBP, which self-assembles into core−shell particles thus providing their sterical stabilization in the aqueous solution.

EXPERIMENTAL SECTION

Materials. Poly[3,5-bis(dimethylaminomethyl)-4-hydroxystyrene]-*block*-poly(ethylene oxide) (NPHOS-PEO) copolymer (M_w = 62.7 kg/mol, M_w/M_n = 1.13, w_{PEO} = 0.14) was prepared by a postpolymerization modification of poly(*tert*-butoxystyrene)-*block*-poly(ethylene oxide) copolymer synthesized by anionic polymerization. Details on the synthesis and characterization of the sample are in ref 15. Solutions of NPHOS-PEO/SDS complexes were prepared by adding various amounts of freshly prepared 0.1 M stock solution of SDS in 0.1 M HCl to 1 mL of 1 mg/mL stock solution of NPHOS-PEO (corresponding to the molar amount of dimethylaminomethyl groups, n_{DMAM} = 6.60 μmol in 0.1 M HCl) under stirring and left 24 h prior to the measurements.

Methods. *Light Scattering (LS).* The light scattering setup (ALV, Langen, Germany) consisted of a 22 mW He−Ne laser, operating at the wavelength λ = 632.8 nm, an ALV CGS/8F goniometer, an ALV High QE APD detector, and an ALV 5000/EPP multibit, multitau autocorrelator. Both static and dynamic LS measurements were carried out at 25 °C in the angular range from 30° to 150°, corresponding in aqueous solutions to the scattering vector magnitudes q ranging from 6.8 to 25.6 μm^{-1}.

The normalized time autocorrelation functions of the scattered light intensity, $g^{(2)}(t,q)$, obtained by DLS, were fitted (i) with the aid of the constrained regularization algorithm (CONTIN) by the relationship,

$$g^{(2)}(t, q) = 1 + \beta\left[\int_0^\infty A(\tau, q)\exp\left(-\frac{t}{\tau}\right)d\tau\right]^2 \quad (1)$$

and (ii) by the second order cumulant expansion,

$$g^{(2)}(t, q) = 1 + \beta\exp[-2\Gamma_1(q)t + \Gamma_2(q)t^2] \quad (2)$$

where β is the coherence factor, $A(\tau,q)$ is the distribution of relaxation times τ, and $\Gamma_1(q)$ and $\Gamma_2(q)$ are the first and second moment of the distribution of relaxation rates. The distributions of apparent hydrodynamic radii R_H^{app} were calculated from $A(\tau,q)$ for q = 18.7 μm^{-1} (scattering angle θ = 90°), using the relationship for the apparent diffusion coefficient, $D_{app} = 1/\tau q^2$ and the Stokes−Einstein equation. The mean hydrodynamic radii (R_H) were calculated from the z-averaged diffusion coefficients obtained as $\Gamma_1(q)/q^2$ values extrapolated to zero q from their dependences on q^2.

Electrophoretic Light Scattering. ζ-Potential measurements were carried out with a Nano-ZS Zetasizer (Malvern Instruments, U.K.). ζ-Potential values were calculated from electrophoretic mobilities (average of three subsequent measurements, each of which consisted of 15−100 runs) using the Henry equation in the Smoluchowski approximation, $\mu = \varepsilon\zeta/\eta$, where μ is the electrophoretic mobility and ε is the dielectric constant of the solvent.

Wet-STEM. Scanning transmission electron microscopy (STEM) measurements were performed with a Quanta 200 FEG microscope (FEI, Hillsboro, OR), operated at the accelerating voltage of 30 kV in the environmental (wet-STEM) mode[16] (typical temperature and pressure in the microscope chamber were +1 °C and 500−700 Pa, respectively). All Wet-STEM micrographs were obtained as dark-field (DF) images using a standard two-segment circular solid-state detector placed below the sample. DF imaging was achieved by detecting electrons scattered to higher angles, which were collected in the opposite segment of the detector relative to the sample.

SAXS. Small-angle X-ray scattering experiments were performed at the ID02 beamline[17] of the European Synchrotron Radiation Facility in Grenoble, France. Two-dimensional (2D) SAXS patterns were recorded using a high-sensitivity low-noise CCD detector (FReLoN 4 M pixels), which was divided into 512 × 512 pixels after 4 × 4 binning. The X-ray wavelength and sample-to-detector distance were 0.1 nm and 1.5 m, respectively, corresponding to the accessible q-range from 0.07 to 3.2 nm^{-1}. The beam size was 350 × 270 μm^2. The readout dead time of the CCD detector was about 190 ms. The samples were filled in a flow-through quartz capillary cell (1.5 mm diameter, wall thickness 10 μm) mounted in a holder in air at room temperature (21 °C), without the need of a special vacuum chamber. Each SAXS pattern was an average of 20 frames of 4 ms and 10 frames of 40 ms. This scheme allowed for checking the reproducibility of the data and for avoiding the radiation damage that would have been a serious problem in case of a continuous exposure to the X-ray beam (~10^{13} photons/s). After each data acquisition sequence, the 2D images were corrected for dark current, detector spatial response function, etc. and normalized to the absolute intensity unit. Silver behenate was used for the q-range calibration and glassy carbon for the intensity normalization. The normalized 2D patterns were subsequently azimuthally averaged to obtain the one-dimensional (1D) scattering curves. The background scattering from the quartz capillary and the solvent were measured and processed in the same way as the sample. To perform the averaging and the background subtraction from the sample data, SAXS Utilities[18] was used.

RESULTS AND DISCUSSION

Unlike the previously studied quaternized copolymer QNPHOS-PEO,[14] its precursor NPHOS-PEO is a weak polybase. As most studies of PE−S containing weak double-hydrophilic polyelectrolytes (PMAA,[6−8] PAA[9−11]) were carried out in high ionic-strength buffers with pH sufficient for the full ionization of the electrolyte groups, we performed our studies in 0.1 M HCl for comparison of the results with similar PE−S systems. Here, we want to note that although sodium dodecyl sulfate undergoes hydrolysis in acidic solutions, its influence is negligible at the conditions and timescale of the experiment (the rate constant of SDS hydrolysis above cmc at pH 1 and 30 °C is 0.35 × 10^{-2} day^{-1}).[19]

After addition of SDS to NPHOS-PEO solutions in 0.1 M HCl, the formed complex precipitates for charge ratios Z from ca. 0.6 to 1.5. This behavior resembles that of homopolyelectrolyte PE−S, which are stabilized mainly electrostatically and

dx.doi.org/10.1021/la400583z | Langmuir 2013, 29, 5443−5449

become water-insoluble if their net charge is too low ($Z = \sim 1$). On the other hand, PE−S formed by DHBP typically coassemble in the core−shell nanoparticles, which are stabilized by the shell of neutral hydrophilic blocks. Interestingly, the solubility limit of $Z = 0.6$ for the NPHOS-PEO/SDS system is similar to the critical value at which the transition to core−shell particles occurs for other PE−S formed by DHBP, suggesting that the precipitation occurs as a result of the inability of the NPHOS-PEO/SDS to form a stabilizing core−shell structure.

Light Scattering Measurements. Figure 1 shows Guinier plots of the light scattering data for NPHOS-PEO/SDS

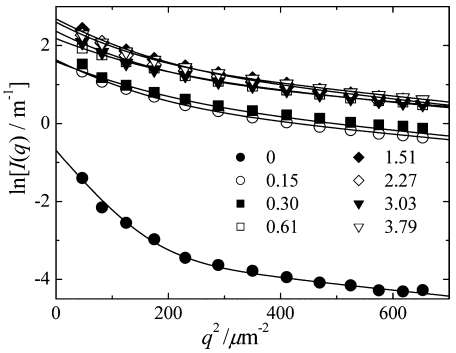

Figure 1. Guinier plots of static light scattering data from solutions of NPHOS-PEO/SDS complexes in 0.1 M HCl (copolymer concentration, c = 1 mg/mL) at various charge ratios, Z, indicated.

complexes in 0.1 M HCl at several Z ratios below and above the precipitation region. The slope of the curves decreases with increasing q^2. This shape of the scattering curve is typical for polydisperse systems in which the Guinier regime for larger particles appears at lower q^2 than that for smaller particles. On the basis of the discussion that follows, we approximately describe the scattering behavior of the NPHOS-PEO/SDS systems for Z from 0 to 3.8 by the sum of two effective Guinier contributions,

$$I(q) = I_1 \exp\left(-\frac{R_{g,1}^2 q^2}{3}\right) + I_2 \exp\left(-\frac{R_{g,2}^2 q^2}{3}\right) \quad (3)$$

where $R_{g,i}$ are effective gyration radii and I_i are forward-scattering intensities for the two contributions. The fits of the data by eq 3 are shown in Figure 1, proving that this simplified model describes the scattering of the system satisfactorily. Figure 2 shows the dependence of the $R_{g,i}$ and the forward scattering intensity $I(0) = I_1 + I_2$ both on Z and the molar amount of added SDS, n_{SDS}.

The scattering data indicate that very large scatterers appear already in the pure NPHOS-PEO solution, despite the low scattering intensity. The presence of large loose weakly scattering aggregates of both homopolyelectrolytes and double hydrophilic polyelectrolytes in aqueous solutions was reported previously. In the case of homopolyelectrolytes, it was hypothesized that these aggregates are metastable micro-phase-separated domains of concentrated polymer solution.[20]

After addition of SDS, the scattering intensity strongly increases, while the larger effective gyration radius $R_{g,1}$ drops from 231 to 172 nm as the smaller but denser PE−S aggregates with much larger scattering lengths are formed. Further increasing the amount of the surfactant in the complex results in the increasing scattering power of the PE−S particles up to

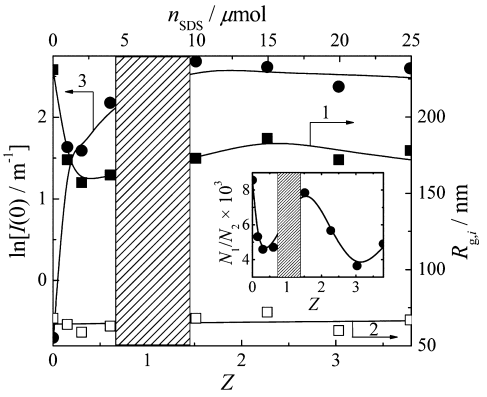

Figure 2. Apparent radii of gyration, $R_{g,1}$ (curve 1) and $R_{g,2}$ (curve 2), and forward scattering intensity, $I(0) = I_1 + I_2$ (curve 3), of NPHOS-PEO/SDS complexes in 0.1 M HCl obtained from fits of LS data shown in Figure 1 by eq 3, as functions of Z and the molar amount of SDS in the system, n_{SDS}. Precipitation region is shown as hatched area. Insert: N_1/N_2 ratio (eq 4), as a function of Z.

the lower precipitation limit, but the effective gyration radii reflecting the size distribution of the particles change only a little with Z. This fact indicates that the aggregates do not undergo the transition to the compact core−shell structure connected with a strong decrease of the particles size as was reported for other PE−S complexes of DHBP.[6−11]

In order to estimate the number-averaged radius of gyration of the polydisperse aggregates, let us consider that the Guinier terms in eq 3 correspond to particles with the scattering lengths, b_i, proportional to their volumes, $b_i \sim R_{g,i}^3$, as for homogeneous spheres of identical composition. The forward scattering intensities are then $I_i = N_i b_i^2$, in which N_i are numbers of the particles in the unit volume, and the N_1/N_2 ratio is

$$\frac{N_1}{N_2} = \frac{I_1}{I_2}\left(\frac{R_{g,2}}{R_{g,1}}\right)^6 \quad (4)$$

The N_1/N_2 values are plotted in the inset of Figure 2 as a function of Z, showing that the amount of large scatterers in the NPHOS-PEO/SDS system reaches the maximum at the precipitation limit at Z = 1.51. However, the N_1/N_2 value does not exceed 1%, which means that the number-averaged R_g is approximately equal to $R_{g,2}$ (about 70 nm). From this result, we can conclude that large particles dominating the scattering behavior in the low-q region ($\theta < 90°$) represent only a minority population among the scatterers in NPHOS-PEO/SDS solutions. We assume that they are formed by secondary aggregation of smaller PE−S particles.

Similarly to the results of static LS measurements, major changes in the scattering behavior revealed by dynamic LS occur after the first addition of SDS to the pure NPHOS-PEO solution, as shown in Figure 3, which depicts distributions of hydrodynamic radii at the scattering angle, $\theta = 90°$, and Figure 4, which shows the mean hydrodynamic radius calculated from the z-averaged diffusion coefficient as a function of Z and n_{SDS} (curve 1). For the pure NPHOS-PEO solution, the R_H^{app} distribution is bimodal, showing the diffusion of both individual NPHOS-PEO chains (with the hydrodynamic radius less than 10 nm and thus scattering in the Rayleigh regime in the studied q range) and their large polydisperse aggregates.

Results of the electrophoretic LS measurements are shown in Figure 4 (curve 2). After addition of the surfactant, the ζ

dx.doi.org/10.1021/la400583z | Langmuir 2013, 29, 5443−5449

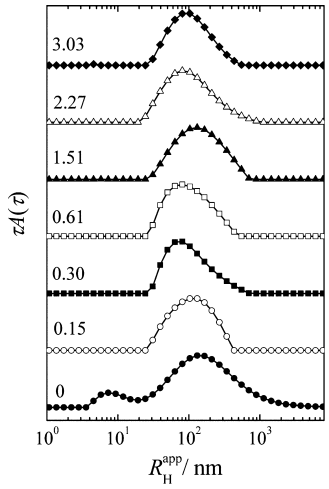

Figure 3. DLS distributions of apparent hydrodynamic radii, R_H^{app}, of NPHOS-PEO/SDS complexes in 0.1 M HCl at various charge ratios, Z.

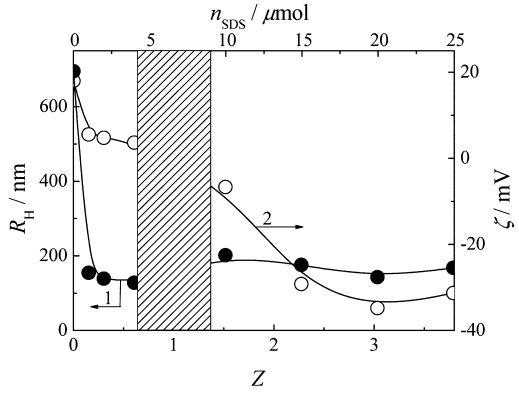

Figure 4. Hydrodynamic radius (curve 1) and ζ potential (curve 2) of NPHOS-PEO/SDS complexes in 0.1 M HCl. Precipitation region is shown as hatched area.

potential drops from +18 mV for the pure NPHOS-PEO solution to +6 mV for Z = 0.15 and further decreases only slightly below the precipitation region, being +4 mV at Z = 0.61. Above the precipitation region, ζ values decrease strongly with increasing Z to −31 mV at Z = 3.8. It is noteworthy that previously studied PE−S systems formed by DHBP have a much weaker tendency to overcharge at Z > 1.[8]

Since the electrophoretic mobilities of the particles are influenced mainly by the charges localized at the surface of the particles or close to their surface, the strong initial decrease in ζ can be explained by the preferential binding of the surfactant in the outer parts of the particle. The fact that the ζ potential values of the PE−S aggregates formed below the precipitation region are not sufficient for the electrostatic stabilization of the aggregates in the solution suggests that PEO blocks still play a role in keeping the particles soluble. On the other hand, the PE−S aggregates above the precipitation region are highly overcharged, indicating that the NPHOS-PEO/SDS particles are readily able to bind more SDS than its stoichiometric amount with respect to the amount of positive charges at NPHOS units. Here, we must note that due to the strong negative charge, the NPHOS-PEO/SDS system exhibits considerably better long-term stability in acidic aqueous solutions at Z > 1 than at Z < 1, where slow gradual precipitation of the PE−S complex can be observed on the timescale of weeks. Since it has been reported that SDS micelles, unlike those of cationic surfactants are able to bind at the PEO homopolymer,[21] the ability of the PE−S nanoparticles to adopt amounts of SDS strongly exceeding the stoichiometric ratio with respect to the polyelectrolyte charges can be explained not only by the adsorption of SDS on the surface of the particles but also by the formation of the PEO/SDS complex.

SAXS Measurements. As the light scattering measurements showed that the size of the PE−S particles changes only a little with their composition, we used SAXS in order to study their structure on shorter length scales. The SAXS curves for NPHOS-PEO/SDS solutions in 0.1 M HCl at several Z ratios below and above the precipitation region are shown in Figure 5.

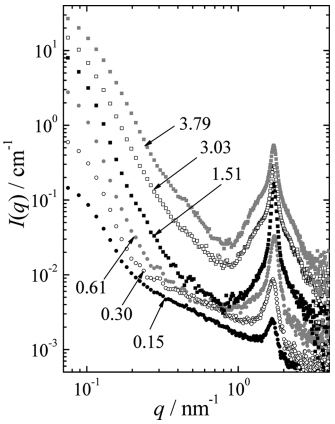

Figure 5. SAXS curves from solutions of NPHOS-PEO/SDS complexes in 0.1 M HCl at various charge ratios, Z. Intensities of the data are shifted by a multiplicative factor 2 for better readability.

The q-range of the SAXS experiment obviously does not allow for observing the entire Guinier region of the aggregates to determine their gyration radii, but it provides information about their internal structure. In our previous study,[14] we showed that the scattering from QNPHOS-PEO/SDS aggregates can be fitted by the mass-fractal model with additional terms for scattering from free QNPHOS-PEO coils and from the densely packed micelles in the complex. We want to note that in the case of the NPHOS-PEO/SDS system, this model describes well its scattering behavior below the precipitation region but not above it. Since it appears too difficult to find a model which would be suitable for the entire studied Z range of the NPHOS-PEO/SDS system, we have applied a model-free analysis of the curves, excluding the sub-Guinier range (0.07 − 0.2 nm^{-1}) and taking the intermediate-q range (0.2 − 0.8 nm^{-1}) and the high-q range (0.8 − 2 nm^{-1}) into account separately.

The scattering behavior at the intermediate-q range reflects the structure of the particles at the length scale of ∼8−30 nm, corresponding to the size of copolymer coils or small domains composed of either NPHOS or PEO blocks and by SDS micelles attached to the polymer chains. The scattering curve in this range can be roughly approximated by the power law, $I(q) \sim q^{-d}$, where d is the power-law exponent equal to the mass fractal dimension of the scatterers at the given length scale.[22] The values of d are shown in Figure 6 as a function of Z. As they accommodate increasing amounts of the surfactant without a significant increase in their size and the packing density of the aggregates thus increases, the fractal dimension of

dx.doi.org/10.1021/la400583z | Langmuir 2013, 29, 5443−5449

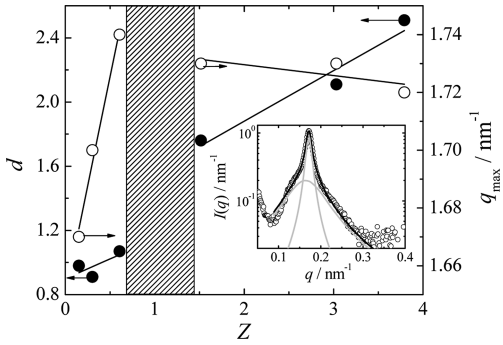

Figure 6. Power law exponent, d, and position of the maximum of the correlation peak, q_{max}, as functions of Z. Precipitation region is shown as hatched area. Inset: The SAXS scattering peak for Z = 3.79 and its fit by the sum of two Lorentzian functions.

the complexes grows with increasing Z from ca. 1.0 at Z = 0.15 to ca. 2.4 at Z = 3.8.

The high q-range of the scattering curve reflects the length scale of ∼3−8 nm, corresponding to the size of parts of the NPHOS-PEO chains and the size of SDS micelles. In this range, a pronounced scattering peak appears, growing with the increasing Z. This behavior is typical for PE−S complexes of both homopolyelectrolytes and double hydrophilic polyelectrolytes and is caused by the scattering from a locally ordered structure of densely packed surfactant micelles bound to the polyelectrolyte chains.[9,10] The q value of the maximum of the peak, q_{max}, is simply related to the distance between neighboring micelles l, as $q_{max} = 2\pi/l$.

The values of q_{max} as a function of Z are shown in Figure 6. Below the precipitation region, the increasing compactness of the structure with increasing Z is proved also by the shift of scattering peak maximum to higher q, which reflects the decrease of the distance between the SDS micelles in the complex. With the assumption that the structure of the packed micelles in the aggregate can be expressed by the structure factor for disordered cell−cell correlations,[23] the scattering function is Lorentzian:

$$I(q) = I_0 \frac{\xi^{-2}}{\xi^{-2} + (q - q_{max})^2} \quad (5)$$

where I_0 is the amplitude of the peak and ξ is the correlation length. While the scattering peaks at low Z can be described by the single Lorentzian function, those above the precipitation region are clearly composed of two Lorentzian contributions. The decomposition is shown for the complex with Z = 3.79 in the inset of Figure 6. It provides the peak maxima 1.65 and 1.72 nm^{-1}, corresponding to the intermicellar distances of 3.81 and 3.65 nm, respectively, and the correlation lengths of 2.0 and 13.4 nm. Since SDS micelles bind to both blocks of NPHOS-PEO, these two overlapping peaks correspond to the scattering from the micelles attached to the NPHOS blocks (a closely packed, more-ordered structure) and to the PEO blocks (a slightly more loosely packed, less-ordered structure).

In summary, the SAXS results confirm that no particles with the segregated core formed by the NPHOS/SDS complex and the shell of the PEO blocks formed the NPHOS-PEO/SDS system in 0.1 M HCl. Reasons for this behavior, which also explains the precipitation of the weakly charged aggregates from the solution can be both kinetical and sterical: The core/shell structure cannot be formed because of (i) the conformational rigidity of NPHOS chains, with bulky side groups on the PS backbone, and (ii) the high charge density on the NPHOS chain (two positive charges per monomeric unit), which precludes the accommodation of a sufficient amount of SDS micelles in the compact core with NPHOS blocks.

Wet-STEM Measurements. In order to supplement the scattering measurements, we employed electron microscopy (EM) for direct imaging of the PE−S particles. As conventional high vacuum EM is not a suitable method for studying loose colloidal aggregates which deform after evaporation of the solvent, we used scanning transmission electron microscopy in the environmental mode which allows for keeping the imaged particles in the swollen state.[16] Figure 7 shows dark field wet-STEM micrographs of NPHOS-PEO/SDS nanoparticles in 0.1 M HCl below (Z = 0.6) and above (Z = 3.0) the precipitation region. Both micrographs depict clusters of roughly spherical objects with the broad size distribution and the mean radius (number-averaged) of the about 50 nm. This value is well-comparable with the number-averaged gyration radius about 70 nm estimated from static LS measurements. Moreover, the extensive clustering shown on the micrographs is supportive for our assumption made on the basis of the light scattering data that a small fraction of PE−S particles undergoes secondary aggregation also in the diluted solution.

Unlike the particles at Z = 3.0, the aggregates below the precipitation region show up like rings having higher contrast on the border of the particle than in its center. This effect was reported earlier in wet-STEM microscopy for colloidal particles from aqueous dispersions stabilized by surfactants and explained by the presence of a surfactant layer at the surface of the particles, which increases the electron density.[24] In the case of the NPHOS-PEO/SDS system, the imaged aggregates are swollen with water at wet-STEM condition, so we can

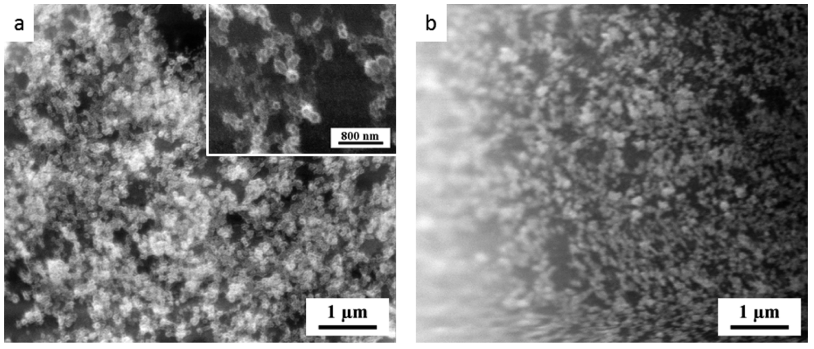

Figure 7. Wet-STEM micrographs of NPHOS-PEO/SDS particles at (a) Z = 0.6 and (b) Z = 3.0.

dx.doi.org/10.1021/la400583z | Langmuir 2013, 29, 5443−5449

assume that at lower Z, adsorption of the surfactant at the gas−liquid interface may lead to a higher concentration of SDS in the surface layer than in the center of the particle.

CONCLUSIONS

The aggregation behavior of the system composed of poly[3,5-bis(dimethylaminomethyl)-4-hydroxystyrene]-*block*-poly(ethylene oxide) and sodium dodecyl sulfate in acidic aqueous solution differs in several respects from that reported for similar systems of a double hydrophilic cationic polyelectrolyte and an oppositely charged ionic surfactant: (1) The size of the PE−S aggregates formed in the NPHOS-PEO/SDS system is almost independent of the charge ratio, Z. For Z in the range from 0.6 to 1.5, in which the ζ potential of the aggregates is low, the PE−S precipitates from the solution. These observations indicate that the aggregates in the solution are stabilized mostly electrostatically and no structural transition of the aggregates to smaller compact core/shell particles stabilized by the PEO shell occurs. (2) Zeta potential measurements show that the aggregates in the NPHOS-PEO/SDS system at higher Z (above the precipitation region) overcharge significantly, suggesting that they readily accommodate the surfactant micelles, which are in excess with respect to the positive charges on the NPHOS blocks. This observation can be explained as a result of the binding of SDS micelles to PEO blocks, which was reported in the literature for PEO homopolymer.[21] This explanation is supported by SAXS measurements, which indicate that above the precipitation region, two types of locally ordered structure of SDS micelles in the complex exist, of which one corresponds to the NPHOS/SDS complex and the other to the PEO/SDS complex.

AUTHOR INFORMATION

Corresponding Author

*E-mail: stepanek@natur.cuni.cz.

Notes

The authors declare no competing financial interest.

ACKNOWLEDGMENTS

The authors acknowledge the financial support from the Ministry of Education of the Czech Republic (long-term Research Project MSM0021620857) and the Czech Science Foundation (Grant 13-02938S). Electron microscopy measurements at the Institute of Macromolecular Chemistry were performed with the financial support through Grants TACR TE01020118 and RVO:61389013. B.A. acknowledges the beamtime from the project SC-3358 at the ID02 beamline of ESRF and thanks Drs. A. Angelova, S.K. Filippov, P. Štěpánek, and T. Narayanan for the cooperation and experimental support.

REFERENCES

(1) Voets, I. K.; de Keizer, A.; Stuart, M. A. C. Complex coacervate core micelles. *Adv. Colloid Interface Sci.* **2009**, *147−148*, 300−318.

(2) Langevin, D. Complexation of oppositely charged polyelectrolytes and surfactants in aqueous solutions. A review. *Adv. Colloid Interface Sci.* **2009**, *147−148*, 170−177.

(3) Zhou, S.; Chu, B. Assembled materials: Polyelectrolyte-surfactant complexes. *Adv. Mater.* **2000**, *12*, 545−556.

(4) Hansson, P. Self-assembly of ionic surfactants in polyelectrolyte solutions: A model for mixtures of opposite charge. *Langmuir* **2001**, *17*, 4167−4180.

(5) Kogej, K. Study of the effect of polyion charge density on structural properties of complexes between poly(acrylic acid) and alkylpyridinium surfactants. *J. Phys. Chem. B* **2003**, *107*, 8003−8010.

(6) Kabanov, A. V.; Bronich, T. K.; Kabanov, V. A.; Yu, K.; Eisenberg, A. Spontaneous formation of vesicles from complexes of block ionomers and surfactants. *J. Am. Chem. Soc.* **1998**, *120*, 9941−9942.

(7) Bronich, T. K.; Popov, A. M.; Eisenberg, A.; Kabanov, V. A.; Kabanov, A. V. Effects of block length and structure of surfactant on self-assembly and solution behavior of block ionomer complexes. *Langmuir* **2000**, *16*, 481−489.

(8) Bronich, T. K.; Kabanov, A. V.; Kabanov, V. A.; Yu, K.; Eisenberg, A. Soluble complexes from poly(ethylene oxide)-*block*-polymethacrylate anions and *N*-alkylpyridinium cations. *Macromolecules* **1997**, *30*, 3519−3528.

(9) Berret, J.-F.; Cristobal, G.; Hervé, P.; Oberdisse, J.; Grillo, I. Structure of colloidal complexes obtained from neutral/polyelectrolyte copolymers and oppositely charged surfactants. *Eur. Phys. J. E* **2002**, *9*, 301−311.

(10) Berret, J.-F.; Vigolo, B.; Eng, R.; Hervé, P.; Grillo, I.; Yang, L. Electrostatic self-assembly of oppositely charged copolymers and surfactants: A light, neutron, and X-ray scattering study. *Macromolecules* **2004**, *37*, 4922−4930.

(11) Courtois, J.; Berret, J.-F. Probing oppositely charged surfactant and copolymer interactions by isothermal titration microcalorimetry. *Langmuir* **2010**, *26*, 11750−11758.

(12) Štěpánek, M.; Škvarla, J.; Uchman, M.; Procházka, K.; Angelov, B.; Kováčik, L.; Garamus, V. M.; Mantzaridis, C.; Pispas, S. Wormlike core-shell nanoparticles formed by co-assembly of double hydrophilic block polyelectrolyte with oppositely charged fluorosurfactant. *Soft Matter* **2012**, *21*, 9412−9417.

(13) Solomatin, S. V.; Bronich, T. K.; Eisenberg, A.; Kabanov, V. A.; Kabanov, A. V. Nanomaterials from ionic block copolymers and single-, double-, and triple-tail surfactants. *Langmuir* **2007**, *23*, 2838−2842.

(14) Štěpánek, M.; Matějíček, P.; Procházka, K.; Filippov, S. K.; Angelov, B.; Šlouf, M.; Mountrichas, G.; Pispas, S. Polyelectrolyte−surfactant complexes formed by poly[3,5-bis(trimethylammoniummethyl)-4-hydroxystyrene iodide]-*block*-poly(ethylene oxide) and sodium dodecyl sulfate in aqueous solutions. *Langmuir* **2011**, *27*, 5275−5281.

(15) Mountrichas, G.; Pispas, S. Novel double hydrophilic block copolymers based on poly(*p*-hydroxystyrene) derivatives and Poly(Ethylene oxide). *J. Polym. Sci., Part A: Polym. Chem.* **2007**, *45*, 5790−5799.

(16) Šlouf, M.; Lapčíková, M.; Štěpánek, M. Imaging of block copolymer vesicles in solvated state by wet scanning transmission electron microscopy. *Eur. Polym. J.* **2011**, *47*, 1273−1278.

(17) Panine, P.; Finet, S.; Weiss, T. M.; Narayanan, T. Probing fast kinetics in complex fluids by combined rapid mixing and small-angle X-ray scattering. *Adv. Colloid Interface Sci.* **2006**, *127*, 9−18.

(18) On-Line Processing and Analysis of SAXS Data. http://www.sztucki.de/SAXSutilities/ (accessed Nov 1, 2012).

(19) Motsavage, V. A.; Kostenbauder, H. B. Influence of state of aggregation on specific acid-catalyzed hydrolysis of sodium dodecyl sulfate. *J. Colloid Sci.* **1963**, *18*, 603−615.

(20) Yun, S. I.; Briber, R. M.; Kee, A. R.; Gauthier, M. Dilute-solution structure of charged arborescent graft polymer. *Polymer* **2006**, *47*, 2750−2759.

(21) Barbosa, A. M.; Santos, I. J. B.; Ferreira, G. M. D.; da Silva, M. D. H.; Teixeira, A. V. N. D.; da Silva, L. H. M. Microcalorimetric and SAXS determination of PEO−SDS interactions: The effect of cosolutes formed by ions. *J Phys. Chem. B* **2010**, *114*, 11967−11974.

(22) Putnam, C. D.; Hammel, M.; Hura, G. L.; Tainer, J. A. X-ray solution scattering (SAXS) combined with crystallography and computation: Defining accurate macromolecular structures, conformations and assemblies in solution. *Q. Rev. Biophys.* **2007**, *40*, 191−285.

(23) Lei, N.; Safinya, C. R.; Roux, D.; Liang, K. S. Synchrotron x-ray-scattering studies on the sodium dodecyl sulfate−water−pentanol−dodecane L3 sponge phase. *Phys. Rev. E* **1997**, *56*, 608−613.

(24) Bogner, A.; Thollet, G.; Basset, D.; Jouneau, P.-H.; Gauthier, C. Wet STEM: A new development in environmental SEM for imaging nano-objects included in a liquid phase. *Ultramicroscopy* **2005**, *104*, 290−301.

Colloids and Surfaces A: Physicochem. Eng. Aspects 456 (2014) 10–17

Contents lists available at ScienceDirect

Colloids and Surfaces A: Physicochemical and Engineering Aspects

journal homepage: www.elsevier.com/locate/colsurfa

Structure of polymeric nanoparticles in surfactant-stabilized aqueous dispersions of high-molar-mass hydrophobic graft copolymers

Jana Hajduová[a], Karel Procházka[a], Vladimír Raus[b], Miroslav Šlouf[b], Vladislav Krzyžánek[c], Vasil M. Garamus[d], Miroslav Štěpánek[a,*]

[a] Department of Physical and Macromolecular Chemistry, Faculty of Science, Charles University in Prague, Hlavova 2030, 128 40 Prague 2, Czech Republic
[b] Institute of Macromolecular Chemistry, Academy of Sciences of the Czech Republic, Heyrovský Sq. 2, 162 06 Prague 6, Czech Republic
[c] Institute of Scientific Instruments, Academy of Sciences of the Czech Republic, Královopolská 147, 61264 Brno, Czech Republic
[d] Helmholtz-Zentrum Geesthacht, Centre for Materials and Coastal Research, D-21502 Geesthacht, Germany

HIGHLIGHTS

- Aqueous dispersions of Cel-g-PS contain clusters of collapsed macromolecules.
- The size of the clusters can be tuned by changing the copolymer concentration.
- The aggregates are stabilized by SDS entrapped in the collapsed macromolecules.

GRAPHICAL ABSTRACT

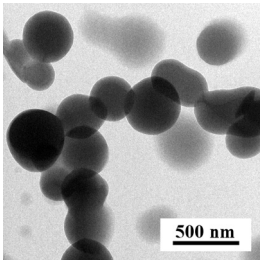

ARTICLE INFO

Article history:
Received 13 March 2014
Received in revised form 24 April 2014
Accepted 29 April 2014
Available online 9 May 2014

Keywords:
Nanoprecipitation
Graft copolymer
Light scattering
SAXS
TEM

ABSTRACT

Aqueous dispersions of hydrophobic high-molar-mass cellulose-*graft*-polystyrene (Cel-g-PS) copolymers were prepared by nanoprecipitation from 1,4-dioxane solutions using sodium dodecyl sulfate as a stabilizer. The size and structure of formed Cel-g-PS nanoparticles were studied by scattering techniques (static and dynamic light scattering, SAXS) and transmission electron microscopy. The scattering and microscopy data show that nanoprecipitation of Cel-g-PS leads to the formation of polydisperse aggregates of collapsed Cel-g-PS macromolecules containing entrapped SDS micelles in the kinetically frozen state. The final size of the aggregates can be tuned by changing the copolymer concentration, c_P, in the dioxane solution. The average hydrodynamic radius of the aggregates, R_H, scales as $[(R_H/R_{H,0})^{2.5} - 1] \sim c_P$, where $R_{H,0}$ is the R_H value extrapolated to the zero copolymer concentration.

1. Introduction

Polymer-surfactant interactions have been extensively studied in the last two decades with respect to the preparation of self-assembled nanoparticles and nanostructured materials with promising applications both in medicine and in technology [1–4]. Many studies in this field have been focused to complexes of polyelectrolytes and oppositely charged ionic surfactants. Since polyelectrolyte–surfactant complexes are water-insoluble close to the zero net charge, co-assembly of block copolymers consisting of a polyelectrolyte block with oppositely charged surfactants allows for preparation of nanoparticles with the core of the insoluble complex and the shell of the neutral blocks [4–6].

In the case of neutral hydrophobic polymers, surfactants are often used as stabilizers in order to prepare polymeric nanoparticles in aqueous media. These can either be prepared by emulsion

* Corresponding author. Tel.: +420 2 2195 1290; fax: +420 2 2491 9752.
E-mail address: stepanek@natur.cuni.cz (M. Štěpánek).

http://dx.doi.org/10.1016/j.colsurfa.2014.04.059
0927-7757/

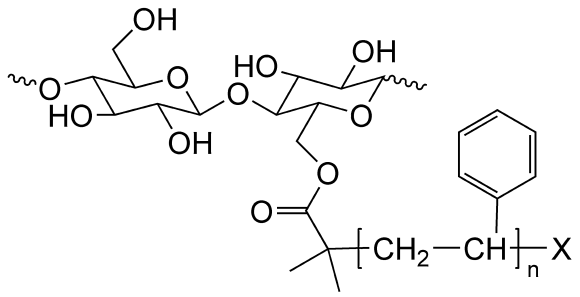

Scheme 1. Structure of cellulose-*graft*-polystyrene copolymers.

polymerization, in which nanoparticles are formed from hydrophobic monomer nanodroplets dispersed in the aqueous medium [7–9], or by nanoprecipitation, which consists in formation of polymer nanoparticles by microphase separation of the polymer after mixing the polymer solution in a water-miscible organic solvent with water. The latter technique, which has been widely used in pharmacology for preparation of carrier vessels for drug delivery [10–12], is the subject of this paper.

Even though there are a number of articles about nanoprecipitation of polymers, most of them aim at encapsulation properties and pharmacological applications, while only a very few of them are focused on the structure of nanoprecipitated particles [13]. Furthermore, nanoprecipitation studies usually deal with low-molar-mass polymers which behave as liquids and coalesce into compact particles [14], the size of which scales with the aggregation number as $R{\sim}N_{agg}^{1/3}$. In this paper, we present a study of nanoparticles prepared by the nanoprecipitation of cellulose-*graft*-polystyrene (Cel-g-PS) copolymers with the molar mass of the order of 10^6 g mol^{-1} and high grafting densities. Our goal is to address the question whether the nanoprecipitation of such large dense macromolecules occurs as coalescence or whether it rather resembles the aggregation of solid particles. In the latter case, the aggregation process results in formation of fractal particles, so that $R{\sim}N_{agg}^{1/d}$, where d is the fractal dimension which is about 1.8 for the diffusion-limited aggregation process [15].

We use two Cel-g-PS samples differing in the grafting density and sodium dodecyl sulfate (SDS) as a stabilizing surfactant. The structure of the nanoparticles is investigated by microscopic (TEM) and scattering (light scattering, SAXS) techniques. We also study the dependence of the size of the particles on the concentration of the copolymer in 1,4-dioxane solution and the surfactant in the aqueous solution.

2. Experimental

2.1. Materials

Cellulose-*graft*-polystyrene (Cel-g-PS) copolymers (Scheme 1) were prepared by the "grafting-from" technique by atom transfer radical polymerization using the macroinitiator prepared by acylation of microcrystalline cellulose by 2-bromoisobutyryl bromide under homogeneous reaction conditions in the N,N-dimethylacetamide/LiCl solvent system. Two samples differing in the grafting density were used for the study (Table 1). Details on the synthesis and characterization of the samples are given in [16].

Cel-g-PS aqueous dispersions were prepared by adding 0.1 mL of the Cel-g-PS solution (1–10 mg/mL) in 1,4-dioxane dropwise into 0.9 mL of aqueous sodium dodecyl sulfate (SDS) solution (1–100 mM) under vigorous stirring. Excess SDS was removed by dialysis against deionized water. The ζ-potential of the nanoparticles in aqueous dispersions was found to be about −30 mV and independent of the SDS concentration in the aqueous solution before the dialysis. The dispersions prepared from 10 mg/mL Cel-g-PS dioxane solutions and 0.1 M aqueous SDS (the final concentration of the copolymers in the dispersion was thus 1 mg/mL) were used for electron microscopy and SAXS measurements. For LS measurements, the dispersions were further diluted with deionized water to achieve the final copolymer concentration 0.1 mg/mL.

2.2. Light scattering

The light scattering setup (ALV, Langen, Germany) consisted of a 22 mW He–Ne laser, operating at the wavelength $\lambda = 632.8$ nm, an ALV CGS/8F goniometer, an ALV High QE APD detector and an ALV 5000/EPP multibit, multitau autocorrelator. Both static and dynamic LS measurements were carried out at 25 °C in the angular range 30°–150° corresponding in aqueous solutions to the scattering vector magnitudes q ranging from 6.8 μm^{-1} to 25.6 μm^{-1}.

Refractive index increment measurements were carried out at 25 °C using a Wyatt T-ReX differential refractometer. The aqueous solutions of FSN-100 in four different concentrations were pumped into the refractometer by a syringe driven by a 78-9100C Cole Parmer syringe drive with a flow rate of 1 mL/min. The refractive index value, $dn/dc_P = 0.17$ mL g^{-1}, was determined from the slope of the plot of the refractive index versus concentration.

Since both Cel-g-PS copolymers in the dioxane solution are too large to obtain reliable results from the Zimm analysis, the static light scattering (SLS) measurements were treated by the Berry method which was shown to be more proper for polymer coils with gyration radius larger than 50 nm [18]. The data were thus fitted to the equation

$$\left[\frac{Kc_P}{\Delta R_\theta(q, c_P)}\right]^{1/2} = \frac{1}{M_w^{1/2}}\left(1 + \frac{1}{6}R_g^2q^2 + \cdots\right)^{1/2}(1 + M_wA_2c_P) \quad (1)$$

where M_w, and A_2, respectively, are the weight-averaged molar mass, R_g^2 is the z-averaged squared radius of gyration and A_2 is the "light-scattering-averaged" osmotic second virial coefficient of the polymer in the solution, $\Delta R_\theta(q,c_P)$ is the corrected Rayleigh ratio which depends on the polymer concentration c_P and on the magnitude of the scattering vector $q = (4\pi n_0/\lambda)\sin(\theta/2)$, where θ is the scattering angle, n_0 is the refractive index of the solvent and λ is the wavelength of the incident light. The contrast factor K is given by the relationship $K = 4\pi^2n_0^2(dn/dc_P)^2/(\lambda^4N_A)$, where dn/dc

Table 1
Characterization of Cel-g-PS-I and Cel-g-PS-II copolymers.

Sample	M_n^{gr} kg mol^{-1} [a]	M_w/M_n [b]	g [c]	M_n^{th}, $\times10^3$ kg mol^{-1} [d]	M_w^{gr}, $\times10^3$ kg mol^{-1} [e]
Cel-g-PS-I	12.2	1.35	0.42	0.587	1.15
Cel-g-PS-II	11.2	1.18	1.04	1.182	2.32

[a] Number averaged molar mass of a PS graft by SEC.
[b] Dispersity of a PS graft by SEC.
[c] Grafting density.
[d] Theoretical number-averaged molar mass of the copolymers, $M_n^{th} = (M_b/M_{gl})g(M_n^{graft}+M_{gl})$, where $M_b = 16.2$ kg mol^{-1} is the number-averaged molar mass of the backbone and $M_{gl} = 0.162$ kg mol^{-1} is the molar mass of the glucose unit.
[e] Theoretical number-averaged molar mass of the copolymers assuming the dispersity $Đ = 1.96$ calculated from the dispersities of the backbone and the grafts [17].

is the refractive index increment of the polymer with respect to the solvent, and N_A is the Avogadro constant.

Dynamic light scattering measurements were evaluated by fitting the measured normalized time autocorrelation function of the scattered light intensity, $g^{(2)}(t)$, related to the electric field autocorrelation function, $g^{(1)}(t)$, by the Siegert relation, $g^{(2)}(t) = 1 + \beta|g^{(1)}(t)|^2$.

The data, collected for various copolymer concentrations and scattering angles were fitted (i) with the aid of the constrained regularization algorithm (CONTIN) which provides the distribution of relaxation times τ, $A(\tau)$, as the inverse Laplace transform of $g^{(1)}(t)$ function

$$g^{(1)}(t) = \int_0^\infty A(\tau)\exp\left(-\frac{t}{\tau}\right)d\tau, \quad (2)$$

and (ii) to the second order cumulant expansion

$$g^{(1)}(t) = \exp\left(-\Gamma_1 t + \frac{\Gamma_2}{2}t^2\right), \quad (3)$$

where Γ_1 and Γ_2, respectively, are the first and the second moment (that is, the mean and the variance) of the distribution function of relaxation rates. The z-averaged diffusion coefficient of the particles, $\langle D\rangle_z$, was obtained by the linear extrapolation to zero q and c_P values as

$$\frac{\Gamma_1(q, c_P)}{q^2} = D_z(1 + CR_g^2q^2 + \cdots)(1 + k_D c_P), \quad (4)$$

where C is the structure parameter dependent of the shape and degree of polydispersity of the particles and k_D is the hydrodynamic virial coefficient. The variance to the square of the mean ratio, $\mu = \Gamma_2/\Gamma_1^2$, is a measure of the dispersity of the diffusion coefficient.

The average hydrodynamic radius (the z-average of R_H^{-1}) was calculated from D_z, by means of the Stokes–Einstein formula

$$R_H = \frac{k_B T}{6\pi\eta_0 D_z}, \quad (5)$$

where k_B is the Boltzmann constant, T is the temperature and η_0 is the viscosity of the solvent. The $A(\tau)$ distributions can be recalculated to the distributions of apparent hydrodynamic radii, R_H^{app}, using the relationship

$$R_H^{app} = \frac{k_B T q^2}{6\pi\eta_0}\tau. \quad (6)$$

2.3. Electrophoretic light scattering

ζ-Potential measurements were carried out with a Nano-ZS Zetasizer (Malvern Instruments, UK). ζ-Potential values were calculated from electrophoretic mobilities (average of three subsequent measurements, each of which consisted of 15–100 runs) using the Henry equation in the Smoluchowski approximation, $\mu = \varepsilon\zeta/\eta$, where μ is the electrophoretic mobility and ε is the dielectric constant of the solvent.

2.4. Transmission electron microscopy

TEM micrographs were obtained with a Tecnai G2 Spirit Twin 12 microscope (FEI, Czech Republic) at 120 kV using bright field imaging and various tilt angles (0° and 50°). The samples were prepared as follows: 2 μL of Cel-g-PS copolymer solution in dioxane or nanoparticle dispersion in water (the copolymer concentration was, c_P = 1 mg/mL, in both cases) were dropped onto a copper TEM grid (300 mesh) coated with thin, electron-transparent carbon film. The solution was sucked out by touching the bottom of the grid with filtering paper. This fast removal of the solution was performed after 1 min in order to suppress oversaturation during the drying process.

2.5. Small-angle X-ray scattering

SAXS experiments were performed on the P12 BioSAXS beamline at the storage ring PETRA III of the Deutsche Elektronen Synchrotron (DESY, Hamburg, Germany) at 20 °C using a Pilatus 2 M detector and synchrotron radiation with the wavelength of λ = 0.12 nm. The sample-detector distance was 4.1 m, allowing for measurements in the q-range interval from 0.07 to 4.6 nm^{-1}. The q range was calibrated using the diffraction patterns of silver behenate. A sample of approximately 20 μL was illuminated. The experimental data were normalized to the incident beam intensity, corrected for non-homogeneous detector response, and the background scattering of the solvent was subtracted. The solvent scattering was measured before and after the sample scattering to control for possible sample holder contamination. 20 diffraction patterns originating from the same sample volume were recorded, using an exposure time of 0.05 s. This background-corrected SAXS data were used to calculate one-dimensional scattering curves by angular averaging. This background-corrected SAXS data were used to calculate one-dimensional scattering curves by angular averaging using an automated acquisition and analysis program [19,20].

3. Results and discussion

3.1. Characterization of Cel-g-PS copolymers by light scattering

Prior to the preparation of nanoprecipitated particles, both Cel-g-PS copolymers were studied in 1,4-dioxane solutions at concentrations ranging from 1 to 10 mg/mL by static and dynamic LS in order to determine their molar mass, size and interaction parameters. Berry plots and dynamic Zimm plots of the scattering data for both copolymers are shown in Fig. 1. They are qualitatively similar for both samples with the exception of the sign of the hydrodynamic virial coefficient. Since $k_D = 2M_wA_2 - k_f - \nu$, where k_f is the second virial coefficient of the friction coefficient and ν is the molar volume of the scattering particles, the positive value of k_D for Cel-g-PS-II indicates that $2M_wA_2$ dominates over the negative contribution k_f (ν is negligible both to $2M_wA_2$ and k_f for the polymer of this molar mass), unlike the case of Cel-g-PS-I.

The results obtained from the evaluation of the scattering data (Eqs. (1, 4 and 5)) are summarized in Table 2. The negative value of k_D for Cel-g-PS-I is in accordance with Yamakawa's theory [21], which predicts the value of the virial coefficient of the friction coefficient as $k_f = 1.2M_wA_2 + 4\pi N_A R_H^3/3M_w$. Using this approximation, M_w, R_H and A_2 obtained by the analysis of the scattering data provide the k_D values of -5.57×10^{-2} $dm^3\,g^{-1}$ for Cel-g-PS-I and 3.57×10^{-2} $dm^3\,g^{-1}$ for Cel-g-PS-II which are in good agreement with the experimental values of k_D.

Similarly to the previous study [16], the molar masses of both samples are significantly higher than those calculated from the known grafting densities and molar masses of the grafts and backbones. Moreover, the molar mass of Cel-g-PS-II is more than four times higher than that of Cel-g-PS-I, although according to the grafting densities, M_w of both samples should differ only by the factor of approximately two. It has been hypothesized that the discrepancy between calculated M_w^{theor} and measured M_w can be ascribed to a partial intermolecular recombination of growing polystyrene chains, resulting in covalent bonding between different copolymer molecules [16]. Since the probability of the formation of a crosslink of two backbones via the recombination of the grafts increases with the increasing number of grafts, this assumption is supported by the fact that the difference between M_w^{theor} and measured M_w is larger for the sample with the higher grafting density. The higher dispersity of the diffusion coefficient for Cel-g-PS-II than for Cel-g-PS-I is also in accordance with the

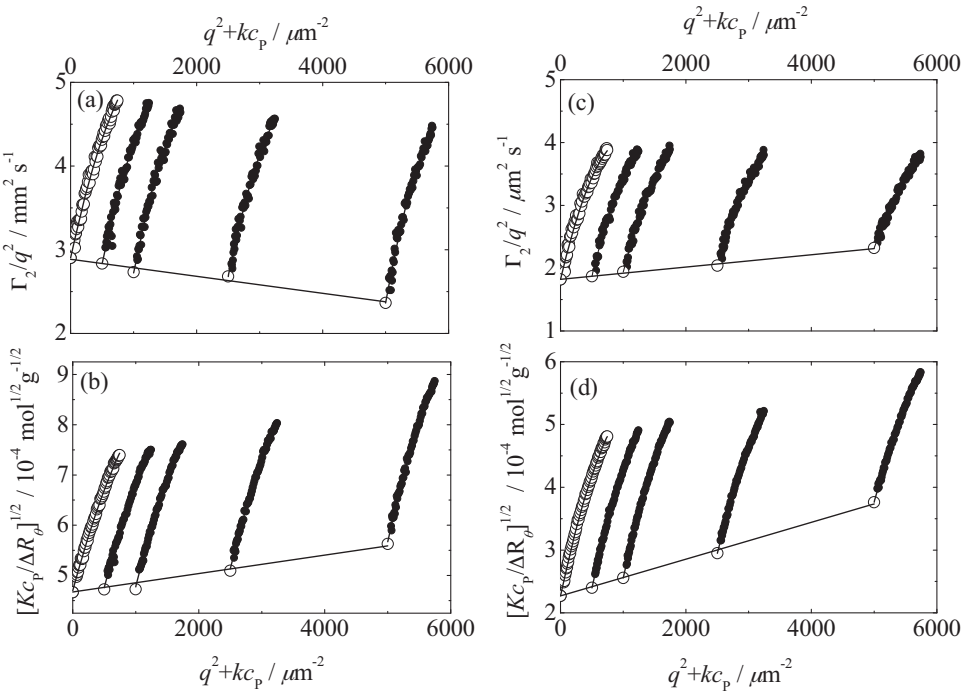

Fig. 1. Dynamic Zimm plots (a,c) and Berry plots (b,d) of the static and dynamic light scattering data from solutions of Cel-g-PS-I (a,b) and Cel-g-PS-II (c,d) in 1,4-dioxane. Plot constant $k = 500\,\mathrm{L\,g^{-1}\,\mu m^{-2}}$.

Table 2
Characteristics of Cel-g-PS copolymers obtained by LS measurements in 1,4-dioxane solutions.

Sample	M_w, $\times 10^6$ g mol^{-1}	R_g, nm	A_2, $\times 10^{-9}$ mol dm^3 g^{-2}	R_H, nm	k_D, $\times 10^{-2}$ dm^3 g^{-1}	μ[a]
Cel-g-PS-I	4.7	79	9.78	56	−2.83	0.33
Cel-g-PS-II	20.0	113	6.74	83	3.61	0.41

[a] Calculated as $\Gamma_2/\Gamma_1{}^2$ ratio for $q \to 0$ and $c_P = 1$ mg/mL.

assumption that Cel-g-PS-II copolymer contains more crosslinked Cel-g-PS macromolecules than Cel-g-PS-I.

3.2. Cel-g-PS nanoparticles in aqueous dispersions

Light and small-angle X-ray scattering were used in order to elucidate the structure of Cel-g-PS nanoparticles in water. Fig. 2 shows LS curves of aqueous dispersions of Cel-g-PS-I and Cel-g-PS-II. In the q range covered by the LS measurements, corresponding to the lengthscales from ca. 800 to ca. 250 nm, an intermediate regime between the Guinier and power-law scattering behavior is observed. Fitting the curves by the Fisher–Burford structure factor [22],

$$I(q) = I_0\left(1 - \frac{2}{3\alpha_1}R_g^2 q^2\right)^{\alpha_1/2} \quad (7)$$

where, I_0 is the forward scattering intensity, R_g is the gyration radius and α_1 is the exponent in the power law regime, provides the values of the particle gyration radius, 260 nm for Cel-g-PS-I and 269 nm for Cel-g-PS-II. The gyration radii can be compared with the results of dynamic LS measurements (Fig. 3). The obtained apparent diffusion coefficients are strongly q-dependent. While the increase of D_{app} with q is due to polydispersity of the aggregates and due to the contribution of their internal dynamics to the autocorrelation function, the decreasing part of the dependence for high q is caused by back reflected light [23]. Hydrodynamic radii calculated from the diffusion coefficients extrapolated to zero q are 226 nm for Cel-g-PS-I and 238 nm for Cel-g-PS-II, yielding the R_g/R_H ratios, ρ, 1.15 for Cel-g-PS-I and 1.13 for Cel-g-PS-II.

The power-law exponent α_1 obtained from the fits of Eq. (7) is −3.25 for Cel-g-PS-I and −3.46 for Cel-g-PS-II. Since $-3 > \alpha_1 > -4$, the scattering above the Guinier region comes mainly from the surface of the aggregates. The values of α_1 in this range generally indicate the rough surface (with the surface fractal dimension $d_s = 6 + \alpha_1$) but the decreased power-law exponent can also be a result of the polydispersity of the system.

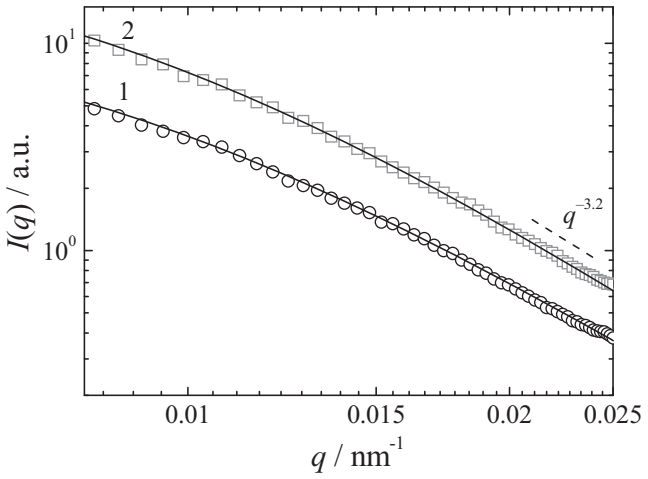

Fig. 2. Static LS curves for Cel-g-PS-I (curve 1) and Cel-g-PS-II (curve 2) aqueous dispersions.

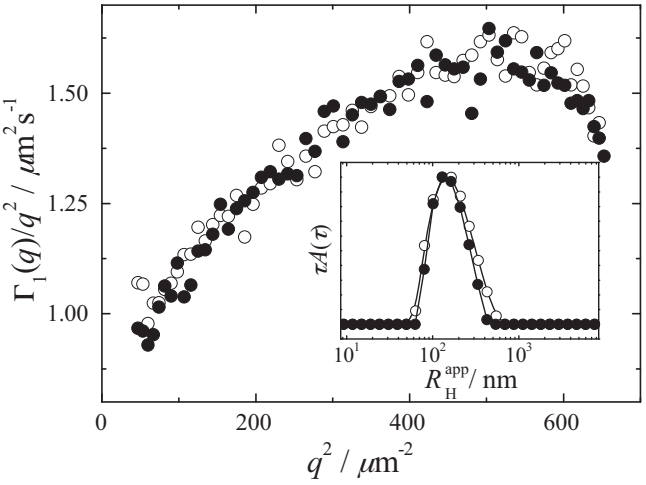

Fig. 3. Dynamic Zimm plots for Cel-g-PS-I (solid circles) and Cel-g-PS-II (open circles) in aqueous dispersions. Insert: CONTIN distributions of apparent hydrodynamic radii for Cel-g-PS-I (solid circles) and Cel-g-PS-II (open circles) at the scattering angle $\theta = 90^\circ$.

In the case of Cel-g-PS dispersions, the surface fractal dimension of the aggregates can be influenced by both factors. Firstly, the large collapsed Cel-g-PS macromolecules are not flexible and cannot merge into an aggregate with the sharp interface. Secondly, since the average R_g of the aggregates is only three to five times larger than that of the Cel-g-PS macromolecules in the dioxane solutions, the aggregates have highly irregular shape and are highly structurally heterogeneous. Moreover, also the individual Cel-g-PS macromolecules are polydisperse due to the above-mentioned formation of crosslinks between the cellulose backbones.

Fig. 4 shows SAXS scattering curves in the q range corresponding to the lengthscale from 104 to 2 nm which probe the internal structure of the collapsed particles forming the aggregate. The scattering in this region exhibits the power law behavior, except for the high-q region where a weak peak appears for both dispersions. Treating the correlation peak as the simple Lorentzian function (the structure factor for disordered cell–cell correlations [24]), the curve can be fitted by the following empirical scattering function

$$I(q) = I_0 q^{\alpha_2} + \frac{I_1 \xi^{-2}}{\xi^{-2} + (q - q_c)^2}, \quad (8)$$

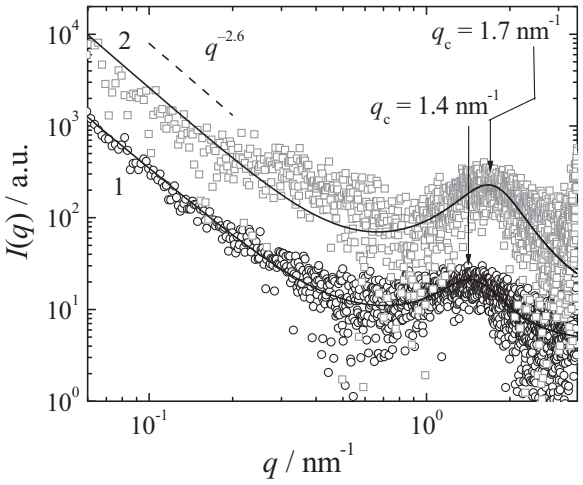

Fig. 4. SAXS curves for Cel-g-PS-I (curve 1) and Cel-g-PS-II (curve 2) aqueous dispersions.

where I_0 and I_1 are prefactors, ξ is the full width in the half-maximum of the peak (the correlation length) and q_c is the center of the peak. The fit provides the values of the exponent α_2 about −2.6 (−2.53 for Cel-g-PS-I and −2.63 for Cel-g-PS-II), indicating that the particles have a dense, but not fully collapsed structure with the mass fractal dimension $d_m = -\alpha_2$. The fact that the aggregates are not fully collapsed is evidenced also by the fairly large value of the R_g/R_H ratio around 1.1.

The maxima of the peaks, q_c, are 1.44 nm^{-1} for Cel-g-PS-I and 1.67 nm^{-1} for Cel-g-PS-II and indicate a local ordering at the lengthscale, $l = 2\pi/q_c$, of ca. 3–4 nm. Since this value is close to the diameter of SDS micelles, the peak suggests the presence of the packed SDS micelles in the particles (similarly to polyelectrolyte–surfactant complexes, in which this behavior can be much more pronounced [25]). Let us remind that the dispersions remain stable (the particles keep the negative zeta potential of about −30 mV) even though they undergo dialysis during which free surfactant is removed from the solution. This behavior clearly indicates that the Cel-g-PS/SDS complex is in a kinetically frozen state so that a fraction of SDS remains trapped in the interior of the collapsed Cel-g-PS macromolecules.

3.3. Transmission electron microscopy

TEM was used to visualize the structure of Cel-g-PS macromolecules before (Fig. 5a–d) and after (Fig. 6a–d) the nanoprecipitation process. The aggregation was observed not only on the micrographs of the samples obtained by drying of the aqueous dispersions (Fig. 6a–d) but also on those prepared from the solutions in 1,4-dioxane (Fig. 5a–d) which suggests that the observed aggregates form rather as a result of the deposition of the copolymer on the TEM grid and drying.

The micrographs clearly show that the mean diameter of the particles from the aqueous dispersions (about 170 ± 80 nm for both Cel-g-PS-I and Cel-g-PS-II) is larger than those from 1,4-dioxane (about 100 ± 40 nm). This difference suggests that the large particles deposited from the 1,4-dioxane solutions are fused aggregates of several Cel-g-PS macromolecules. In the case of aqueous dispersions, the fusion is not possible because the collapsed macromolecules loaded with the surfactant lack flexibility to do so. This explanation is supported by the micrographs obtained at the tilt angle of 50°, which reveal that the nanoprecipitated macromolecules from the aqueous dispersions are less flattened than those deposited from the dioxane solutions.

In order to study the influence of the sample preparation process on the observed particles, we employed two other scanning transmission electron microscopy (STEM) techniques: (i) In the case of 1,4-dioxane solutions, the samples were freeze dried and observed in high vacuum STEM. (ii) In the case of the aqueous dispersions, we studied the hydrated state by means of wet-STEM (STEM in the environmental mode as described in Supplementary Material). In both cases, the images corresponded to those obtained by fast-drying at the room temperature followed by high-vacuum TEM microscopy. For the results and the experimental details of STEM techniques, see the Supplementary Material.

3.4. Dependence of Cel-g-PS particle size on copolymer and surfactant concentration

Since the formation of the nanoprecipitated particles is controlled both by the aggregation of Cel-g-PS macromolecules and by the adsorption of SDS on the formed aggregates which hinders the aggregation process, it can be expected that the size of the resulting particles will change with changing the initial polymer and SDS concentrations, c_P (from 1 to 10 mg/mL) and c_{SDS} (from

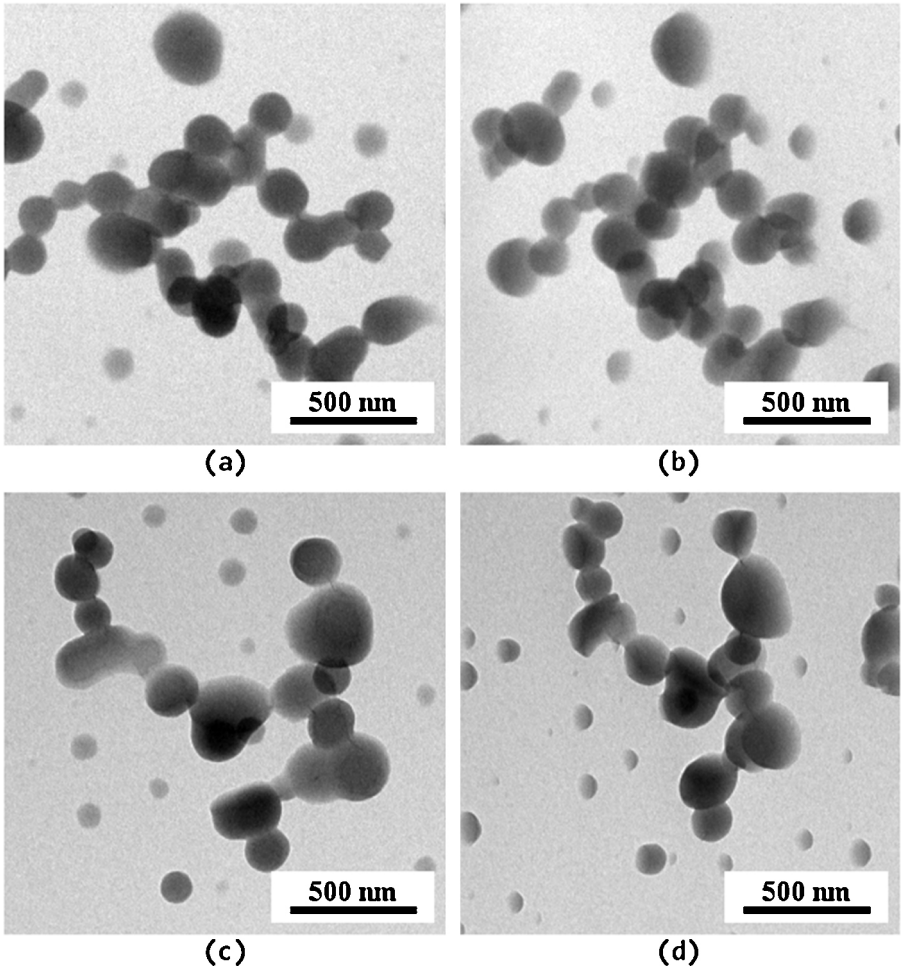

Fig. 5. Transmission electron micrographs of Cel-g-PS macromolecules from 1,4-dioxane solutions: (a,b) Cel-g-PS-I, (c,d) Cel-g-PS-II, at tilt angles of 0° (a,c) and 50° (b,d).

1 to 100 mM), in the preparation protocol described in the Experimental Section. Let us first consider the case of the size dependence on c_P in the excess of the surfactant. In this case, long-range electrostatic interactions are suppressed due to the high ionic strength of the solution and the aggregation process is then limited only by the diffusion of the copolymer macromolecules. (This does not contradict the observed fractal dimension of the aggregates which is higher than that corresponding to the diffusion-limited cluster aggregation regime [15] because in our case the fractal dimension is determined mainly by the internal structure of the collapsed Cel-g-PS macromolecules and polydispersity of the aggregates.) For the diffusion-limited coalescence process [14], the characteristic size of the aggregates grows with the time as $R^3(t) = R_0^3[1 + t/\tau]$, where τ is the characteristic coalescence time which is inversely proportional to the concentration of the copolymer, c_P, and R_0 is the initial size of the particles, that is, the size of the singe collapsed Cel-g-PS macromolecule. Therefore, taking into account that in our case the aggregation number scales with the size as $N_{agg} \sim R^d$, where $d = 2.53$ is the mass fractal dimension, and assuming further that the characteristic time of mixing at which the aggregates reach their maximum size is independent on c_P, the increase in the particle size with the copolymer concentration should scale as $(R^d - R_0^d) \sim c_P$.

Fig. 7 shows R_H^d, where R_H is the hydrodynamic radius of Cel-g-PS-I aggregates at $c_{SDS} = 100$ mM and $d = 2.53$ is their fractal dimension obtained from SAXS, as a function of c_P (curve 1). In accordance with the above-mentioned theoretical considerations, the dependence is linear, providing the extrapolated value of the initial hydrodynamic radius, $R_{H,0} = 122$ nm. The mean radius of the Cel-g-PS macromolecules on the micrographs of the aqueous dispersions (Fig. 6a–d) is lower (about 50 nm) but it is necessary to keep in mind that we compare the number averaged value with the hydrodynamic radii from DLS which is based on the *z*-averaged diffusion coefficient.

In connection with the observed value of the scaling exponent *d*, it is worth mentioning that the dependence of the nanoprecipitated particle size on the polymer concentration was investigated previously for various polymer dispersions and besides the scaling behavior predicted by the diffusion limited coalescence theory ($R_H^3 \sim c_p$) [26], the linear dependence of R_H on c_P was also reported [27]. Since this behavior cannot be explained by the deviation of the scaling of the particles size with the aggregation number like in our case (the linear dependence of R_H on N_{agg} would not be possible), it suggests that in some cases nanoprecipitation is controlled by the different kinetics of aggregation.

In the case that we follow the R_H of the aggregates as a function of c_{SDS} (at $c_P = 1$ mg/mL), the slight decrease in the hydrodynamic radius with the decreasing SDS concentration is observed (Fig. 7, curve 2). (SDS concentrations below 1 mM were insufficient for the stabilization of the nanoparticles and macroscopic precipitation of the copolymer was observed.) This result is surprising because for many other dispersions prepared by nanoprecipitation, the exactly opposite effect (that is, the decreasing particle size with the increasing surfactant concentration) was observed due to the fact that the higher is the surfactant concentration, the faster is the surfactant adsorption on the surface of the particles which prevents their further growth. The different behavior of our system

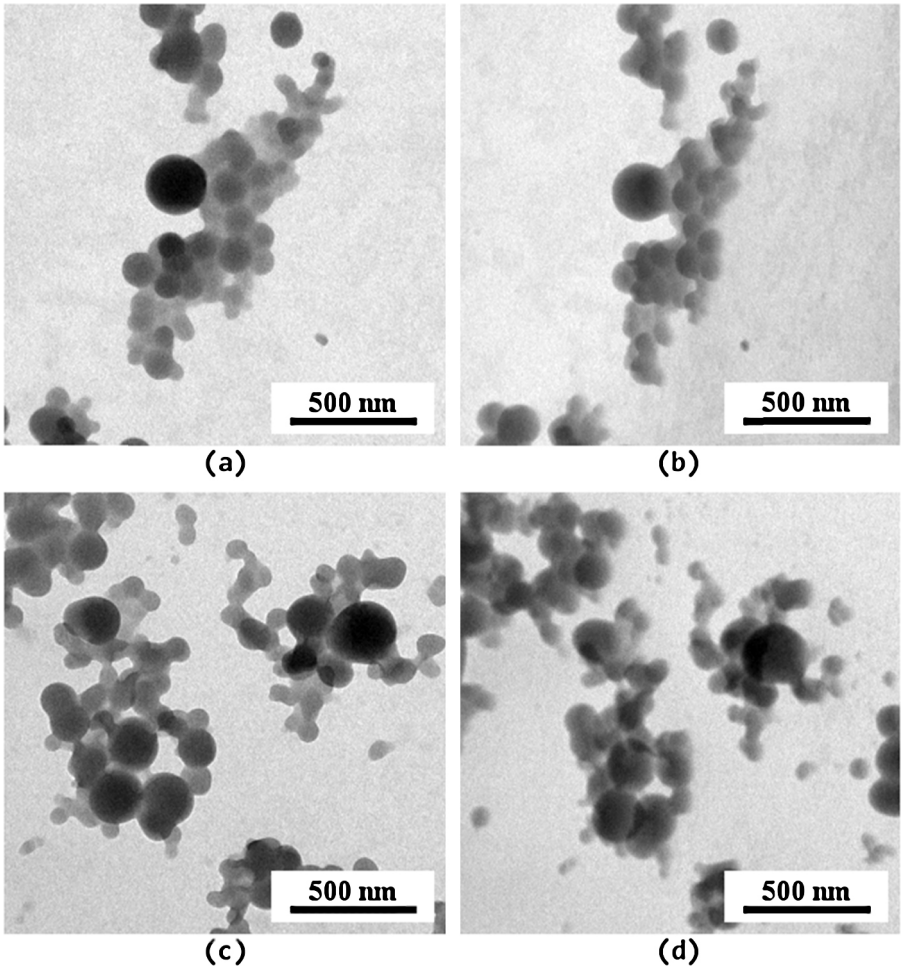

Fig. 6. Transmission electron micrographs of Cel-g-PS nanoparticles from aqueous dispersions: (a,b) Cel-g-PS-I, (c,d) Cel-g-PS-II, at tilt angles if 0° (a,c) and 50° (b,d).

probably stems from the fact that we use a ionic surfactant which stabilizes the particles electrostatically, so that the effect of the increasing adsorption rate with increasing c_{SDS} is suppressed by the opposite effect of the screening of electrostatic repulsion between individual Cel-g-PS-I macromolecules as the increasing amount of the excess surfactant in the solution increases its ionic strength. A similar behavior has been reported in studies of the influence of electrolytes on nanoprecipitation [28].

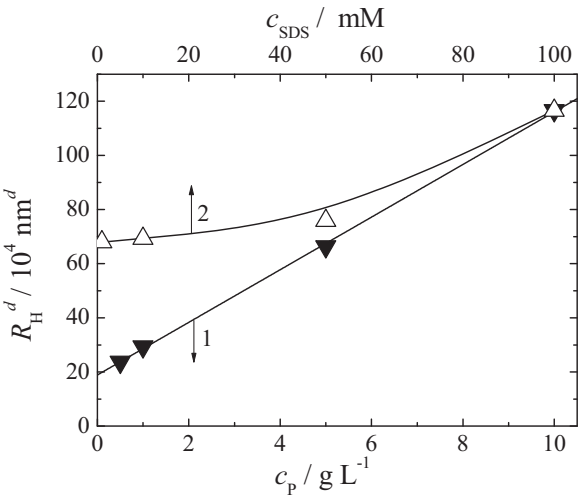

Fig. 7. R_H^d, where R_H are the hydrodynamic radii of the nanoprecipitated particles of Cel-g-PS-I and $d = 2.53$ is their fractal dimension, as functions of the copolymer concentration in the 1,4-dioxane solution, c_P (curve 1), and of SDS concentration in the aqueous solution, c_{SDS} (curve 2).

4. Conclusion

In this paper, we have studied the structure of nanoparticles in aqueous dispersions prepared by nanoprecipitation of high-molar-mass densely grafted cellulose-*graft*-polystyrene copolymers from 1,4-dioxane solutions. Scattering and transmission electron microscopy measurements show that the aggregation of Cel-g-PS in the presence of sodium dodecyl sulfate leads to the formation of polydisperse clusters of individual collapsed macromolecules, the size of which can be tuned by changing the Cel-g-PS concentration in the 1,4-dioxane solution which is mixed with the aqueous SDS. The aggregates are electrostatically stabilized by SDS molecules entrapped in the collapsed Cel-g-PS macromolecules (SAXS in the high-q region indicates that the particles contain densely packed SDS micelles). The surfactant cannot escape from the interior of the particles and keeps them negatively charged when the dispersion is subject to dialysis and excess SDS molecules are removed from the solution. Therefore we can conclude that the collapse of Cel-g-PS macromolecules in aqueous solutions in the presence of SDS leads to the formation of compact particles so that their aggregation resembles rather that of solid colloids than that of small polymer coils.

Acknowledgments

The authors acknowledge the Czech Science Foundation and the Technology Agency of the Czech Republic for funding (Grants P106-12-0143 and TE01020118, respectively) and Dr. Clément Blanchet for the kind support at the P12 BioSAXS beamline (EMBL/DESY, PETRA III).

Appendix A. Supplementary data

Supplementary data associated with this article can be found, in the online version, at http://dx.doi.org/10.1016/j.colsurfa.2014.04.059.

References

[1] D.J.F Taylor, R.K. Thomas, J. Penfold, Polymer/surfactant interactions at the air/water interface, Adv. Colloid Interface Sci. 132 (2007) 69–110.
[2] K.C. Tam, E. Wyn-Jones, Insights on polymer surfactant complex structures during the binding of surfactants to polymers as measured by equilibrium and structural techniques, Chem. Soc. Rev. 35 (2006) 693–709.
[3] D. Langevin, Complexation of oppositely charged polyelectrolytes and surfactants in aqueous solutions. A review, Adv. Colloid Interface Sci. 147–148 (2009) 170–177.
[4] S. Zhou, B. Chu, Assembled materials: polyelectrolyte–surfactant complexes, Adv. Mater. 12 (2000) 545–556.
[5] L. Vitorazi, J.F. Berret, W. Loh, Self-assembly of complex salts of cationic surfactants and anionic-neutral block copolymers. Dispersions with liquid-crystalline internal structure, Langmuir 29 (2013) 14024–14033.
[6] M. Uchman, M. Štěpánek, S. Prévost, B. Angelov, J. Bednaár, M.S. Appavou, M. Gradzielski, K. Procházka, Coassembly of poly(ethylene oxide)-block-poly(methacrylic acid) and N-dodecylpyridinium chloride in aqueous solutions leading to ordered micellar assemblies within copolymer aggregates, Macromolecules 45 (2012) 6471–6480.
[7] M. Antonietti, K. Landfester, Polyreactions in miniemulsions, Prog. Polym. Sci. 27 (2002) 689–757.
[8] E. Bourgeat-Lami, G.A. Farzi, L. David, J.L. Putaux, T.F.L. McKenna, Silica encapsulation by miniemulsion polymerization: distribution and localization of the silica particles in droplets and latex particles, Langmuir 28 (2012) 6021–6031.
[9] L.L. Hecht, C. Wagner, K. Landfester, H.P. Schuchmann, Surfactant concentration regime in miniemulsion polymerization for the formation of MMA nanodroplets by high-pressure homogenization, Langmuir 27 (2011) 2279–2285.
[10] C.E. Mora-Huertas, H. Fessi, A. Elaissari, Polymer-based nanocapsules for drugdelivery, Int. J. Pharm. 385 (2010) 113–142.
[11] S.M. D'Addio, R.K. Prud'homme, Controlling drug nanoparticle formation by rapid precipitation, Adv. Drug Delivery Rev. 63 (2011) 417–426.
[12] Z. Ye, E. Squillante, The development and scale-up of biodegradable polymeric nanoparticles loaded with ibuprofen, Colloids Surf. A Physicochem. Eng. Aspects 422 (2013) 75–80.
[13] A. Jager, D. Gromadzki, E. Jager, F.C. Giacomelli, A. Kozlowska, L. Kobera, J. Brus, B. Říhová, M. El Fray, K. Ulbrich, P. Štěpánek, Novel "soft" biodegradable nanoparticles prepared from aliphatic based monomers as a potential drug delivery system, Soft Matter 8 (2012) 4343–4354.
[14] R. Stepanyan, J.G.J.L. Lebouille, J.J.M. Slot, R. Tuinier, M.A.C. Stuart, Controlled nanoparticle formation by diffusion limited coalescence, Phys. Rev. Lett. 109 (2012), Art. No. 138301.
[15] M.Y. Lin, H.M. Lindsay, D.A. Weitz, R.C. Ball, R. Klein, P. Meakin, Universality in colloid aggregation, Nature 339 (1989) 360–362.
[16] V. Raus, M. Štěpánek, M. Uchman, M. Šlouf, P. Látalová, P. Čadová, M. Netopilík, J. Kříž, J. Dybal, P. Vlček, Cellulose-based graft copolymers with controlled architecture prepared in a homogeneous phase, J. Polym. Sci. A: Polym. Chem. 49 (2011) 4353–4367.
[17] K. Dušek, M. Netopilík, P. Kratochvíl, Nonuniformities of distributions of molecular weights of grafted polymers, Macromolecules 45 (2012) 3240–3246.
[18] M. Andersson, B. Wittgren, K.G. Wahlund, Accuracy in multiangle light scattering measurements for molar mass and radius estimations. Model calculations and experiments, Anal. Chem. 75 (2003) 4279–4291.
[19] D. Franke, A.G. Kikhney, D.I. Svergun, Automated acquisition and analysis of small angle X-ray scattering data, Nucl. Instrum. Methods A 689 (2012) 52–59.
[20] http://www.embl-hamburg.de/biosaxs/download.html (accessed 1.08.13).
[21] H. Yamakawa, Modern Theory of Polymer Solutions, Harper & Row, London, 1971.
[22] M.D. Haw, W.C.K. Poon, P.N. Pusey, Structure and arrangement of clusters in cluster aggregation, Phys. Rev. E 56 (1997) 1918–1933.
[23] S. Bantle, M. Schmidt, W. Burchard, Simultaneous static and dynamic light scattering, Macromolecules 15 (1982) 1604–1609.
[24] N. Lei, C.R. Safinya, D. Roux, K.S. Liang, Synchrotron X-ray-scattering studies on the sodium dodecyl sulfate–water–pentanol–dodecane L3 sponge phase, Phys. Rev. E 56 (1997) 608–613.
[25] J. Hajduová, K. Procházka, M. Šlouf, B. Angelov, G. Mountrichas, S. Pispas, M. Štěpánek, Polyelectrolyte–surfactant complexes of poly[3,5-bis(dimethylaminomethyl)-4-hydroxystyrene]-block-poly(ethyleneoxide) and sodium dodecyl sulfate: anomalous self-assembly behavior, Langmuir 29 (2013) 5443–5449.
[26] J. Cheng, B.A. Teply, I. Sherifi, J. Sung, G. Luther, F.X. Gu, E. Levy-Nissenbaum, A.F. Radovic-Moreno, R. Langer, O.C. Farokhzad, Formulation of functionalized PLGA-PEG nanoparticles for in vivo targeted drug delivery, Biomaterials 28 (2007) 869–876.
[27] A.M. de Oliveira, M. Anderson, E. Jager, A. Jager, P. Stepanek, F.C. Giacomelli, Physicochemical aspects behind the size of biodegradable polymeric nanoparticles: a step forward, Colloids Surf. A: Physicochem. Eng. Aspects 436 (2013) 1092–1102.
[28] C. Zhang, V.J. Pansare, R.K. Prud'homme, R.D. Priestley, Flash nanoprecipitation of polystyrene nanoparticles, Soft Matter 8 (2012) 86–93.

Colloids and Surfaces A: Physicochem. Eng. Aspects 483 (2015) 1–7

Contents lists available at ScienceDirect

Colloids and Surfaces A: Physicochemical and Engineering Aspects

journal homepage: www.elsevier.com/locate/colsurfa

Aggregation of superparamagnetic iron oxide nanoparticles in dilute aqueous dispersions: Effect of coating by double-hydrophilic block polyelectrolyte

Jana Hajduová[a], Mariusz Uchman[a], Ivo Šafařík[b], Miroslava Šafaříková[b], Miroslav Šlouf[c], Stergios Pispas[d], Miroslav Štěpánek[a,*]

[a] Department of Physical and Macromolecular Chemistry, Faculty of Science, Charles University in Prague, Hlavova 2030, 12840 Prague 2, Czech Republic
[b] Department of Nanobiotechnology, Institute of Nanobiology and Structural Biology of GCRC, Na Sádkách 7, 370 05 České Budějovice, Czech Republic
[c] Institute of Macromolecular Chemistry, Academy of Sciences of the Czech Republic, Heyrovský Sq. 2, 16206 Prague 6, Czech Republic
[d] Theoretical & Physical Chemistry Institute, National Hellenic Research Foundation, 48 Vassileos Constantinou Ave., 11635 Athens, Greece

HIGHLIGHTS

- Coating of magnetic nanoparticles by block polyelectrolyte affects their aggregation.
- Clusters of polyelectrolyte-coated magnetic nanoparticles form linear aggregates.
- Non-diffusive internal dynamics of the aggregates was observed.

GRAPHICAL ABSTRACT

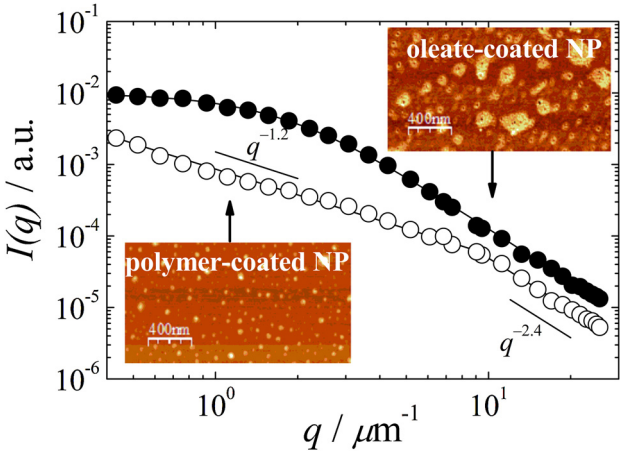

ARTICLE INFO

Article history:
Received 19 May 2015
Received in revised form 1 July 2015
Accepted 3 July 2015
Available online 11 July 2015

Keywords:
Magnetic nanoparticles
Block polyelectrolytes
Aggregation
Small-angle light scattering

ABSTRACT

Polymer-coated superparamagnetic iron oxide nanoparticles (SPION) in aqueous dispersion were prepared by the coassembly of SPION coated by an oleate bilayer with the double hydrophilic block polyelectrolyte poly[(3,5-bis(trimethylammoniummethyl)-4-hydroxystyrene iodide]-*block*-poly(ethylene oxide) (QNPHOS-PEO) and characterized by TEM and AFM. It was found that the coating by QNPHOS-PEO affects their aggregation into larger structures on the micrometer length scale observed by small-angle light scattering as well as the dynamics of the dispersion observed by dynamic light scattering. Oleate-SPION in aqueous dispersions form compact aggregates with the fractal dimension, $D = 2.4$, and the characteristic size about 2 μm which exhibit internal dynamics manifesting itself by the presence of the relaxation mode with $\tau \sim q^{-3}$. In the case of QNPHOS-PEO/oleate-SPION dispersions, the polyelectrolyte coating promotes the formation of compact clusters with the size of the order of $\sim 10^2$ nm. The

* Corresponding author. Tel.: +420 221951290.
E-mail address: stepanek@natur.cuni.cz (M. Štěpánek).

http://dx.doi.org/10.1016/j.colsurfa.2015.07.008

clusters, weakly interacting by magnetic dipolar interactions, form linear chainlike aggregates with the low fractal dimension, $D = 1.2$. The dynamics of the QNPHOS-PEO/oleate-SPION dispersions observed by DLS is dominated by the diffusion of the clusters.

1. Introduction

Superparamagnetic iron oxide nanoparticles (SPION) of magnetite (Fe_3O_4) or maghemite (γ-Fe_2O_3) [1–3] have been extensively studied in connection with their applications in technology as magnetic fluids [4] or in medicine as systems for magnetic hyperthermia therapy [5], targeted drug delivery systems [6,7] or as contrast agents for magnetic resonance imaging [6,7]. In these applications, it is essential to obtain stable aqueous dispersions of SPION. Therefore, various kinds of biocompatible coatings have been tested for the stabilization of SPIONs in aqueous media [8,9].

Even though concentrated aqueous dispersions of coated iron oxide SPION (ferrofluids) can exhibit excellent long-term stability, they are apt to aggregate upon dilution because of desorption of the coating agent from the SPION [10]. In addition to Van der Waals attractive forces among the particles, anisotropic magnetic dipole interactions can play a role in the aggregation process. It was observed by several authors [11–14], that in applied magnetic field SPION or nanoparticles with encapsulated SPION form one-dimensional chainlike aggregates or self-assembled structures. It has also been reported that in diluted aqueous dispersions of surfactant-coated SPIONs, chainlike aggregates with the fractal dimension $D = \sim 1.2$ were formed spontaneously [10,15].

Double hydrophilic block polyelectrolytes (DHBP), that is, block copolymers consisting of a hydrophilic neutral block and a polyelectrolyte block, represent a promising group of materials that can be used for stabilizing magnetic SPION in aqueous dispersions [14,16,17]. The DHBP layer can simply be formed by mixing electrostatically stabilized coated SPION with an oppositely charged DHBP. Electrostatic co-assembly of both components leads to the formation of mixed nanoparticles with protective shells formed by the neutral block of the DHBP which are stable in diluted dispersion, even though the self-assembly process usually leads to the formation of small SPION clusters that form the core of the hybrid co-assembled particle [17]. Coating by DHBP represents a generally applicable process leading to the formation of biocompatible colloids with many potential applications. Not only iron oxide nanoparticles, but also nanoparticles constituted of gold semiconductors (quantum dots) or other inorganic materials coated by block copolymers have been prepared and applied as tags or labels in bioassays and in biochips or nanobiosensors with the purpose to detect DNA or proteins in small volumes within a reduced time [18].

In this article, we compare the aggregation behavior of iron oxide SPION coated by a bilayer of oleate (oleate-SPION) and the SPION provided with an additional layer of cationic block polyelectrolyte poly[(3,5-bis(trimethylammoniummethyl)-4-hydroxystyrene iodide]-*block*-poly(ethylene oxide) [19,20] (QNPHOS-PEO/oleate-SPION) that were prepared by co-assembly of QNPHOS-PEO with the negatively charged oleate-SPION. The nanoparticles and their aggregates are characterized on the length scales from 1 nm to tens of μm using transmission electron microscopy, atomic force microscopy and light scattering techniques including small-angle light scattering. We show that the coating of the SPION significantly changes both the internal dynamics (observed by dynamic light scattering) and the structure (observed by small-angle static light scattering) of the aggregates formed in dilute aqueous dispersions.

2. Experimental

2.1. Materials

2.1.1. QNPHOS-PEO copolymer

QNPHOS-PEO copolymer ($M_w = 100.7\ kg\ mol^{-1}$, the weight fraction of the PEO block, $w_{PEO} = 0.14$) was prepared from the poly(*t*-butoxy styrene)-*block*-poly(ethylene oxide) precursor synthesized by the sequential living anionic polymerization. Details on the synthesis and characterization are given in [19].

2.1.2. Synthesis of oleate-SPION

In order to prepare oleate-stabilized iron oxide nanoparticles (oleate-SPION), 2.10 g of $FeCl_3 \cdot 6H_2O$ and 1.1 g of $FeSO_4 \cdot 7H_2O$ were dissolved in 40 ml of water. Then 10 ml of 25% ammonium hydroxide solution was added under intensive stirring with a mechanical overhead stirrer at 460 rpm. The black precipitate formed was 5-times washed with water and then 25 ml of water and 0.75 g of sodium oleate was added. The beaker was covered by an aluminum sheet and the mixture was stirred at 460 rpm and heated on a water bath at 80 °C for one hour. The resulting dispersion (magnetic fluid) was centrifuged at $7700 \times g$ for 30 min to remove the remaining precipitate. The pH of the dispersion was around 10 and the concentration of iron oxide nanoparticles was, $c_{NP} = 34\ g\ l^{-1}$.

2.1.3. Coating of oleate-SPION by QNPHOS-PEO

QNPHOS-PEO/oleate-SPION dispersions were prepared according to the following protocol: 29.4 μl of the oleate-SPION dispersion ($c_{NP} = 34\ g\ l^{-1}$) was added to 4 ml of deionized water in a 22 ml glass vial under shaking by a vortex mixer at 560 rpm. Then various amounts of $10\ g\ l^{-1}$ aqueous stock solution of QNPHOS-PEO ranging from 125 μl to 5 ml were added dropwise (ca. 1 ml/min) under shaking at 560 rpm and the resulting mixed dispersions were diluted with deionized water so that their total volume was 10 ml. In such dispersions, the concentration of oleate-SPION was, $c_{NP} = 1\ g\ l^{-1}$ and QNPHOS-PEO concentrations, c_P, ranged from 0.25 to $5\ g\ l^{-1}$.

The mixed dispersions were then left to stand at least 24 h prior to the further use. For some measurements, the dispersions had to be further diluted as indicated below. The above mentioned procedure provided the best results in terms of reproducibility and stability of the mixed dispersions. We note that the dilution of the oleate-SPION dispersions prior to coating was a prerequisite to avoiding precipitation of the nanoparticles after mixing with QNPHOS-PEO.

2.2. Methods

2.2.1. Small-angle light scattering

SALS measurements were performed at a Mastersizer 3000 instrument (Malvern, UK) equipped with a Hydro SV dispergation unit. 0.5 ml of the sample ($c_{NP} = 1\ g\ l^{-1}$) was injected to 6.5 ml of deionized water in the measurement cell (so that the resulting oleate-SPION concentration in the cell was $0.07\ g\ l^{-1}$) and mixed for 5 min using a built-in magnetic stirrer and then left to stand for 20 min prior to the measurement. The obtained scattering curves were averages of 3 subsequent measurements, each of which took 10 s.

2.2.2. Wide-angle light scattering

The light scattering setup (ALV, Langen, Germany) for combined static and dynamic multiangle light scattering measurements consisted of a 22 mW He–Ne laser, operating at the wavelength, $\lambda = 632.8$ nm, an ALV CGS/8F goniometer, an ALV High QE APD detector and an ALV 5000/EPP multibit, multitau autocorrelator. The measurements were carried out at 25 °C at the oleate-SPION concentrations, $c_{NP} = 1\ g\ l^{-1}$ for DLS measurements and $0.07\ g\ l^{-1}$ (the same concentration as for SALS) for SLS measurements. The scattering angles, θ, ranging from 30° to 150°, corresponding to the scattering vector magnitudes, $q = (4\pi n_0/\lambda)\sin(\theta/2)$ (here n_0 is the refractive index of the solvent), from 6 to 25 μm^{-1}. DLS measurements were evaluated by fitting the measured normalized time autocorrelation function of the scattered light intensity, $g^{(2)}(t,q)$, related to the electric field autocorrelation function, $g^{(1)}(t,q)$, by the Siegert relation, $g^{(2)}(t,q) = 1 + \beta|g^{(1)}(t,q)|^2$. The data were fitted with the aid of the constrained regularization algorithm (CONTIN) which provides the distribution of relaxation times τ, $A(\tau,q)$, as the inverse Laplace transform of $g^{(1)}(t,q)$ function

$$g^{(1)}(t,q) = \int_0^\infty A(\tau,q)\ \exp\left(-\frac{t}{\tau}\right) d\tau. \quad (1)$$

2.2.3. Electrophoretic light scattering

ζ-Potential measurements were carried out with a Nano-ZS Zetasizer (Malvern Instruments, UK). ζ-Potential values were calculated from electrophoretic mobilities (average of three subsequent measurements, each of which consisted of 15–100 runs) using the Henry equation in the Smoluchowski approximation, $\mu = \varepsilon\zeta/\eta$, where μ is the electrophoretic mobility, η the solvent viscosity and ε is the dielectric constant of the solvent.

2.2.4. Transmission electron microscopy

Transmission electron microscopy (TEM) measurements were performed with a Tecnai G2 Spirit Twin microscope (FEI, Czech Republic), equipped with an energy-dispersive X-ray spectrometer (EDAX, NJ, USA). The samples were prepared as follows: 2 μl of the SPION dispersion ($c_{NP} = 1\ g\ l^{-1}$) was dropped onto a standard carbon-coated copper grid, left to equilibrate for 1 min at ambient temperature and then sucked off by touching the bottom of the grid with a thin strip of a filter paper. The sample was left to dry completely at ambient temperature and then characterized in a TEM microscope using bright-field imaging (TEM/BF), energy-dispersive analysis of X-rays (TEM/EDX) and selected-area electron diffraction (TEM/SAED). All experiments were carried out at the accelerating voltage of 120 kV. The SAED diffraction patterns were converted to one-dimensional diffractograms (using the ProcessDiffraction software [21]) and compared with the calculated powder diffraction patterns using the PowderCell software [22]); the calculation was based on the known crystal structures of magnetic iron oxides (maghemite (γ-Fe_2O_3) and magnetite (Fe_3O_4)), which were taken from Inorganic Crystal Structure Database [23].

2.2.5. Atomic force microscopy

AFM images under ambient conditions were recorded with an Asylum Cypher scanning probe microscope (Asylum Research, Santa Barbara, CA, USA) in the tapping mode using silicon cantilevers with a spring constant of 42 N/m. Scan sizes of 2 μm × 2 μm were used. Nanoparticles were deposited on a freshly peeled-out mica surface by a fast dip coating in a dilute ($c_{NP} = \sim 0.02\ g\ l^{-1}$) nanoparticles aqueous dispersion and dried in a vacuum oven. The analysis of the scans was performed using WSxM 5.0 Develop 7.0 software [24].

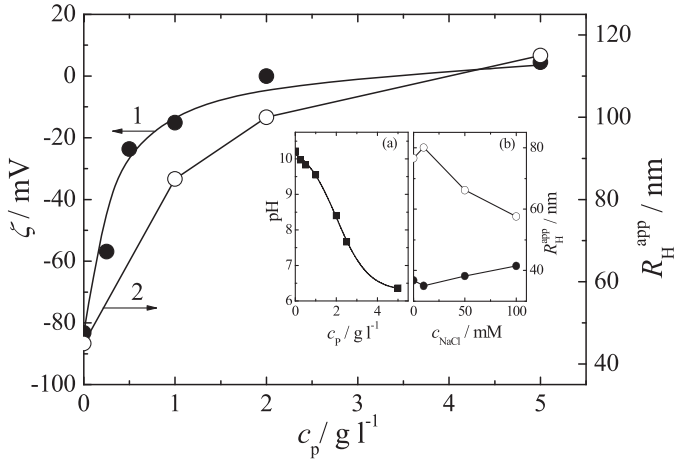

Fig. 1. ζ-Potential (curve 1) and apparent hydrodynamic radius, R_H^{app} (curve 2), of QNPHOS-PEO/oleate-SPION aggregates (SPION concentration, $c_{NP} = 1\ g\ l^{-1}$) as a function of the QNPHOS-PEO concentration, c_p. Inset: (a) pH of the dispersion as a function of c_p and (b) R_H^{app} as a function of the NaCl concentration, c_{NaCl}.

3. Results and discussion

3.1. Binding of QNPHOS-PEO copolymer to oleate-SPION

Interaction of oleate-SPION with the QNPHOS-PEO in aqueous dispersion was at first followed by electrophoretic light scattering measurements. Fig. 1 (curve 1) shows the ζ-potential of the QNPHOS-PEO/oleate-SPION system (the concentration of the oleate-SPION, $c_{NP} = 1\ g\ l^{-1}$) plotted against the concentration of QNPHOS-PEO, c_p. Since the scattering length of the SPION is much larger than that of the copolymer coils, scattering from the free QNPHOS-PEO is negligible even for the highest QNPHOS-PEO concentrations examined and the measured data reflect only the scattering from the coated SPION. However, the added QNPHOS-PEO is partitioned between the particles and the bulk dispersion as evident from the dropping value of the dispersion pH (inset a in Fig. 1) due to neutralization of OH^- ions by the acidic phenolic groups of QNPHOS.

The measured data show that QNPHOS-PEO binds to the nanoparticles and that the saturation corresponds to almost zero value of the ζ-potential ($\zeta_{sat} = \sim 5$ mV), which confirms that the stabilization of the QNPHOS-PEO/oleate-coated SPION is provided by the PEO blocks of the copolymer. The binding of QNPHOS-PEO to oleate-SPION can also be observed by the DLS measurement (Fig. 1, curve 2) which shows that the apparent hydrodynamic radius of the formed SPION clusters increases with the increasing copolymer concentration.

Inset b in Fig. 1 shows the apparent hydrodynamic radius of the clusters as a function of the concentration of the added sodium chloride. While in the case of oleate-SPION, R_H^{app} slightly increases with the increasing ionic strength due to the screening of the electrostatic repulsion between the oleate-coated nanoparticles which promotes the formation of the clusters, QNPHOS-PEO/oleate-SPION exhibit an opposite trend because the clusters are formed as a result of attractive electrostatic interactions between the oleate-SPION and the copolymer.

3.2. Characterization of SPION by TEM and AFM

TEM micrographs (Fig. 2a, b) of oleate-SPION and QNPHOS-PEO/oleate-SPION ($c_p/c_{NP} = 1$) show black nanoparticles on electron transparent carbon film. TEM/SAED diffraction patterns (Fig. 2c, d) confirm that the crystalline structure of the NP corresponds

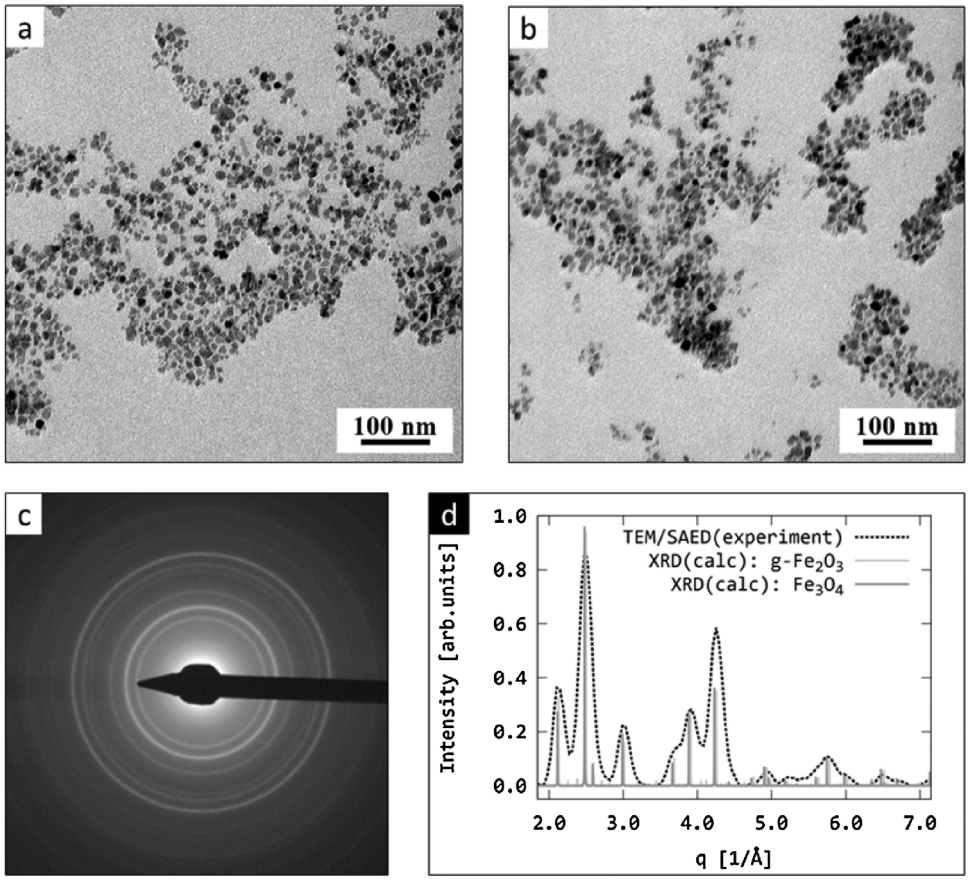

Fig. 2. TEM analysis of (a) oleate-NP and (b) QNPHOS-PEO/oleate-NP deposited from dispersions with (a) $c_{NP} = 1\ g\ l^{-1}$ and (b) $c_{NP} = 1\ g\ l^{-1}$, $c_P = 1\ g\ l^{-1}$; SAED diffraction patterns (c) confirmed that the observed nanoparticles have crystalline structure corresponding to magnetic iron oxides – magnetite and maghemite (d).

to that of magnetite/maghemite. Since the coating layers are not visible due to their low contrast as compared with iron oxide, the micrographs reveal only the bare SPION with the characteristic size of ~20 nm. In the case of QNPHOS-PEO/oleate-SPION, the clusters are more compact as compared with oleate-SPION suggesting that clustering is promoted by linking the oleate-SPION by QNPHOS blocks.

The AFM images (Fig. 3) reveal SPION clusters on the freshly cleaved mica surface. In the case of oleate-SPION (Fig. 3a, c), the deposited clusters are much larger (up to 300 nm) but more spread (the maximum height about 5 nm) and less compact as compared with QNPHOS-PEO/oleate-SPION (the cluster size up to 100 nm, the maximum height about 14 nm). The phase scans (Fig. 3c, d) show that the contrast between the hard iron oxide nanoparticles and the soft layers of the coating agent is more apparent in the case of oleate-SPION. This means that in the case of QNPHOS-PEO/oleate-SPION the coating layer is so thick that the hard bare iron oxide core of the nanoparticles cannot be detected.

3.3. Dynamic light scattering

Angular DLS measurements revealed a striking difference between the relaxation behavior of oleate-SPION and QNPHOS-PEO/oleate-SPION dispersions. While in the case of QNPHOS-PEO/oleate-SPION the DLS relaxation time distributions are monomodal (Fig. 4b) and the observed relaxation mode has diffusive character ($\tau \sim q^{-2}$) in the entire angular range of the measurement, in the case of oleate-SPION the distributions at low q ($\theta < 90^\circ$) consist of two modes (Fig. 4a), of which the faster one is diffusive, while the slower mode has the relaxation time proportional approximately to $q^{-3/2}$. At high q ($\theta > 90^\circ$), only the fast mode is observed with τ proportional to q^{-3} (Fig. 5a).

The $\tau \sim q^{-2}$ modes can be ascribed to the diffusion of SPION clusters and the mean dynamic correlation length of the diffusive mode, $\xi_D = kT\tau q^2/6\pi\eta$ (here k is the Boltzmann constant, T temperature and η the solvent viscosity), can be interpreted as the hydrodynamic radius of the clusters; R_H^{app} for $\theta = 90^\circ$ is plotted as function of c_p in Fig. 1 (curve 2). However, the presence of the slow $\tau \sim q^{-3/2}$ mode and the fast $\tau \sim q^{-3}$ mode suggests that the motions of the clusters are correlated and that the relaxation behavior is influenced by internal dynamics of larger aggregates. (The internal motion will dominate the relaxation behavior in the high q that reflects the dynamics at the shorter length scales.) Similar non-diffusive relaxation modes with $\tau \sim q^{-3}$ have been observed in DLS of polymer gels and interpreted as dynamics connected with structural rearrangement of clusters within the polymer network [25]. The same mechanism can be considered also in the case of magnetic nanoparticles that can form large aggregates which are flexible enough to allow for such rearrangement.

3.4. Small-angle light scattering

The presence of the non-diffusive DLS relaxation modes indicated the interactions between the SPION clusters suggesting that larger aggregates are formed with characteristic dimensions exceeding the length scales observable by the wide-angle LS measurement. Therefore we performed SALS measurements in order to obtain information about the size and structure of these aggregates.

As the aggregates are loose and have low refractive index increments with respect to the solvent, the structure of the dispersion

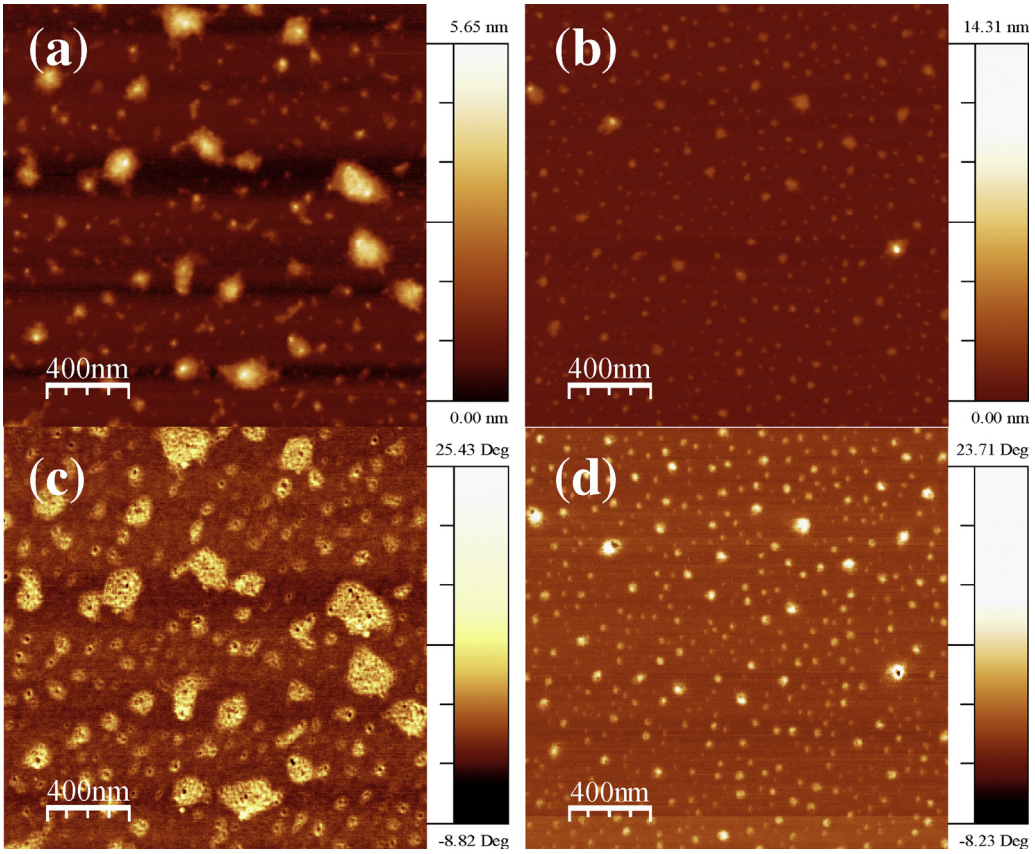

Fig. 3. AFM scans (a, b – height, c, d – phase) of (a, c) oleate-SPION and (b, d) QNPHOS-PEO/oleate-SPION deposited from dispersions with (a, c) $c_{NP} = 0.02\,g\,l^{-1}$ and (b, d) $c_{NP} = 0.02\,g\,l^{-1}$, $c_P = 0.02\,g\,l^{-1}$.

at very long length scales is strongly affected by convection of the solvent and other perturbations induced by the stirring process. Repeating the measurements at different stirring speeds has shown that the scattering behavior in the low q region ($q < 0.4\,\mu m^{-1}$) covering the length scale from 15 μm to 2 mm exhibits large fluctuations and depends on stirring speed while the shape of the scattering curve at q is reproducible and independent on whether the sample is stirred of left without stirring. For these reasons, only the high q part ($q > 0.4\,\mu m^{-1}$) of the scattering curves was taken into account for the analysis.

Since the size of the particles is negligible as compared with q^{-1} in the range studied by SALS measurements, the scattering function of the dispersion is fully described by the structure factor $S(q)$ resulting from the aggregation of the SPION. Assuming the exponential damping of the pair distance distribution function $g(r)$ and the mass-fractal structure of the aggregates, $g(r) \sim r^{D-3}\exp(-r/\xi)$,

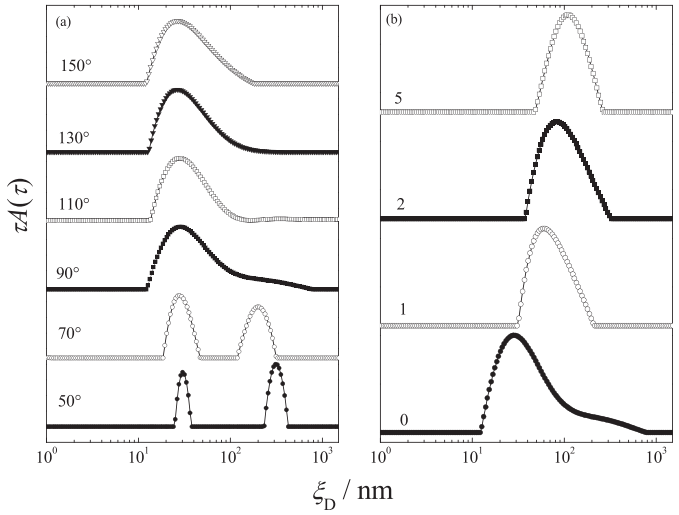

Fig. 4. DLS CONTIN distributions plotted against the dynamic correlation length, ξ_D, for (a) oleate-SPION dispersions at various scattering angles θ and (b) oleate-SPION and QNPHOS-PEO/oleate dispersions ($c_{NP} = 1\,g\,l^{-1}$) at $q = 90^{\circ}$ and various c_p (indicated above the curves in $g\,l^{-1}$).

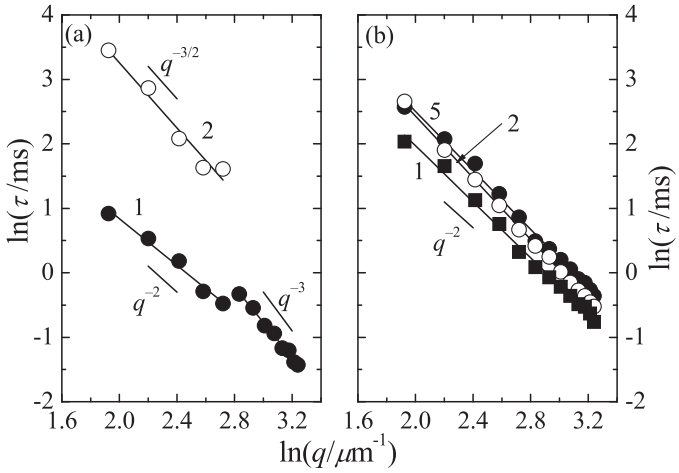

Fig. 5. Mean relaxation times of the modes observed in CONTIN distributions of (a) oleate-SPION dispersions ($c_{NP} = 1\,g\,l^{-1}$): curve 1 – fast mode, curve 2 – slow mode and (b) QNPHOS-PEO/oleate dispersions ($c_{NP} = 1\,g\,l^{-1}$) at various c_p (indicated above the curves in $g\,l^{-1}$).

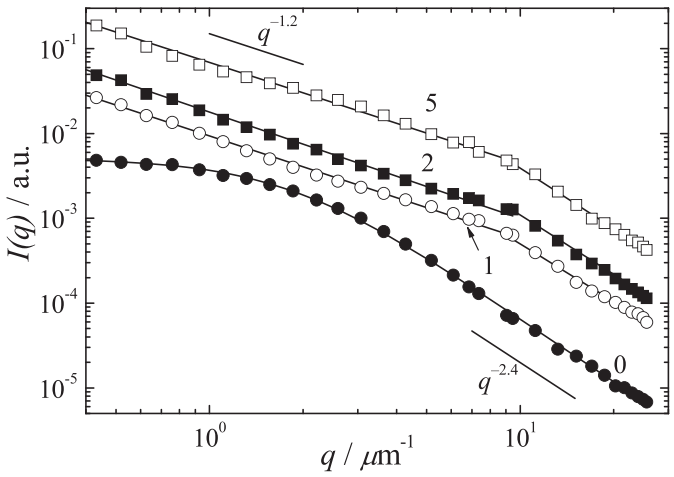

Fig. 6. Combined SALS/SLS curves for QNPHOS-PEO/oleate-SPION dispersions, $c_p = 0.07\ g\ l^{-1}$. The c_p/c_{NP} ratios are indicated at the curves.

where D is the mass fractal dimension and ξ is the cut-off length, the corresponding structure factor is given by the formula [26]

$$S(q) = \frac{\sin[(D-1)\arctan(\xi q)]}{(D-1)\xi q(1+\xi^2 q^2)^{(D-1)/2}}. \quad (2)$$

The gyration radius of the aggregate, R_g, can be calculated from the cut-off length as

$$R_g^2 = \frac{(D+1)D}{2}\xi^2 \quad (3)$$

Fig. 6 shows combined SALS (0.4–9 μm^{-1}) and SLS (6–25 μm^{-1}) scattering curves of oleate-SPION and QNPHOS-PEO/oleate-SPION for various c_p. The scattering behavior of oleate-SPION can be described by Eq. (2); the fit provides the values of the gyration radius and the fractal dimension, $R_g = \sim 1.1\ \mu m$ and $D = 2.4$. In the case of QNPHOS-PEO/oleate-SPION, the scattering behavior is markedly different: in the high q region above 8 μm^{-1}, the scattering curves fall with the exponent about −2.3, similar to that of oleate-SPION aggregates. In the q range from 0.4 to 9 μm^{-1}, the exponent drops to about −1.2 and the scattering curve does not level off. This result indicates that the power-law regime in the region from 9 to 25 μm^{-1} reflects the internal structure of the compact clusters that arrange into chainlike aggregates as seen from the scattering behavior at low q. The aggregates are so large that their Guinier regime is not accessible and the measurements show only the high-q power law limit of the structure factor, $S(q) \sim q^{-D}$.

While the mass fractal dimension of oleate-SPION aggregates is in accordance with the values for reaction limited cluster–cluster aggregation (RLCA) regime with respect to repulsive electrostatic interactions between the oleate-coated SPION, the fractal dimension of QNPHOS-PEO/oleate-SPION is much lower than the theoretical value for the diffusion-limited cluster–cluster aggregation (DLCA; $D = \sim 1.7$) that should be expected in the absence of repulsive interactions between the particles [27]. Comparable fractal dimensions were reported for surfactant-stabilized SPION aqueous dispersions (at concentrations slightly ca. 10 times lower than those examined in our study) and explained as a result of weak anisotropic attractive interactions between the small SPION clusters forming the aggregate [10]. In our case, the presence of small clusters with the compact internal structure is evidenced both by the static light scattering at high q and by the results of dynamic light scattering which both indicate that the formation of small SPION clusters.

4. Conclusions

We have studied the structure and dynamics of aggregates formed in aqueous dispersions of superparamagnetic iron oxide nanoparticles (SPION) coated (i) by a bilayer of oleate (oleate-SPION) and (ii) by an additional layer of the double hydrophilic cationic block polyelectrolyte QNPHOS-PEO adsorbed at the negatively charged surface of oleate-SPION (QNPHOS-PEO/oleate-SPION). The study showed that despite the coating by QNPHOS-PEO rather promotes the formation of clusters at the length scales of the order of 10^2 nm as observed by TEM and AFM, the structure of QNPHOS-PEO/oleate-SPION aggregates at the micrometer length scale is much looser as compared with oleate-SPION which is indicated by their fractal dimension obtained by SALS measurements (2.4 for oleate-SPION, 1.2 for QNPHOS-PEO/oleate-SPION). The results demonstrate that the coating of SPION by QNPHOS-PEO (and possibly by other DHBP) prevents the isotropic Van der Waals attraction among the coated SPION. This allows for magnetic dipolar interaction between the SPION clusters to dominate which leads to the formation of elongated aggregates of SPION. In conclusion, our results show that tuning the interactions among SPION by the choice of the coating agent can influence the structure of large aggregates they form on micrometer length scales.

Acknowledgments

The authors acknowledge the support from the Czech Science Foundation (Grant No. 14-11516S). Electron microscopy at the Institute of Macromolecular Chemistry was supported through Technology Agency of the Czech Republic Grant TE01020118.

References

[1] H.E. Horng, C.-Y. Hong, S.Y. Yang, H.C. Yang, Novel properties and applications in magnetic fluids, J. Phys. Chem. Solids 62 (2001) 1749–1764.
[2] C. Scherer, A.M. Figueiredo Neto, Ferrofluids: properties and applications, Braz. J. Phys. 35 (2005) 718–728.
[3] A. Joseph, S. Mathew, Ferrofluids: synthetic strategies, stabilization, physicochemical features, characterization, and applications, ChemPlusChem 79 (2014) 1382–1420.
[4] B.J. Park, F.F. Fang, H.J. Choi, Magnetorheology: materials and application, Soft Matter 6 (2010) 5246–5253.
[5] A. Jordan, R. Scholz, P. Wust, H. Fahling, R. Felix, Magnetic fluid hyperthermia (MFH): cancer treatment with AC magnetic field induced excitation of biocompatible superparamagnetic nanoparticles, J. Magn. Magn. Mater. 201 (1999) 413–419.
[6] S. Mornet, S. Vasseur, F. Grasset, E. Duguet, Magnetic nanoparticle design for medical diagnosis and therapy, J. Mater. Chem. 14 (2004) 2161–2175.
[7] O. Veiseh, J.W. Gunn, M. Zhang, Design and fabrication of magnetic nanoparticles for targeted drug delivery and imaging, Adv. Drug Deliv. Rev. 62 (2010) 284–304.
[8] B.I. Kharisov, H.V. Rasika Dias, O.V. Kharissova, A. Vásquez, Y. Peña, I. Gómez, Solubilization, dispersion and stabilization of magnetic nanoparticles in water and non-aqueous solvents: recent trends, RSC Adv. 4 (2014) 45354–45381.
[9] A.K. Gupta, M. Gupta, Synthesis and surface engineering of iron oxide nanoparticles for biomedical applications, Biomaterials 26 (2005) 3995–4021.
[10] L.F. Shen, A. Stachowiak, S.E.K. Fateen, P.E. Laibinis, T.A. Hatton, Structure of alkanoic acid stabilized magnetic fluids. A small-angle neutron and light scattering analysis, Langmuir 17 (2001) 288–299.
[11] B.H. Pettersen, T. Skodvin, J. Sjöblom, Sedimentation of monodisperse magnetic particles as studied by means of time-domain dielectric spectroscopy, Colloids Surf. A: Physicochem. Eng. Aspects 143 (1998) 323–330.
[12] M. Yan, J. Fresnais, J.-F. Berret, Growth mechanism of nanostructured superparamagnetic rods obtained by electrostatic co-assembly, Soft Matter 6 (2010) 1997–2005.
[13] S.L. Saville, R.C. Woodward, M.J. House, A. Tokarev, J. Hammers, B. Qi, J. Shaw, M. Saunders, R.R. Varsani, T.G. St Pierre, O.T. Mefford, The effect of magnetically induced linear aggregates on proton transverse relaxation rates of aqueous suspensions of polymer coated magnetic nanoparticles, Nanoscale 5 (2013) 2152–2163.
[14] Y. Xu, J. Yuan, B. Fang, M. Drechsler, M. Müllner, S. Bolisetty, M. Ballauff, A.H.E. Müller, Hybrids of magnetic nanoparticles with double-hydrophilic core/shell cylindrical polymer brushes and their alignment in a magnetic field, Adv. Funct. Mater. 20 (2010) 4182–4189.

[15] M. Hod, C. Dobbrow, M. Vaidyanathan, D. Guin, L. Belkoura, R. Strey, M. Gottlieb, A.M. Schmidt, Controlling the self-assembly of magnetic nanoparticles by competing dipolar and isotropic particle interactions, J. Colloid Interface Sci. 436 (2014) 83–89.
[16] J.-F. Berret, A. Sehgal, M. Morvan, O. Sandre, A. Vacher, M. Airiau, Stable oxide nanoparticle clusters obtained by complexation, J. Colloid Interface Sci. 303 (2006) 315–318.
[17] B. Frka-Petesic, J. Fresnais, J.-F. Berret, V. Dupuis, R. Perzynski, O. Sandre, Stabilization and controlled association of superparamagnetic nanoparticles using block copolymers, J. Magn. Magn. Mater. 321 (2009) 667–670.
[18] C. Pichot, Reactive nanocolloids for nanotechnologies and microsystems, in: A. Elaissary (Ed.), Colloidal Nanoparticles in Biotechnology, Wiley, 2008, pp. 1–30.
[19] G. Mountrichas, S. Pispas, Novel double hydrophilic block copolymers based on poly(p-hydroxystyrene) derivatives and poly(ethylene oxide), J. Polym. Sci. A: Polym. Chem. 45 (2007) 5790–5799.
[20] M. Štěpánek, P. Matějíček, K. Procházka, S.K. Filippov, B. Angelov, M. Šlouf, G. Mountrichas, S. Pispas, Polyelectrolyte-surfactant complexes formed by poly-[3,5-bis(trimethylammoniummethyl)4-hydroxystyrene iodide]-block-poly(ethylene oxide) and sodium dodecyl sulfate in aqueous solutions, Langmuir 27 (2011) 5275–5281.
[21] J.L. Lábár, Consistent indexing of a (set of) SAED pattern(s) with the ProcessDiffraction program, Ultramicroscopy 103 (2005) 237–249.
[22] W. Kraus, G. Nolze, POWDER CELL – a program for the representation and manipulation of crystal structures and calculation of the resulting X-ray powder patterns, J. Appl. Crystallogr. 29 (1996) 301–303.
[23] www.fiz-karlsruhe.de/icsd.html
[24] www.wsxmsolutions.com
[25] M.C. Blanco, D. Leisner, C. Vázquez, M.A. López-Quintela, Dynamic light scattering in transient reversible gels, Langmuir 16 (2000) 8585–8594.
[26] C.M. Sørensen, J. Cai, N. Lu, Test of static structure factors for describing light scattering from fractal soot aggregates, Langmuir 8 (1992) 2064–2069.
[27] J. Liu, W.I. Shih, M. Sarikaya, I.A. Aksay, Fractal colloidal aggregates with finite interparticle interactions: energy dependence of the fractal dimension, Phys. Rev. A 41 (1990) 3206–3213.

European Polymer Journal 73 (2015) 212–221

Contents lists available at ScienceDirect

European Polymer Journal

journal homepage: www.elsevier.com/locate/europolj

Self- and co-assembly of amphiphilic gradient polyelectrolyte in aqueous solution: Interaction with oppositely charged ionic surfactant

Mariusz Uchman [a,*], Jana Hajduová [a], Eleni Vlassi [b], Stergios Pispas [b], Marie-Sousai Appavou [c], Miroslav Štěpánek [a,*]

[a] Department of Physical and Macromolecular Chemistry, Faculty of Science, Charles University in Prague, Hlavova 2030, 12840 Prague 2, Czech Republic
[b] Theoretical & Physical Chemistry Institute, National Hellenic Research Foundation, 48 Vassileos Constantinou Ave., 11635 Athens, Greece
[c] Forschungszentrum Jülich GmbH, IFF-JCNS, Lichtenbergerstraße 1, D-85747 Garching, Germany

ARTICLE INFO

Article history:
Received 20 July 2015
Received in revised form 18 September 2015
Accepted 10 October 2015
Available online 22 October 2015

Keywords:
Gradient copolymer
Poly(oxazoline)
SANS
Polyelectrolyte surfactant complexes

ABSTRACT

Association behavior of the biocompatible amphiphilic cationic gradient polyelectrolyte poly[(2-methyl-2-oxazoline)-*grad*-(2-phenyl-2-oxazoline)-*mod*-(ethylene imine)] (HPPhMeOx) prepared by partial hydrolysis of the gradient copolymer poly[(2-methyl-2-oxazoline)-*grad*-(2-phenyl-2-oxazoline)] and the interaction of HPPhMeOx with the anionic surfactant sodium dodecyl sulfate (SDS) in aqueous solutions were investigated by scattering techniques (SANS, DLS) and by atomic force microscopy. SANS measurements revealed that large particles with the hydrodynamic radius of ca. 500 nm observed in HPPhMeOx aqueous solutions by DLS are formed by a network of physically crosslinked compact hydrophobic domains with the mean radius of ca. 10 nm. Upon addition of sodium dodecyl sulfate (SDS), the size of the domains increases at low amounts of the added SDS due to hydrophobic interaction of the single surfactant ions with the aggregates. Further addition of SDS leads to the formation of the co-assembled polyelectrolyte–surfactant complex manifested in SANS by the presence of the correlation peak from the densely packed SDS micelles as well as by partial disruption of the domains.

1. Introduction

Block copolymers (BC) have been a subject of numerous studies in connection with their ability to form self-assembled core–shell nanoparticles in selective solvents, such as micelles or vesicles, with the core formed by the collapsed insoluble blocks and the shell (also referred to as corona) of soluble blocks swollen by the solvent [1–3]. Amphiphilic BC nanoparticles have been extensively investigated as potential vessels for the controlled release and delivery of hydrophobic drugs [4,5].

In contrast to block copolymers, much less attention has been paid so far to the association behavior of gradient copolymers (GC) in selective solvents [6–10]. In the case of an amphiphilic GC, instead of micelles which possess a well-defined core–shell structure with segregated blocks, one can expect the formation of particles in which the GC chain ends rich in the hydrophobic units will assemble in the inner parts of the associate, and the shell rich in the hydrophilic units in the outer part. The structure of such particles resembles that of block copolymer micelles with no sharp interface between the core and the shell.

* Corresponding authors.
E-mail addresses: uchman@natur.cuni.cz (M. Uchman), stepanek@natur.cuni.cz (M. Štěpánek).

http://dx.doi.org/10.1016/j.eurpolymj.2015.10.015
0014-3057/

The self-assembly behavior of amphiphilic GC in aqueous solutions depends both on the solvent interaction parameters of the monomeric units in the GC chain and on the steepness of the gradient. It has been reported that the presence of poly (acrylic acid) (PAA) hydrophilic units in the polystyrene (PS) core of PAA-*b*-(PAA-*grad*-PS) micelles causes the swelling of the core with water and makes the core softer so that the micelles are in dynamic equilibrium with the unimers although micelles of the BC counterpart of this copolymer, PAA-*b*-PS, are kinetically frozen [11,12].

On the other hand, the shell of the amphiphilic GC micelles has partly hydrophobic character due to the presence of hydrophobic units. This may lead to secondary association of the micelles into larger aggregates and to the formation of physical network [11,12].

Here we focus on the amphiphilic cationic gradient polyelectrolyte poly[(2-methyl-2-oxazoline)-*grad*-(2-phenyl-2-oxazoline)-*mod*-(ethylene imine)] (HPPhMeOx) [13] prepared by partial hydrolysis of the gradient copolymer poly(2-methyl-2-oxazoline)-*grad*-poly(2-phenyl-2-oxazoline) (PPhMeOx) [14,15]. Derivatives of poly(2-oxazoline)s have proved to be promising polymers for biomedical applications due to their biocompatibility and tunable hydrophobicity [16,17] (some of them exhibiting the critical solution temperature behavior in water and alcohols) [18,19]. The partial hydrolysis of 2-methyl-2-oxazoline and 2-phenyl-2-oxazoline to ethylene imine units converts the PPhMeOx copolymer to biocompatible amphiphilic cationic polyelectrolyte HPPhMeOx, the structure of which mimics a positively charged protein with hydrophobic and hydrophilic domains. It was reported that HPPhMeOx formed electrostatically stabilized complexes with DNA [13].

In this article, we focus on electrostatic coassembly behavior of HPPhMeOx and report on the formation of the polyelectrolyte–surfactant complexes (PE–S) of HPPhMeOx with sodium dodecyl sulfate (SDS) in aqueous solutions. PE–S have attracted attention of many researchers in the past two decades due to general interest in nanostructured self-assembled systems, as well as due to applications of these systems [20–22]. It has been found that the oppositely charged surfactant condenses on the polyelectrolyte chains and forms micelles at concentrations below the critical micelle concentration (cmc) of the surfactant [23] and that water-insoluble stoichiometric PE–S with zero net charge form various water-insoluble ordered crystalline-like phases [24]. While there are a number of papers about co-assembly of block copolymers consisting of a neutral block and a polyelectrolyte block (so-called double hydrophilic block polyelectrolytes, DHBP) with oppositely-charged surfactants in core–shell particles [25–27], the interaction of the hydrophobic–hydrophilic gradient polyelectrolyte with oppositely charged surfactant has not yet been studied so far.

In this study, we use both scattering techniques (static and dynamic light scattering, SANS) and atomic force microscopy to investigate structure of HPPhMeOx and HPPhMeOx/SDS aggregates in aqueous solutions.

2. Experimental

2.1. Materials

HPPhMeOx (Fig. 1) was prepared by partial hydrolysis of the precursor gradient copolymer PPhMeOx synthesized by ring opening cationic polymerization according to the procedure described in Ref. [14]. PPhMeOx (1 g) was then dissolved in 16 ml of ethanol, 6.2 ml of 37% HCl were added to the solution and the reaction mixture was left to stand for 3 h. After hydrolysis, the mixture was cooled in an ice bath and the pH was adjusted to 3 using NaOH solution and dialyzed against deionized water. The resulting HPPhMeOx copolymer was isolated using a rotary evaporator and further dried in a vacuum oven. The number-averaged molar mass of HPPhMeOx according to a SEC analysis of the precursor was, M_n = 3400 g mol^{-1}, taking into account the mass composition according to ^{1}H NMR, which was 39, 37 and 24 wt.% of ethylene imine, 2-methyloxazoline and 2-phenyloxazoline units, respectively [13].

2.2. Preparation of samples

For light scattering and AFM measurements, 10 mg of HPPhMeOx copolymer were dissolved in 10 ml of deionized water. The pH and conductivity of the resulting 1 mg/ml solution were 3.5 and 0.8 mS cm^{-1}, respectively, which correspond to the

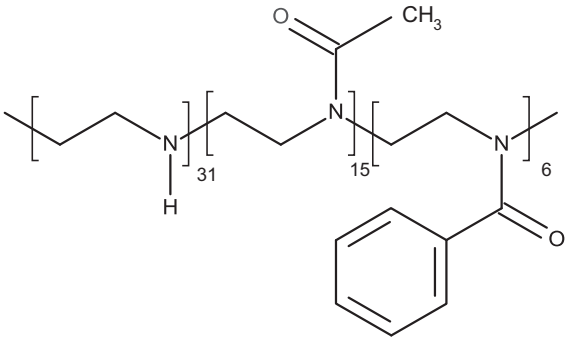

Fig. 1. Structure of HPPhMeOx copolymer.

ionic strength of ca. 10^{-2} M assuming the contribution of H^+, Cl^- and Na^+ ions to the conductivity of the solution. 1 ml portions of the 1 mg/ml HPPhMeOx solution (concentration of ethylene imine units, c_{NH} = 9.1 mmol/l) were mixed with the corresponding amounts of 0.1 M aqueous stock solution of sodium dodecyl sulfate and left to equilibrate overnight prior to the measurements. The same protocol was used for the preparation of samples for SANS, except that D_2O was used as a solvent.

2.3. Light scattering

The light scattering setup (ALV, Langen, Germany) consisted of a 22 mW He–Ne laser, operating at the wavelength, λ = 632.8 nm, an ALV CGS/8F goniometer, an ALV High QE APD detector and an ALV 5000/EPP multibit, multitau autocorrelator. The measurements were carried out at 25 °C and the scattering angle θ = 90°, corresponding to the scattering vector magnitude, $q = (4\pi n_0/\lambda)\sin(\theta/2)$=18.7 μm^{-1} (here n_0 is the refractive index of the solvent). The measured scattering intensities were converted to Rayleigh ratios using the calibration by toluene standard. DLS measurements were evaluated by fitting the measured normalized time autocorrelation function of the scattered light intensity, $g^{(2)}(t,q)$, related to the electric field autocorrelation function, $g^{(1)}(t,q)$, by the Siegert relation, $g^{(2)}(t,q) = 1 + \beta|g^{(1)}(t,q)|^2$. The data were fitted with the aid of the constrained regularization algorithm (CONTIN) which provides the distribution of relaxation times τ, $A(\tau,q)$, as the inverse Laplace transform of $g^{(1)}(t,q)$ function

$$g^{(1)}(t,q) = \int_0^\infty A(\tau,q)\exp\left(-\frac{t}{\tau}\right)\mathrm{d}\tau \quad (1)$$

The $A(\tau)$ distributions were recalculated to the distributions of apparent hydrodynamic radii, R_H^{app}, assuming the apparent diffusion coefficient $D_{app} = 1/\tau q^2$ and using the Stokes–Einstein formula, $R_H^{app} = k_B T/6\pi\eta D_{app}$, where k_B is the Boltzmann constant, T the temperature and η the solvent viscosity.

Electrophoretic mobility and conductivity measurements were carried out with a Nano-ZS Zetasizer (Malvern Instruments, UK). The obtained values were averages of three subsequent measurements, each of which consisted of 15–100 runs).

2.4. Small angle neutron scattering

SANS experiments were carried out on KWS-2 from the Jülich Center for Neutron Science (JCNS) at MLZ (FRM-II) in Garching, Germany [28]. Samples were poured in quartz cuvettes (QX quality from Hellma) of 2 mm neutron pathway, thermostatted at 25.0 °C. Three configurations were used with SD = 1.7 m, λ = 0.45 nm, SD = 7.7 m, λ = 0.45 nm and SD = 7.7 m, λ = 1.2 nm, where SD is the sample-to-detector distance and λ the mean wavelength (FWHM = 20%); the final q-range obtained is 0.025–3.2 nm^{-1}, corresponding to 2–250 nm in the real space (using Bragg's law $d = 2\pi/q$). The beam was collimated at 8 m from the sample in all cases. The beam size at the sample position was 8 × 8 mm^2. Data reduction was performed on 2D patterns by means of BerSANS software [29] using the scattering by a 1.5 mm PMMA sheet to correct for pixel efficiency, taking a tabulated value for the absolute scale, and subtracting the experimental intensity for the buffer as background. Data were radially averaged and scattering curves from the 3 configurations were merged with no need for any arbitrary coefficient. The curves were fitted using SASFit 0.93.2 software [30].

2.5. Atomic force microscopy

AFM images under ambient conditions were recorded with an Asylum Cypher scanning probe microscope (Asylum Research, Santa Barbara, CA, USA) in the tapping mode using silicon cantilevers with a spring constant of 42 N m^{-1}. Scan sizes of 2 × 2 μm^2 were used. Samples were prepared by a fast dip coating of a freshly cleaved sheet of mica surface in a dilute solution of HPPhMeOx/SDS mixtures (copolymer concentration, c_P = 0.02 g l^{-1}) nanoparticles aqueous dispersion and dried in a vacuum oven. The analysis of the scans was performed using WSxM 5.0 Develop 7.0 software [31].

3. Results and discussion

3.1. Structure of HPPhMeOx aggregates in aqueous solutions

The previous study on HPPhMeOx copolymer complexes with DNA [13] revealed that HPPhMeOx undergoes aggregation in aqueous solutions at pH 7. Our results confirm that observation even in acidic solutions (pH 3) at the conditions of the full protonation of the ethylene imine units. Dynamic LS data indicate that HPPhMeOx is not molecularly soluble and forms large, weakly scattering aggregates with the mean apparent hydrodynamic radius of ca. 500 nm.

Since the size of the aggregates exceeds the contour length of the HPPhMeOx chain, the aggregates cannot have a simple core/shell structure. Instead, one could expect the formation of a physical network of HPPhMeOx chains interconnected by domains formed by associated hydrophobic PPhOx units. In order to probe the internal structure of the aggregates and to verify this assumption, we performed a small-angle neutron scattering measurement.

The SANS curve of the HPPhMeOx solution in D_2O is shown in Fig. 2. The curve exhibits the distinct Guinier regime with the gyration radius of 10 nm (the fit is shown in Fig. 2 as the dashed curve). This behavior is in accordance with the

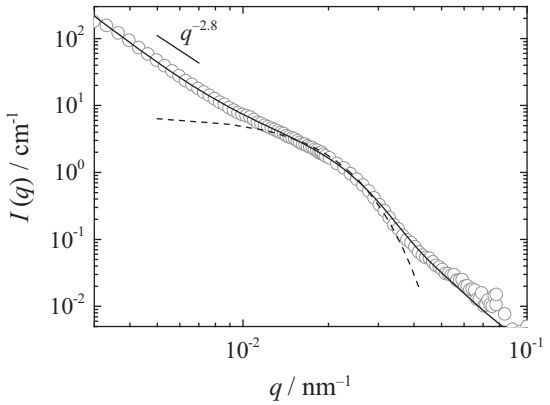

Fig. 2. SANS curve of acidic HPPhMeOx solution (HPPhMeOx concentration, c = 1 mg ml^{-1}) in D_2O (open circles), the fit of the curve by Eq. (2) (solid line) and the fit of the Guinier region of the curve by the Guinier equation (dashed line).

Table 1
Parameters of the fit of the SANS curve of acidic HPPhMeOx solution in D_2O by Eq. (2).

R_0, nm	σ, nm	D	r_0, nm
7.0 ± 0.9	3.2 ± 0.4	2.79 ± 0.01	10.7 ± 0.5

assumption that the aggregates contain compact domains. Taking the suggested structure into account, the Guinier regime, the R_g of which can be interpreted as the characteristic radius of the domains, separates the high q region of the curves corresponding to the internal structure of the domains and their junctions from the low q region which reflects the interdomain interference within the aggregate.

In order to treat this structural model more carefully, we fitted the scattering curve to the following model: (i) The interconnected domains were treated by the form factor $P_{sph}(q)$ of polydisperse spheres with the Gaussian distribution of the sphere radii. (ii) The interactions among the domains were described by the mass fractal structure factor $S_{fract}(q)$ with the exponential cut-off of the pair correlation function. The scattering intensity is then given by the relationship

$$I(q) = N(\Delta b)^2 S_{fract}(q) P_{sph}(q) + I_b \tag{2}$$

where Δb and N, respectively, are the excess scattering length and the number density of the domains and I_b is the background scattering. The form factor $P_{sph}(q)$ is given by the formula

$$P_{sph}(q) = \int_0^\infty \frac{\exp\left(-\frac{(R-R_0)^2}{2\sigma^2}\right)\left[3\frac{\sin(qR)-qR\cos(qR)}{q^3R^3}\right]^2}{\sqrt{\frac{\pi}{2}}\sigma\left[1+\mathrm{erf}\left(\frac{R}{\sqrt{2}\sigma}\right)\right]} R^6 \mathrm{d}R \tag{3}$$

where R_0 is the center and σ is the width of the distribution. The structure factor reads [32]

$$S_{fract}(q) = 1 + \frac{D\Gamma(D-1)\sin([D-1]\arctan(q\xi))}{(qr_0)^D\left[1+q^{-2}\xi^{-2}\right]^{(D-1)/2}} \tag{4}$$

where D is the mass fractal dimension of the aggregate, ξ is the cut-off length, and r_0 is the characteristic size of the particles forming the fractal aggregate.

The fit is shown in Fig. 2 as the solid curve. With the exception of the high q regime reflecting both the internal structure of the domains and the connections among the domains which are not treated properly by the used model, the Eq. (2) fits the experimental data satisfactorily. The results of the fit are listed in Table 1. Since the curve does not level off in the low q region, the cut-off length cannot be determined reliably (the fit provides the value larger than 100 nm). The mass fractal dimension close to 3 indicates a dense structure of aggregate at the lengthscale of the tens of nm.

3.2. Formation of PE–S complexes of HPPhMeOx with SDS

Mixing the acidic aqueous HPPhMeOx solution with a certain critical amount of SDS causes the formation of highly turbid dispersions, which become transparent again after further addition of the surfactant. This behavior indicates the formation of the HPPhMeOx/SDS complex and its aggregation as a result of decreased solubility of the complex.

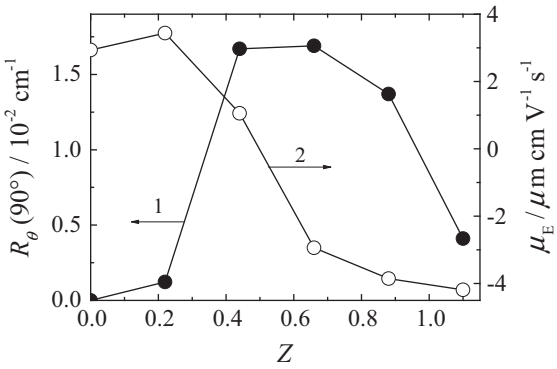

Fig. 3. Rayleigh ratio at the scattering angle $\theta = 90°$ and electrophoretic mobility of HPPhMeOx/SDS dispersions (HPPhMeOx concentration, $c = 1$ mg ml^{-1}) as function of charge ratios Z.

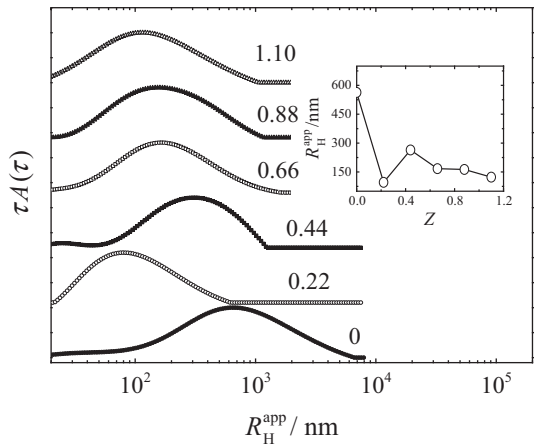

Fig. 4. DLS CONTIN distributions of apparent hydrodynamic radii of HPPhMeOx and HPPhMeOx/SDS aggregates (HPPhMeOx concentration, $c = 1$ mg ml^{-1}) at the scattering angle $\theta = 90°$. Charge ratios Z are indicated above the curves. Insert: The mean apparent hydrodynamic radius of the aggregates as a function of Z.

Fig. 3 shows the light scattering intensity at $\theta = 90°$ (curve 1) and the electrophoretic mobility, μ_E, of the HPPhMeOx/SDS complex (curve 2) as functions of the charge ratio Z, defined as the molar ratio of the amount of dodecyl sulfate anions to the amount of ethylene imine units. The strongly scattering aggregates are formed in the Z region from 0.4 to 0.8. The aggregates with the low μ_E (that is, with the low surface charge) close to $Z = 0.4$ are very unstable and the phase separation of the complex occurs within a few days after mixing.

While the lower Z limit for the formation of the aggregates is caused by the fact that SDS must reach the critical aggregation concentration in order to bind cooperatively on HPPhMeOx chains [23] and form the complex, the disruption of the aggregates at high Z is probably connected with the destabilization of hydrophobic domains in the aggregate. It should be pointed out that disruption of various coassembled systems by adding ionic surfactants that bind stronger to one of the components of the coassembly was reported in the literature [33].

Fig. 4 shows the CONTIN distributions of apparent hydrodynamic radii of HPPhMeOx and HPPhMeOx/SDS aggregates obtained by DLS measurements at the scattering angle $\theta = 90°$. All the distributions are very broad indicating that the aggregates are polydisperse. The size of the aggregates strongly decreases after adding the surfactant as a result of screening the electrostatic repulsion between the HPPhMeOx chains and the formation of the HPPhMeOx/SDS complex.

Fig. 5 shows SANS curves of HPPhMeOx and HPPhMeOx/SDS dispersions (for Z ratios 0.22, 0.66 and 0.88) in D_2O. As in the case of HPPhMeOx aggregates, the scattering curves of HPPhMeOx/SDS complexes reveal a distinct Guinier regime indicating the presence of compact domains. The apparent gyration radius, R_g, and the apparent forward scattering intensity, $I(0)$ obtained from the fit of the Guinier regions of the curves are shown in Fig. 6 as functions of Z. The fact that both R_g and $I(0)$ dependences on Z pass the maximum at $Z = 0.22$ can be explained by the different mechanisms SDS interacts with HPPhMeOx below and above the critical aggregation concentration (cac) of the surfactant. Below the cac, DS ions are sorbed preferentially into hydrophobic domains and cause the substantial growth of their size. On the other hand, after the cac of SDS is reached and the PE-S complex is formed, the size of the domains decreases because the major part of the HPPhMeOx

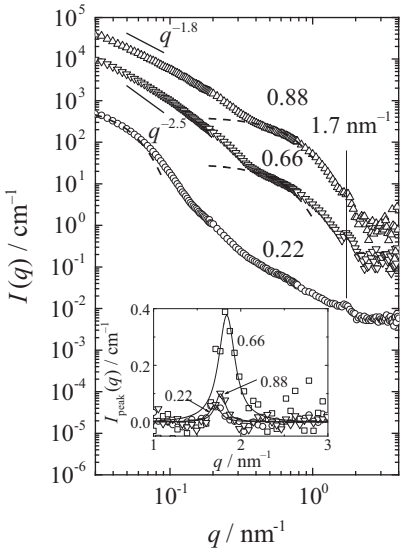

Fig. 5. SANS curves of HPPhMeOx/SDS dispersions (HPPhMeOx concentration, c = 1 mg ml^{-1}) in D_2O at various charge ratios Z (indicated above the curves) and the fits of the Guinier regions of the curves by the Guinier equation (dashed lines). For clarity, the curves and fits are shifted by a multiplicative factor of 20. Insert: Correlation peaks of the SANS curves and their fits by the Eq. (4) (solid lines).

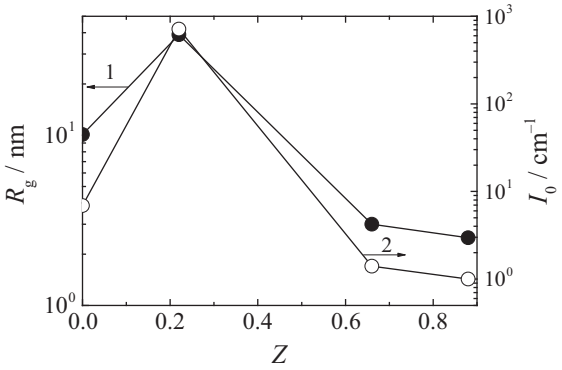

Fig. 6. Parameters of the fits of the Guinier regions of the SANS curves by the Guinier equation, as functions of the charge ratio Z.

chain is bound to the complex. (At Z > 0.9, the further disruption of the domains leads to the disruption of the aggregates as indicated by light scattering measurements.)

The latter explanation is supported by the presence of the correlation peak with the maximum, q_{max} = ~1.75 nm^{-1} in the SANS curves of the aggregates formed by HPPhMeOx/SDS complexes (Fig. 5). This behavior is typical for polyelectrolyte–surfactant complexes and is indicative of the presence of densely packed surfactant micelles in the complex [24,26,27]. The Bragg length corresponding to the peak position, $\lambda = 2\pi/q_{max}$ = 3.6 nm, corresponds to the distance between the neighboring packed SDS micelles. The correlations among the densely packed surfactant micelles in the polyelectrolyte surfactant complex were treated by the structure factor for disordered cell–cell correlations [34]. The scattering curves in the high-q region from 1 to 3 nm^{-1} were fitted by the equation $I(q) = I_{peak}(q) + C_p q^{\alpha} + I_b$, where I_b is the background scattering, C_p is the preexponential factor of the power law scattering contribution with the power law exponent α, and $I_{peak}(q)$ is the Lorentzian function

$$I_{peak}(q) = \frac{I_0 \xi_{cor}^{-2}}{\xi_{cor}^{-2} + \left(q - 2\pi l^{-1}\right)^2} \tag{5}$$

where I_0 is the amplitude, l is the distance between the micelles and ξ_{cor} is the correlation length. The correlation peaks and the fits by Eq. (5) are shown in Fig. 5 as insert. The correlation length ξ_{cor} is independent on Z and is ca. 10 nm. For the aggregates with Z = 0.66, the amplitude of the correlation peak reaches the maximum value. The decrease of the amplitude at higher Z is caused by the decrease of the amount of clusters of densely packed micelles in the aggregates due to their disruption.

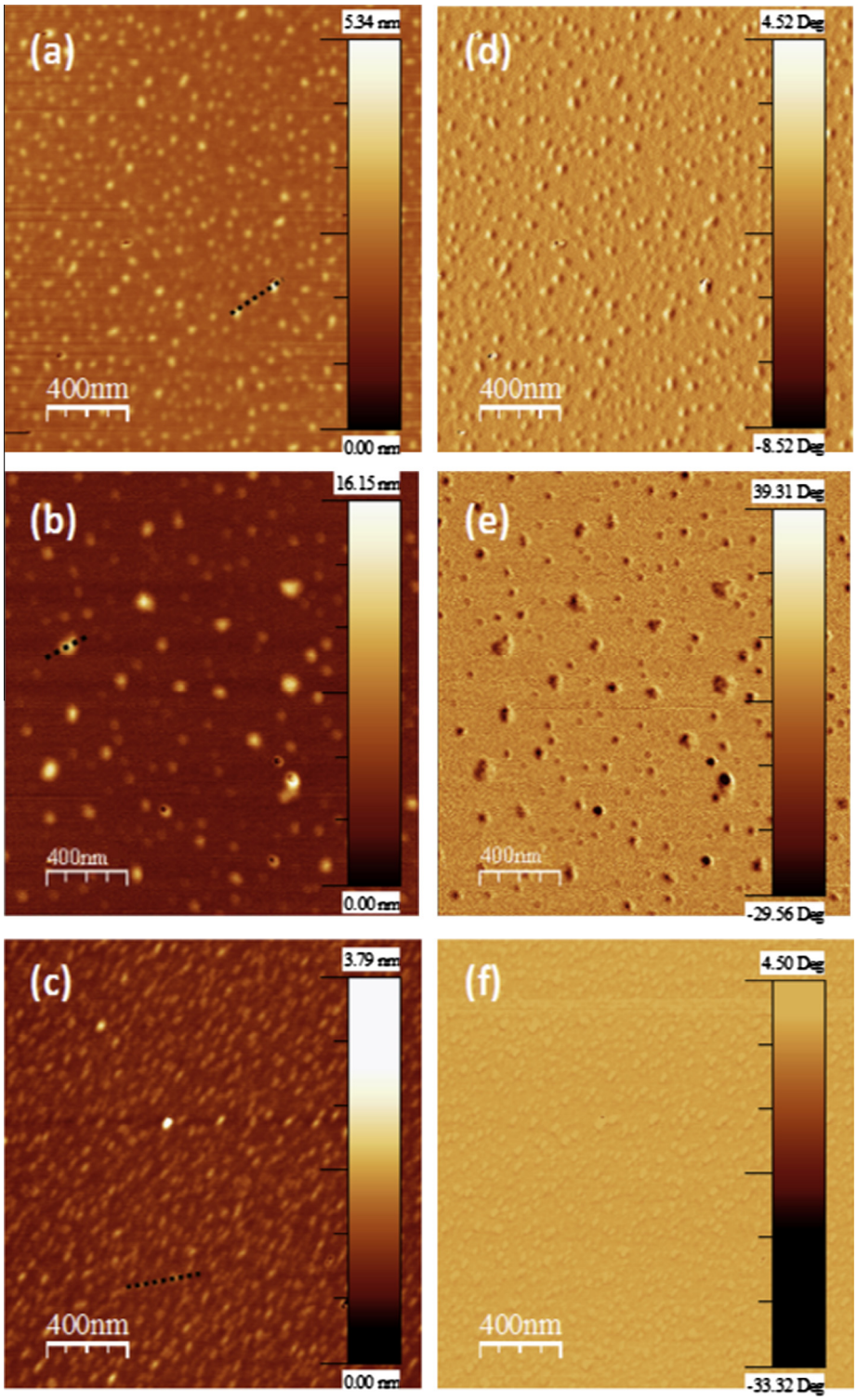

Fig. 7. AFM scans (2 μm × 2 μm, a–c height, d–f phase) of HPPhMeOx/SDS aggregates on mica surface deposited from dilute aqueous solutions (HPPhMeOx concentration, $c = 0.02$ mg ml^{-1}). (a and d) $Z = 0.22$, (b and e) $Z = 0.44$, (c and f) $Z = 0.66$. Dotted lines in a–c indicate horizontal tip motions for section analysis shown in Fig. 8.

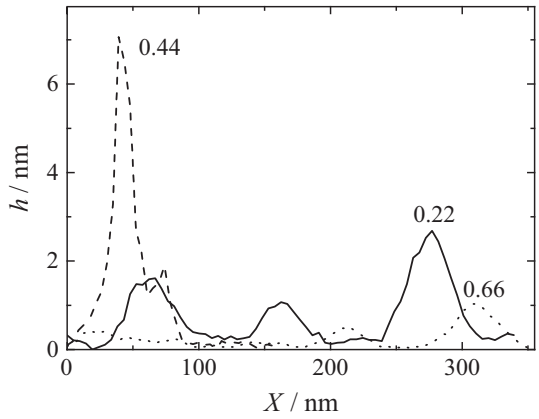

Fig. 8. Section analysis of AFM height scans of HPPhMeOx/SDS aggregates at different Z ratios (indicated above the curves). Lines indicating the corresponding horizontal tip motions are shown in Fig. 7(a)–(c).

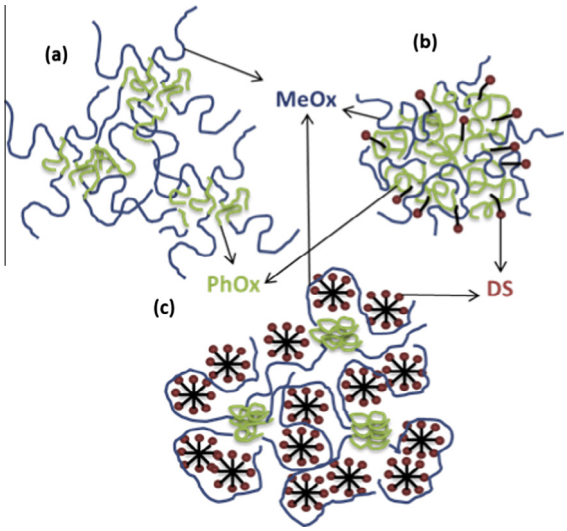

Fig. 9. Illustration of the internal structure of HPPhMeOx and HPPhMeOx/SDS aggregates: (a) HPPhMeOx aggregate with hydrophobic domains formed by HPPhMeOx chain ends rich with poly(2-phenyloxazoline) (PhOx) hydrophobic units and interconnected by parts of the HPPhMeOx chain rich with poly(2-methyloxazoline) (MeOx) hydrophilic units. (b) HPPhMeOx/SDS aggregate at $Z = \sim 0.2$ with large hydrophobic domains with embedded dodecylsulfate (DS) ions. (c) HPPhMeOx/SDS aggregate at $Z = \sim 0.6$ with small hydrophobic domains and PE-S complex formed by DS micelles and MeOx-rich parts of HPPhMeOx.

The disruption of the aggregates can also be observed in the low q range of the curve by the decrease of the power-law exponent indicating a transition to a less compact structure.

3.3. Imaging of HPPhMeOx/SDS aggregates by AFM

Fig. 7 shows AFM scans of HPPhMeOx/SDS aggregates deposited from dilute solutions to freshly peeled-out mica surface. Section analysis of the height scans shown in Fig. 8 indicates that the deposited aggregates are very flat, with the height of only a few nm. Both maximum size (about 100 nm) and maximum height of 7 nm of the HPPhMeOx/SDS aggregates is reached for the complex with $Z = \sim 0.4$. Although the average size of the deposited particles is smaller than that obtained from DLS, both AFM adn DLS reveal that the largest aggregates are formed in the case of the complex with $Z = \sim 0.4$ which has almost zero surface charge.

At $Z = 0.6$, the aggregates are slightly elongated. It is noteworthy that in the case of DHBP complexes with oppositely charged surfactant, the formation of cylindrical particles was reported for highly concentrated systems due to the formation of the hexagonal phase of the surfactant [35]. In the case of the AFM measurements, the concentration of HPPhMeOx/SDS solution from which the samples for AFM measurement are prepared by dip coating are very low, however, such phase transition can still occur prior to the deposition of the particles on the surface as a result of the removal of the solvent.

4. Conclusions

We have shown that amphiphilic cationic gradient polyelectrolyte poly[(2-methyl-2-oxazoline)-*grad*-(2-phenyl-2-oxazoline)-*mod*-(ethylene imine)] (HPPhMeOx) forms large aggregates (hydrodynamic radius of ca. 500 nm) in aqueous solutions, the structure of which resembles a physical network composed of mutually connected hydrophobic domains with the radius of ca. 10 nm (Fig. 9a). The self-assembly, despite the large size of the aggregates, allows for the structural rearrangement as evidenced by its interaction with sodium dodecyl sulfate. At low molar ratios of SDS to ethylene imine units, the embedding of individual surfactant ions into the network promotes the hydrophobic character of the domains and leads to the growth of their size (Fig. 9b). After the amount of the added SDS reaches the critical aggregation concentration, SDS micelles form polyelectrolyte–surfactant complex with HPPhMeOx chains which leads to the disruption of the domains (Fig. 9c). The ability of HPPhMeOx chains to form both hydrophobic domains and the PE-S complex indicates the amphiphilic character of the gradient polyelectrolyte chain.

Acknowledgements

The authors acknowledge the support from the Czech Science Foundation – Czech Republic (grant no. 14-11516S) and from the Ministry of Education, Youth and Sports of the Czech Republic (grant no. LK21302). This work is based upon experiments performed at the KWS-2 instrument (grant proposal no. 10296) operated by FRM II at the Heinz Maier-Leibnitz Zentrum (MLZ), Garching, Germany.

References

[1] J. Rodriguez-Hernandez, F. Checot, Y. Gnanou, S. Lecommandoux, Toward 'smart' nano-objects by self-assembly of block copolymers in solution, Prog Polym Sci 30 (2005) 691–724.
[2] N. Hadjichristidis, H. Iatrou, M. Pitsikalis, S. Pispas, A. Avgeropoulos, Linear and non-linear triblock terpolymers. Synthesis, self-assembly in selective solvents and in bulk, Prog Polym Sci 30 (2005) 725–782.
[3] A. Blanazs, S.P. Armes, R.J. Ryan, Self-assembled block copolymer aggregates: From micelles to vesicles and their biological applications, Macromol Rapid Commun 30 (2009) 267–277.
[4] A. Harada, K. Kataoka, Supramolecular assemblies of block copolymers in aqueous media as nanocontainers relevant to biological applications, Prog Polym Sci 31 (2006) 948–982.
[5] A. Rösler, G.W.M. Vandermeulen, H.A. Klok, Advanced drug delivery devices via self-assembly of amphiphilic block copolymers, Adv. Drug Deliv. Revs. 64 (2012) 270–279.
[6] R.W. Sandoval, D.E. Williams, J.K. Kim, C.B. Roth, J.M. Torkelson, Critical micelle concentrations of block and gradient copolymers in homopolymer: effects of sequence distribution, composition, and molecular weight, J. Polym. Sci. A Polym. Chem. 46 (2008) 2672–2682.
[7] J. Kuldová, P. Košovan, Z. Limpouchová, K. Procházka, O.V. Borisov, Self-association of copolymers with various composition profiles, Collect Czech Chem Commun 75 (2010) 493–505.
[8] Y. Zhao, Y.W. Luo, B.G. Li, S.P. Zhu, PH responsivity and micelle formation of gradient copolymers of methacrylic acid and methyl methacrylate in aqueous solution, Langmuir 27 (2011) 11306–11315.
[9] T. Ribaut, J. Oberdisse, B. Annighofer, B. Fournel, S. Sarrade, H. Haller, P. Lacroix-Desmazes, Solubility and self-assembly of amphiphilic gradient and block copolymers in supercritical CO_2, J. Phys. Chem. B 115 (2011) 836–843.
[10] C. Zheng, H. Huang, T.B. He, Micellization of St/MMA gradient copolymers: a general picture of structural transitions in gradient copolymer micelles, J. Phys. Chem. B 34 (2013) 1654–1661.
[11] O. Borisova, L. Billon, M. Zaremski, B. Grassl, Z. Bakaeva, A. Lapp, P. Štěpánek, O. Borisov, PH-triggered reversible sol–gel transition in aqueous solutions of amphiphilic gradient copolymers, Soft Matter 7 (2011) 10824–10833.
[12] O. Borisova, L. Billon, M. Zaremski, B. Grassl, Z. Bakaeva, A. Lapp, P. Štěpánek, O. Borisov, Synthesis and pH- and salinity-controlled self-assembly of novel amphiphilic block-gradient copolymers of styrene and acrylic acid, Soft Matter 8 (2012) 7649–7659.
[13] E. Vlassi, S. Pispas, Solution behavior of hydrolyzed gradient methyl/phenyl oxazoline copolymers and complexation with DNA, Macromol Chem Phys 216 (2015) 873–883.
[14] H.P.C. van Kuringen, V.R. de la Rosa, M.W.M. Fijten, J.P.A. Heuts, R. Hoogenboom, Enhanced selectivity for the hydrolysis of block copoly(2-oxazoline)s in ethanol–water resulting in linear poly(ethylene imine) copolymers, Macromol Rapid Commun 33 (2012) 827–832.
[15] Y. Milonaki, E. Kaditi, S. Pispas, C. Demetzos, Amphiphilic gradient copolymers of 2-methyl- and 2-phenyl-2-oxazoline: self-organization in aqueous media and drug encapsulation, J. Polym. Sci. A Polym. Chem. 50 (2011) 1226–1237.
[16] O. Sedláček, B.D. Monnery, S.K. Filippov, R. Hoogenboom, M. Hrubý, Poly(2-oxazoline)s – are they more advantageous for biomedical applications than other polymers?, Macromol Rapid Commun 33 (2012) 1648–1662
[17] H. Schlaad, Ch. Diehl, A. Gress, M. Meyer, A.L. Demirel, Y. Nur, A. Bertin, Poly(2-oxazoline)s as smart bioinspired polymers, Macromol Rapid Commun 31 (2010) 511–525.
[18] R. Hoogenboom, H.M.L. Lambermont-Thijs, M.J.H.C. Jochems, S. Hoeppener, C. Guerlain, C.A. Fustin, J.F. Gohy, U.S. Schubert, A schizophrenic gradient copolymer: switching and reversing poly(2-oxazoline) micelles based on UCST and subtle solvent changes, Soft Matter 5 (2009) 3590–3592.
[19] M. Glassner, K. Lava, V.R. de la Rosa, R. Hoogenboom, Tuning the LCST of poly(2-cyclopropyl-2-oxazoline) via gradient copolymerization with 2-ethyl-2-oxazoline, J. Polym. Sci. A Polym. Chem. 52 (2014) 3118–3122.
[20] I.K. Voets, A. de Keizer, M.A.C. Stuart, Complex coacervate core micelles, Adv Colloid Interface Sci 147–148 (2009) 300–318.
[21] D. Langevin, Complexation of oppositely charged polyelectrolytes and surfactants in aqueous solutions. A review, Adv. Colloid Interf. Sci. 147–148 (2009) 170–177.
[22] S. Zhou, B. Chu, Assembled materials: polyelectrolyte–surfactant complexes, Adv Mater 12 (2000) 545–556.
[23] P. Hansson, Self-assembly of ionic surfactants in polyelectrolyte solutions: a model for mixtures of opposite charge, Langmuir 17 (2001) 4167–4180.
[24] K. Kogej, Study of the effect of polyion charge density on structural properties of complexes between poly(acrylic acid) and alkylpyridinium surfactants, J. Phys. Chem. B 107 (2003) 8003–8010.
[25] A.V. Kabanov, T.K. Bronich, V.A. Kabanov, K. Yu, A. Eisenberg, Spontaneous formation of vesicles from complexes of block ionomers and surfactants, J Am Chem Soc 120 (1998) 9941–9942.
[26] J.F. Berret, B. Vigolo, R. Eng, P. Herve, I. Grillo, L. Yang, Electrostatic self-assembly of oppositely charged copolymers and surfactants: a light, neutron, and X-ray scattering study, Macromolecules 37 (2004) 4922–4930.

[27] M. Uchman, M. Gradzielski, B. Angelov, Z. Tošner, J. Oh, T. Chang, M. Štěpánek, K. Procházka, Thermodynamic and kinetic aspects of coassembly of PEO-PMAA block copolymer and DPCl surfactants into ordered nanoparticles in aqueous solutions studied by ITC, NMR, and time-resolved SAXS techniques, Macromolecules 46 (2013) 2172–2181.
[28] A. Radulescu, V. Pipich, H. Frielinghaus, M.-S. Appavou, KWS-2, the high intensity/wide Q-range small-angle neutron diffractometer for soft-matter and biology at FRM II, J Phys: Conf Ser 351 (2012) 012026.
[29] http://www.psi.ch/sinq/sansii/bersans.
[30] https://kur.web.psi.ch/sans1/SANSSoft/sasfit.html.
[31] I. Horcas, R. Fernandez, J.M. Gomez-Rodriguez, J. Colchero, J. Gomez-Herrero, A.M. Baro, WSXM: a software for scanning probe microscopy and a tool for nanotechnology, Rev Sci Instrum 78 (2007) 013705.
[32] C.M. Sørensen, J. Cai, N. Lu, Test of static structure factors for describing light-scattering from fractal soot aggregates, Langmuir 8 (1992) 2064–2069.
[33] N. Schonbeck, K. Kvale, T. Demarcy, J. Giermanska, J.-P. Chapel, J.-F. Berret, Swelling and disassembly of electrostatic aggregates upon addition of surfactant, Langmuir 30 (2014) 5620–5627.
[34] N. Lei, C.R. Safinya, D. Roux, K.S. Liang, Synchrotron X-ray-scattering studies on the sodium dodecyl sulfate–water–pentanol–dodecane L-3 sponge phase, Phys Rev E 56 (1997) 608–613.
[35] J.-F. Berret, Sphere-to-cylinder transition in hierarchical electrostatic complexes, Colloid Polym Sci 287 (2009) 801–810.